Simultaneous velocity-temperature measurements for the quantification of the effect of background turbulence on the mixing within a turbulent jet

Fanny Legay

Master of Engineering

Department of Mechanical Engineering

McGill University

Montreal, Quebec, Canada

August 2020

A thesis submitted to McGill University in partial fulfillment of the requirements of the degree of Master of Engineering

ACKNOWLEDGEMENTS

First and foremost, I would like to express my sincere gratitude to my supervisor, Prof. Laurent Mydlarski, for his continuous support and guidance during my studies at McGill University. He always found time to answer my questions, share his knowledge, or review and encourage me in my work, and I am deeply grateful for that.

I would like to thank the turbulence team, and especially Alaïs Hewes, for teaching me how to make and use hot- and cold-wires, for her help with the technical issues in the lab, and for her patience in answering my numerous questions.

I wish to say a very special thanks to my family and friends for their unconditional love and confidence. They provided precious support in my studies and my whole life.

Finally, my appreciation goes to the Natural Sciences and Engineering Research Council of Canada (NSERC) for supporting and funding this research.

ABSTRACT

Turbulent jets are commonly encountered flows, which frequently transport a scalar and occur in both natural and man-made settings (e.g. pollutants being dispersed from a smokestack into the atmosphere; injection of reactants into a combustor). In the majority of such contexts, the jet issues into an environment that is turbulent – a factor that plays a key role in the jet's subsequent evolution, yet one that has been the subject of little study. The objective of this work was therefore to quantify the (longitudinal and radial) velocity and scalar fields of an axisymmetric turbulent jet of heated air emitted into a turbulent background.

To this end, turbulent coflows with three different levels of turbulence intensity ($T_i = 0.4\%$, 2.2% and 9.8%) were generated in a wind tunnel by means of passive and active grids and a flow-conditioning circuit was designed and built to generate the axisymmetric jet of heated air. Emphasis was placed on simultaneous measurements of the velocity and temperature fields, with the aim of both quantifying and further understanding the mixing of jets within a turbulent environment. Hot-wire anemometry and cold-wire thermometry were employed, using a combined hot- and cold-wire probe that was designed and built for this purpose. Simultaneous measurements of the jet's velocity and temperature fields were made at various downstream positions ($26.5 \leq x/D \leq 75.0$) and for four jet-to-coflow velocity ratios ($\lambda = 3.4, 4.3, 4.6$ and 5.7).

Measurements of the velocity and temperature fields, and the combined velocity-scalar statistics, showed that the background turbulence accelerated the evolution of the jet, by increasing both the rate at which the velocity and scalar fields decay in

magnitude and broaden in width with increasing downstream distance. Moreover, the effective "destruction" of the average jet was observed under certain conditions. Spectral analyses suggested that the entrainment mechanism occurs at intermediate scales for low levels of background turbulence, but that large scales of the background turbulence play a significant role when the intensity of the background turbulence increases (for the cases studied herein). Probability density functions demonstrated that (i) a larger range of instantaneous velocities throughout the jet, and (ii) the presence of cold air deeper into the jet were observed due to the background turbulence. Conditional expectations suggested that axial velocity fluctuations transport larger radial velocity (momentum) and temperature fluctuations, and that the radial transport of temperature fluctuations was enhanced when the intensity of the background turbulence increased.

RÉSUMÉ

Les jets turbulents sont des écoulements fréquemment rencontrés, qui transportent généralement un scalaire, et qui se produisent à la fois dans des situations naturelles et créées par l'homme (ex. polluants dispersés dans l'atmosphère par une cheminée; réactifs injectés dans une chambre de combustion). Dans la majorité des cas, le jet est émis dans un environnement qui est turbulent, un facteur qui joue un rôle clé dans l'évolution subséquente du jet, et qui a pourtant été le sujet de peu d'études. L'objectif de ce travail était ainsi de quantifier le champ de vitesse (longitudinale et radiale) et le champ scalaire d'un jet turbulent axisymétrique d'air chaud, émis dans un milieu turbulent.

Dans ce but, des écoulements turbulents, parallèles à la direction du jet, avec trois niveaux d'intensité de turbulence ($T_i = 0.4\%$, 2.2% and 9.8%), ont été générés au moyen de grilles passives et actives, et un circuit de conditionnement de l'écoulement a été conçu et construit pour créer le jet axisymétrique d'air chaud. L'accent a été mis sur les mesures simultanées des champs de vitesse et de scalaire, avec pour but à la fois la quantification et une meilleure compréhension du mélange des jets dans un environnement turbulent. Les techniques d'anémométrie à fil chaud et de thermométrie à fil froid ont été employées, en utilisant une sonde combinée de fils chauds et froids qui a été conçue et construite pour cet objectif. Des mesures simultanées des champs de vitesse et de température du jet ont été faites à plusieurs distances en aval du jet ($26.5 \leq x/D \leq 75.0$) et pour quatre rapports de la vitesse du jet sur celle de l'écoulement d'arrière-plan ($\lambda = 3.4, 4.3, 4.6$ and 5.7).

Les mesures des champs de vitesse et de température, et les statistiques combinées de la vitesse et du scalaire, ont montré que la turbulence de l'arrière-plan accélère l'évolution du jet, en augmentant à la fois la vitesse à laquelle les champs de vitesse et de température décroisent en amplitude, et celle à laquelle ils s'étalent en largeur avec la distance en aval du jet. De plus, la "destruction" effective en moyenne du jet a été observée sous certaines conditions. Les analyses spectrales ont suggéré que le mécanisme d'entrainement se déroule aux échelles intermédiaires pour de faibles niveaux de turbulence en arrière-plan, mais que les grandes échelles jouent un rôle important lorsque l'intensité de la turbulence d'arrière-plan augmente (pour les cas étudiés ici). Les fonctions de densité de probabilité ont démontré que (i) un plus grand éventail de vitesses instantanées à travers le jet, et (ii) la présence d'air froid plus profondément dans le jet sont observés en raison de l'environnement turbulent. Les moyennes conditionnelles ont suggéré que les fluctuations de vitesse axiale transportent de plus grandes fluctuations de vitesse radiale et de température, et que le transport radial des fluctuations de température est amélioré lorsque l'intensité de la turbulence d'arrière-plan augmente.

TABLE OF CONTENTS

LIST OF TABLES

LIST OF FIGURES

CHAPTER 1
Introduction

1.1 Objectives and motivation

Turbulent jets are a common type of flow, found in both natural and engineering contexts. They frequently transport a scalar, like temperature or chemical species concentration, and their study has many applications. For instance, when pollutants are discharged into the atmosphere, they are usually released in the form of turbulent jets, dispersed from a smokestack. In combustion, jets are widely used to inject reactants (e.g. fuel) into the reaction chamber. Thus, to minimize the impact of potentially harmful chemicals on both the health and the environment, and improve the efficiency of combustion processes, knowledge of the velocity and scalar fields of the jet is important. Moreover, turbulent jets are very efficient at diluting the scalar they carry into their surroundings by entrainment and mixing. The understanding of these processes, through the study of both the velocity and scalar fields of turbulent jets, is therefore a key element.

It should be noted that the dynamics of a jet not only depend on the jet itself, but also on the environment in which it is issued. Similar jets can evolve differently if there are differences in their surroundings. Several parameters can affect the development of jets, such as mean flow advection, density stratification, boundary effects or the turbulence intensity of the surrounding fluid. To account for the impact of all these factors on the evolution of jets, it is advisable to study each one individually.

In the majority of jet flows, the fluid issues into an environment that is turbulent; however, the effect of the background turbulence on turbulent jets has been the subject of little study. The vast majority of previous studies of jets have focused on turbulent jets emitted into quiescent or laminar surroundings, so their results may not be applicable to many real situations. Of the research examining turbulent jets emitted into turbulent surroundings, it has been shown that the presence of background turbulence plays a key role in the jet's subsequent evolution. However, there is no general understanding of the exact effect of background turbulence on jets. Some works suggest an increase in the dilution of jets in the presence of background turbulence (Wright 1994), whereas other studies hypothesize a decrease in the entrainment (due to the breaking up the jet structure, Hunt 1994). Moreover, among these studies, the velocity and scalar fields have generally been studied separately, which prevents researchers from being able to directly calculate combined velocity-scalar statistics such as the turbulent scalar flux. To quantify and further understand the mixing processes within turbulent jets, simultaneous measurements of these two fields are therefore required.

The main objective of this work is to experimentally study the effect of background turbulence on the dynamics and mixing of an axisymmetric turbulent jet of heated air by way of simultaneous velocity and temperature measurements of a jet emitted into homogeneous, isotropic turbulence. To this end, hot-wire anemometry and cold-wire thermometry are employed to obtain statistics of the velocity and temperature fields. Using these techniques, a sensor was designed and built to be capable of making simultaneous measurements of two components of velocity (U and V) and the scalar (*viz.* temperature). An experimental set-up was designed and built

to obtain an axisymmetric turbulent jet of heated air, and its evolution was investigated while varying various parameters of interest. The homogeneous, isotropic background turbulence was generated in a wind tunnel by means of passive and active grids. The jet was emitted into this turbulent coflow and three different levels of background turbulence intensity were examined. For each of them, the velocity and temperature statistics were measured at four different downstream positions from the jet's exit. The velocities of the jet and coflow were also varied. Two jet velocities and two background velocities were selected, which allows for a comparison of the behaviour of the jet for different jet-to-coflow velocity ratios.

1.2 Thesis organization

The subsequent chapters of the thesis are organized as follows. Chapter 2 presents a literature review of turbulent jets in quiescent, laminar and turbulent backgrounds. The experimental apparatus and techniques are presented in Chapter 3. It includes a description of the wind tunnel, the jet set-up, and the combined hot- and cold-wire (X-T) probe. The data acquisition and analysis techniques are then described, as well as the calibration procedures for the hot-and cold-wires, and the passivity of the scalar is confirmed. The results of the experiments are discussed in Chapter 4. The measurement technique is first validated. Then, the mean and r.m.s. velocities and temperature, combined velocity-temperature statistics, spectra, probability density functions, and conditional expectations of the two components of velocity and the temperature are presented and discussed. Finally, Chapter 5 provides a summary and suggestions for future work.

CHAPTER 2
Literature Review

This chapter reviews publications in the literature that are related to the present work. The following topics are presented: §2.1 Turbulent jets in quiescent backgrounds; §2.2 Turbulent jets in laminar coflowing backgrounds; and §2.3 Turbulent jets in turbulent backgrounds.

2.1 Turbulent jets in quiescent backgrounds

Jets, like plumes, wakes and mixing layers, belong to the category of free shear flows and are inhomogeneous and anisotropic. In this study, the flow under consideration is an incompressible (Mach number $(Ma) < 0.3$) flow of an effectively constant property and Newtonian fluid (air). The jet studied herein is steady, axisymmetric, momentum-driven and turbulent.

Turbulence is a complex phenomenon that is not easy to define, so it is usually defined by is main characteristics. Turbulent flows are random, diffusive, dissipative and continuum phenomena that arise at high Reynolds numbers. A turbulent flow contains a wide range of scales and 3-D vorticity fluctuations (Tennekes and Lumley 1972). If a jet is heated, the scalar under study is the air temperature. If the jet's temperature is kept low enough so that buoyancy effects do not affect the velocity field, the scalar is deemed passive.

2.1.1 Governing equations

The flow of an axisymmetric jet can be described in a cylindrical coordinate system (x, r, θ) in which the statistics are only dependent on the axial and radial coordinates. If the jet has a high Reynolds number, we can neglect the effect of the fluid's viscosity and thermal diffusivity. Thus, the continuity, Navier-Stokes (momentum) and advection-diffusion equations for the jet can be written as follows:

$$\frac{\partial \tilde{U}}{\partial x} + \frac{1}{r}\frac{\partial}{\partial r}(r\tilde{V}) = 0 \tag{2.1}$$

$$\tilde{U}\frac{\partial \tilde{U}}{\partial x} + \tilde{V}\frac{\partial \tilde{U}}{\partial r} = -\frac{1}{\rho}\frac{\partial \tilde{P}}{\partial x} \tag{2.2}$$

$$\tilde{U}\frac{\partial \tilde{V}}{\partial x} + \tilde{V}\frac{\partial \tilde{V}}{\partial r} - \frac{\tilde{W}^2}{r} = -\frac{1}{\rho}\frac{\partial \tilde{P}}{\partial r} \tag{2.3}$$

$$\tilde{U}\frac{\partial \tilde{T}}{\partial x} + \tilde{V}\frac{\partial \tilde{T}}{\partial r} = 0 \tag{2.4}$$

with $\tilde{U}$, $\tilde{V}$ and $\tilde{W}$ respectively denoting the instantaneous axial, radial and azimuthal velocities, $\tilde{T}$ the temperature, $\tilde{P}$ the pressure, and ρ the fluid's density (the $\tilde{}$ symbol used herein denotes instantaneous parameters).

Given the random nature of turbulent flows, it is common practice to apply the Reynolds decomposition to the above equations, in which the instantaneous parameters are decomposed into the sum of their mean and fluctuating components:

$$\tilde{U} = \overline{U} + u \; ; \quad \tilde{V} = \overline{V} + v \; ; \quad \tilde{W} = \overline{W} + w \; ; \quad \tilde{T} = \overline{T} + \theta \; ; \quad \tilde{P} = \overline{P} + p \tag{2.5}$$

Overbars indicate average values and there is no swirl in the flow so $\overline{W} = 0$. Applying this decomposition to equations (2.1) - (2.4) and then averaging yields the Reynolds-averaged continuity, Navier-Stokes and advection-diffusion equations for the mean

flow:

$$\frac{\partial \overline{U}}{\partial x} + \frac{1}{r}\frac{\partial}{\partial r}(r\overline{V}) = 0 \tag{2.6}$$

$$\overline{U}\frac{\partial \overline{U}}{\partial x} + \overline{V}\frac{\partial \overline{U}}{\partial r} = -\frac{1}{\rho}\frac{\partial \overline{P}}{\partial x} - \frac{\partial \overline{u^2}}{\partial x} - \frac{1}{r}\frac{\partial}{\partial r}(r\overline{uv}) \tag{2.7}$$

$$\overline{U}\frac{\partial \overline{V}}{\partial x} + \overline{V}\frac{\partial \overline{V}}{\partial r} = -\frac{1}{\rho}\frac{\partial \overline{P}}{\partial r} - \frac{\partial}{\partial x}(\overline{uv}) - \frac{1}{r}\frac{\partial}{\partial r}(r\overline{v^2}) + \frac{\overline{w^2}}{r} \tag{2.8}$$

$$\overline{U}\frac{\partial \overline{T}}{\partial x} + \overline{V}\frac{\partial \overline{T}}{\partial r} = -\frac{\partial}{\partial x}(\overline{u\theta}) - \frac{1}{r}\frac{\partial}{\partial r}(r\overline{v\theta}) \tag{2.9}$$

In these Reynolds-averaged equations, there are now more unknowns than equations, so additional relationships are needed to solve them. This is called the closure problem (Tennekes and Lumley, 1972). The unknown variables are the Reynolds stresses, $\overline{u_i u_j}$, and the turbulent scalar fluxes, $\overline{u_i \theta}$. They respectively represent the transport of momentum and the transport of scalar fluctuations by the turbulent velocity fluctuations. They are particularly important to the understanding of the mixing processes that occur in turbulent jets.

The jet Reynolds number is defined as $Re_{jet} \equiv \dfrac{U_j D}{\nu}$ where U_j is the velocity at the jet exit, D is the jet diameter and ν is the kinematic viscosity of the air. For turbulent flows, the largest length scale (the integral length scale) is determined by the geometry of the flow and the velocity characterizing that scale is approximately the root mean square (r.m.s.) velocity $u_{rms} \equiv (\overline{u^2})^{1/2}$. Kolmogorov (1941) characterized the smallest scales in turbulent flows by defining the Kolmogorov (length, time and velocity) scales ($\eta \equiv (\nu^3/\epsilon)^{1/4}$, $\tau \equiv (\nu/\epsilon)^{1/2}$, $u \equiv (\nu\epsilon)^{1/4}$), using the kinematic viscosity and ϵ, the dissipation rate of turbulent kinetic energy per unit mass. At scales on the order of η, the turbulent kinetic energy is "dissipated" into internal energy by way of viscous interactions. Kolmogorov theory predicts a $-5/3$ power

law region in the inertial subrange (a range in between the largest and Kolmogorov scales, where both viscosity and large-scale effects can be considered negligible).

For the study of temperature as a scalar transported in a flow, the Prandtl number ($Pr \equiv \nu/\alpha$) is an important dimensionless parameter. It represents the ratio of the "momentum diffusivity" (i.e. the kinematic viscosity) to the thermal diffusivity. It do not depend on the flow, but only on the fluid under study. For air, the Prandtl number is approximately equal to 0.7 at standard temperature and pressure. The dissipation of temperature fluctuations in flows of air occurs at a scale called the Corrsin scale, defined as $\eta_\theta \equiv (\alpha^3/\epsilon)^{1/4}$ (Corrsin 1951). For air, $\eta_\theta = \eta Pr^{-3/4}$ is therefore only slightly larger than η. Similar to the velocity field, the characteristic temperature for the large-scale fluctuations is the root mean square (r.m.s.) temperature $\theta_{rms} = (\overline{\theta^2})^{1/2}$.

2.1.2 Self-similarity in turbulent jets

An extensive number of experimental, numerical and theoretical studies have focused on turbulent jets in quiescent backgrounds. Both the velocity field (Wygnanski and Fiedler 1969, Fisher et al. 1979, Panchapakesan and Lumley 1993, Hussein et al. 1994, Pope 2000, Lipari and Stansby 2011, Darisse et al. 2015) and the scalar field (Wilson and Danckwerts 1964, Becker et al. 1967, Birch et al. 1978, Lockwood and Moneib 1980, Dowling and Dimotakis 1990, Panchapakesan and Lumley 1993, Darisse et al. 2015) exhibit similar behaviours, to be discussed below.

A jet flow can be divided into two sub-regions in the streamwise direction. There is first the near field, or zone of flow establishment, which is the initial developing region (Weisgraber et al. 1998). Then, there is the far field, or zone of established flow, which is characterized by self-similar velocity and scalar fields. Self-similarity

is an important characteristic of turbulent jets and implies that, when properly non-dimensionalized, their (velocity and temperature) profiles become independent of downstream position and collapse onto a single curve. In the self-similar region, the mean radial profiles of both the axial velocity and scalar concentration are approximately Gaussian (Fisher et al. 1979, Lockwood and Moneib 1980) and their centerline values decay as x^{-1}, with x being the downstream distance from the jet exit. The velocity and scalar half-widths, defined as the radial distances at which the mean axial velocity and mean scalar concentration equal half of their centerline values, scale proportionally to the downstream distance (i.e. $\propto x^1$, Wilson and Danckwerts 1964).

For the velocity field, self-similarity of the higher-order moments occurs farther downstream than the mean flow. Wygnanski and Fiedler (1969) observed that the mean velocity was self-similar at roughly 20 diameters downstream of the jet nozzle, whereas the longitudinal velocity fluctuations became self-similar at 40 diameters downstream. Moreover, the radial and tangential turbulence intensities reached self-similarity only 70 diameters from the nozzle. Hussein, Capp and George (1994) performed hot-wire and laser-Doppler anemometry (LDA) measurements in a jet similar to that of Wygnanski and Fiedler (1969). However, they used a much larger facility and demonstrated that the jet's behaviour could be strongly influenced by backflow or recirculation within the experimental enclosure. Similarly for the scalar field, Wilson and Danckwerts (1964) and Lockwood and Moneib (1980) measured the temperature fluctuations in a turbulent jet of hot air. They found that self-similarity was achieved beyond $x/D > 10$ for the mean temperature excess and beyond $x/D > 40$ for the temperature fluctuations (similar to the Reynolds stresses).

It has also been noted that the different initial conditions of a jet's flow can lead to differences in their evolution towards self-similarity (George 1989). In general, there exists two typical initial conditions for a turbulent jet, which are generated by either a smooth contracting nozzle or a long pipe. For these two cases, the respective velocity profiles at the jet exit are a top-hat velocity profile or a fully-developed velocity profile. The downstream position at which the mean velocity profile becomes self-similar is the same for both cases, but it has been shown to be smaller for the Reynolds stresses when the jet exit is a top-hat profile (Ferdman et al. 2000, Xu and Antonia 2002). The scalar field has been shown to be more sensitive to initial flow conditions (Mi et al. 2001), but their effect on the evolution of the velocity and scalar fields diminishes with the downstream distance in all cases, until the differences become negligible.

2.1.3 Entrainment in turbulent jets

When a turbulent jet develops downstream, it spreads in the radial direction and its width increases. This is due to the addition of ambient fluid, that is drawn radially into the jet through its surface and becomes turbulent. This process is called entrainment and was first studied and analyzed by Morton et al. (1956). They proposed that the inflow velocity, referred to as the entrainment velocity (normal to the surface of the jet) is proportional to the local axial mean velocity at each location of the jet. The constant of proportionality, α, is known as the entrainment coefficient. Entrainment is the principal mechanism responsible for enhancing the mixing of two adjacent streams. With it, turbulent jets are able to mix large volumes of ambient fluid with the discharged fluid, therefore being an effective mechanism

for the dilution of pollutants into the environment and reducing their detrimental effects.

Two different entrainment mechanisms have been studied in turbulent jets issued in quiescent backgrounds. The first one is a large-scale process called engulfment and the second one is a small-scale process called nibbling. There are multiple views in the literature on which one is dominant.

On one hand, Townsend (1966) proposed the 'equilibrium hypothesis' in which the large eddies of the turbulent flow are the principal agent of entrainment. This hypothesis has been supported by many investigations (Yule 1978, Long and Chu 1981). Shlien (1987) used photographs to visualize a fluorescent dye injected into an axisymmetric turbulent jet. They observed that the tagged entrained fluid is drawn deeply into the turbulent jet, supporting the hypothesis that the main entrainment mechanism is engulfment by the large-scale structures. With instantaneous concentration measurements, Dahm and Dimotakis (1987) showed that the entrainment and mixing processes in a turbulent jet have a spatial and temporal large-scale organization with unmixed ambient fluid being transported deep into the jet.

On the other hand, the 'superlayer' hypothesis states that entrainment is mainly caused by small-scale eddy motions (nibbling) acting at the thin turbulent/non-turbulent interface between the jet and its quiescent surroundings. At this interface, of thickness on the order of the Kolmogorov microscale, small eddies interact with the jet's structure. In this process, originally proposed by Corrsin and Kistler (1955), the vorticity of the turbulent flow is transmitted to the irrotational fluid by viscous forces. Direct numerical simulations of a turbulent axisymmetric jet by Mathew and Basu (2002) have shown that the entrainment process is dominated by small scales, even though the overall entrainment rate can be predicted by large-scale quantities.

The experimental studies of Westerweel et al. (2005, 2009) are also consistent with the hypothesis that nibbling is the dominant entrainment process. They measured the fluxes of turbulent kinetic energy and enstrophy in a jet and showed that the proportion of fluid engulfed by large scales is less than 10% of the total entrained fluid.

Philip and Marusic (2012) suggested that entrainment in jets is a three-part-process involving both small and large scales. Small eddies are responsible for nibbling, while large eddies cause both engulfment and a third process called "induced inward motion". They argued that, instantaneously, both induced and engulfed fluids pass through the turbulent/non-turbulent interface where they are nibbled into turbulent fluid. Small-scale nibbling eddies can also have an effect akin to diffusion and transform irrotational fluid into turbulent fluid by themselves.

Among the parameters used to measure the amount of entrainment and mixing in an axisymmetric jet, there is the mass flow rate, $\dot{m}$, defined in equation 2.10 for an axisymmetric jet in quiescent backgrounds. Its evolution is directly related to the entrainment coefficient α (Morton et. al. 1956).

$$\dot{m} = 2\pi\rho \int_0^{+\infty} \overline{U} r dr \tag{2.10}$$

For the transport of axial momentum, Hussein et al. (1994) derived the second-order momentum integral for an axisymmetric jet to be:

$$\int_0^{+\infty} (\overline{U}^2 + \overline{u^2} - \overline{v^2}) r dr - \frac{M}{2\pi\rho} = -\frac{1}{2}\frac{d}{dx}\left[\int_0^{+\infty} (\overline{UV} + \overline{uv}) r^2 dr\right]_0^x + \frac{1}{2}\int_0^{+\infty} \overline{V}^2 r dr \tag{2.11}$$

In quiescent backgrounds, the right-hand side is negligible and one concludes that the total momentum flow rate (M) is equal to the sum of its mean (M_m) and turbulent

(M_t) components, which respectively correspond to the transport of the momentum by the mean flow and by the velocity fluctuations (see equation 2.12). When temperature is the transported scalar, a similar equation (2.13) can be obtained for the total scalar flow rate of an axisymmetric jet in quiescent backgrounds. $\dot{m}$, M and F respectively quantify the amount of mass, momentum and scalar transported across the jet cross-section per unit time.

$$M = M_m + M_t \quad ; \quad M_m = 2\pi\rho \int_0^{+\infty} \overline{U}^2 r dr \quad ; \quad M_t = 2\pi\rho \int_0^{+\infty} (\overline{u^2} - \overline{v^2}) r dr \tag{2.12}$$

$$F = F_m + F_t \quad ; \quad F_m = 2\pi\rho \int_0^{+\infty} (\overline{U} \cdot \overline{T}) r dr \quad ; \quad F_t = 2\pi\rho \int_0^{+\infty} \overline{u\theta} r dr \tag{2.13}$$

If a steady-state, constant-property, turbulent jet in a quiescent background is self-similar, its centerline mean velocity ($\overline{U}_c$) decays as x^{-1} and its half-width ($r_{1/2}$) scales as x^1. The total mass flow rate therefore increases linearly with the downstream position ($m/m_0 = c \times x/D$, where m_0 is the mass flow rate at the jet nozzle and c is a constant of proportionality). In the fully developed region of a jet of air emitted into a quiescent background of air, Ricou and Spalding (1961) found $c = 0.32$. Contrary to the total mass flow rate, the total momentum flow rate and the total scalar flow rate remain constant for a jet in quiescent backgrounds. Law and Wang (2000) used combined digital particle image velocimetry (DPIV) and planar laser induced fluorescence to measure the mean and turbulent mass transport in a turbulent jet issuing into a stagnant fluid. They found that the mean momentum (M_m) and scalar (F_m) flow rates respectively accounted for 90% and 93% of the total momentum (M_0) and scalar (F_0) flow rates at the jet exit.

2.2 Turbulent jets in laminar coflowing backgrounds

When a turbulent jet issues into a parallel moving stream of air, the mean velocity excess at the jet centerline ($\overline{U}_c - U_\infty$) is initially much higher than the free-stream velocity U_∞. This is the strong jet region and the jet's structure is close to that of a jet in a quiescent background. The excess velocity then gradually decreases until it becomes much smaller than the coflow velocity. This is the weak jet or strongly advected region, in which the jet's structure can be compared to the one of a wake (Bradbury and Riley 1967). The entrainment mechanism in the jet also evolves accordingly.

For jets in coflows, the notion of self-similarity of the mean properties has been confirmed by multiple studies (Antonia and Bilger 1973; Smith and Hughes 1977; Nickels and Perry 1996). They all found that the radial profiles of the mean velocity collapse far enough downstream from the jet's exit when suitably normalized. The mean velocity was therefore independent of the jet's initial conditions and only depended on the net momentum excess and local conditions. Similar observations were made for the mean scalar concentration. Chu et al. (1999) and Davidson and Wang (2002) showed that the scalar field became self-similar for jets emitted into laminar coflows.

For the higher-order moments, however, Antonia and Bilger (1973), Smith and Hughes (1977) and Nickels and Perry (1996) observed that they were not self-similar. They measured higher values of the normalized axial r.m.s. velocity and Reynolds shear stresses for a jet in a coflow compared to a jet in quiescent backgrounds and these values kept increasing with the downstream distance. It therefore suggests that the assumption of self-similarity for jets in a coflow may not hold.

To describe the mixing in jets, integral models have been developed. They are based on the integration of the governing equations, combined with the specification of an entrainment function. A characteristic velocity of the flow is chosen, which leads to the expression of an entrainment coefficient α (Morton et. al. 1956). When the turbulent jet is emitted into a coflow, the characteristic velocity and entrainment coefficient must be modified.

Chu et al. (1999) observed that the concentration and velocity half-widths vary non-linearly with downstream distance. Similar to Nickels and Perry (1996), they also found that the decay of the centerline velocity deviates from the classic x^{-1} (in the strong jet region) to $x^{-2/3}$ law (in the weak jet region). They developed an integral model to describe the evolution of jets in such coflows.

The work of Davidson and Wang (2002) focused on the strongly advected (weak jet) region. They found that the mixing processes evolve and the spread constant changes from the weakly to the strongly advected regions. They argued that the spread relationship traditionally employed to model the mean behavior of the jet should be redefined and they therefore proposed a new entrainment function.

2.3 Turbulent jets in turbulent backgrounds

2.3.1 Effect of ambient turbulence on the velocity and scalar fields

In the vast majority of previous works, turbulent jets (and plumes) were emitted into quiescent or laminar surroundings. In most of the models used to describe the behaviour of turbulent jets, the effect of coflow turbulence is not taken into account (e.g. Chu et. al. 1999). The results and conclusions from these different studies may therefore not be valid for jets emitted into turbulent backgrounds. Davidson and Wang (2002) compared measurements of a jet's spreading rate in a coflow and

noticed scatter in the results. They suggested that this was associated with the presence of ambient turbulence in those experiments, albeit at low intensity. To improve the understanding of this topic, there have been recent studies investigating turbulent jets issuing into turbulent fields.

For a plane jet emitted into a turbulent shallow open-channel flow, Gaskin et al. (2004) argued that the downstream evolution of the scalar concentration occurs in three regions. Near the nozzle exit (the near field), the background turbulence has a negligible effect on the jet and its evolution is similar to a jet emitted into a quiescent background. In the second region, the background turbulence begins to disrupt the structure of the jet. In the third region (the far field), the jet's structure is destroyed by the turbulent background and scalar mixing is only due to the fluctuations of the background turbulence.

The overall effect of the turbulent background is to reduce the mean values and increase the r.m.s. values of both the velocity and concentration fields, compared to a jet in quiescent surroundings. The comparison of the velocity field (Khorsandi 2011) and the scalar field (Perez-Alvarado 2016, Afrooz 2019) shows that they have similar behaviors. For a jet in quiescent backgrounds, both the centerline mean velocity and concentration decay as x^{-1}. However, in turbulent backgrounds, they were found to decay at a faster rate and this rate increases with the level of background turbulence. The main difference between the velocity and scalar fields is the radial extent of their mean and r.m.s. profiles. The half-widths of the scalar fields are larger than those of the velocity fields. This difference is more significant for jets in turbulent backgrounds than for jets in quiescent backgrounds. It has been attributed to the increased radial transport of scalar by both the meandering of the jet and the turbulent diffusion, which are enhanced by the turbulent background.

As respectively noted by Khorsandi et al. (2013) and Perez-Alvarado (2016), the mean momentum and scalar flow rates (M_m and F_m) for a jet in a turbulent background with zero mean velocity are not constant, but decrease along the axial direction, in contrast to a jet in quiescent surroundings. This becomes progressively more important as the background turbulence begins to affect the jet structure, and must be accounted for in an integral model. As previously mentioned, the ratio of the turbulent to mean momentum flow rates in quiescent surroundings is typically only about 10%, so a reasonably accurate first-order integral model could be developed by considering only the mean momentum flow rate. However, when background turbulence is present, the relative contribution of the turbulent momentum flow rate becomes more important.

Lai et al. (2019) carried out experimental and theoretical investigations of a buoyant jet discharging into a homogeneous, isotropic turbulent background without mean flow. They developed a general integral jet model that included the effect of the background turbulence. They showed that the total momentum remained conserved when the second-order statistics are taken into account in the model.

For a jet in a turbulent background with zero mean flow, Khorsandi et al. (2013) reported data for $\overline{U}$ and $\overline{V}$ which were not measured at the same locations into the jet, and no data for the radial velocity fluctuations were presented. This therefore does not allow for the calculation of all term in equation 2.11, such as $\overline{UV}$, $\overline{uv}$ and $\overline{v^2}$. Moreover, the calculation of the velocity-scalar statistics for a turbulent jet in turbulent backgrounds is needed to fully understand and quantify the mixing processes. Simultaneous measurements of velocity and concentration are therefore necessary to calculate the terms $\overline{u\theta}$ and $\overline{UT}$ of the scalar conservation equation 2.13.

Moreover, for a jet emitted into a turbulent background, none of the mean and fluctuating components of both the velocity and scalar fields becomes self-similar. This results from the multiplicity of scales in the flow, as characteristic scales for both the turbulent jet *and* the turbulent background are independent. This lack of self-similarity indicates an evolution in the jet's structure which presumably implies a modification of the entrainment mechanism.

2.3.2 Effect of ambient turbulence on the mixing and entrainment

As allude to above, there are two main theories on the effect of background turbulence on the jet mixing and entrainment. The first theory (proposed by Wright 1994) suggests that there is a superposition of the dilution effects of both the jet and the turbulent surroundings. Wright (1994) added a new term in the entrainment function used in integral models to account for ambient turbulence and suggested that an increase in the background turbulence intensity leads to an increase in the jet entrainment rate. On the other hand, Hunt (1994) suggested that, when the entrainment velocity of the jet is larger than the r.m.s. velocity of the background turbulence, the external turbulence is entrained and does not increase the rate of spreading of the jet. However, when the turbulence intensity of the background becomes on the same order as the one of the jet, the jet's structure will be disrupted by its turbulent surroundings. In contrast with the first theory, Hunt (1994) argued that the external turbulence can serve to reduce the entrainment and that the jet's dilution is only due to turbulent diffusion. Both theories have been discussed by different experimental studies.

Ching et al. (1995) investigated the evolution of a linear turbulent plume in a turbulent flow that increased in intensity as the plume evolved downstream, and

concluded that the background turbulence increased the dilution. They showed that the plume growth rate was only slightly affected during the initial rise, but then increased significantly when the background turbulent intensity was about 1.6 times higher than the convective velocity of the plume. When the plume's structure was destroyed, the spreading angle increased, thus enhancing the plume's lateral dispersion.

Guo et al. (2005) studied the spatial development of a momentum-driven, axisymmetric turbulent jet evolving in a turbulent background generated by an oscillating grid. They observed that the jet's evolution was disrupted by the background turbulence when the local r.m.s. velocity of the surroundings exceeded about 0.44 times that of the incident jet. At the jet's breakup location, they measured a significant increase in the lateral spreading angle, with an apparent destruction of the jet's edges. This location was also characterised by a decrease of the initially predominant axial velocity and an increase of the radial velocity with the strong horizontal spreading.

Cuthbertson et. al. (2006) followed up on the work of Guo et. al. (2005) with the study of the interaction of a vertical turbulent buoyant jet with grid-generated turbulence. They obtained similar results noting that the breakdown of the jet's structure occurred when the ratio of the r.m.s. velocities in the turbulent background and the jet was approximately 1. Within the interaction zone of the jet and the background turbulence, the edges were first destroyed by a lateral outward spreading of the jet. The core region was then arrested at a critical distance that depended on the momentum and buoyancy fluxes of the jet as well as the intensity of the turbulence background.

In the aforementioned works, the observed increase in the jet's spreading rate was argued to support the hypothesis of superposition of the dilution effects of the jet

and background turbulence. However, theoretical arguments and recent experimental measurements have come to different conclusions. The major issue with the use of oscillating grids perpendicular to the direction of the jet is that the jet is evolving (decaying) against an increasing gradient of turbulence intensity. The jet is therefore quickly destroyed and its behavior is hidden when the ratio of the jet-to-background turbulence is close to one. Moreover, the grid may even block the jet flow, explaining the lateral spreading close to the grid.

Gaskin et al. (2004) conducted an experimental study on a plane jet in shallow coflows with different levels of background turbulence. They investigated the structure of the jet as well as the mean and fluctuating components of its concentration and velocity fields. Their results showed that, when the level of background turbulence increases, the excess jet velocity decreased, whereas the scalar dilution reduced. They argued that, when the background turbulence disrupts the integral scale eddies of the jet structure, the entrainment mechanism changes from large-scale engulfment to turbulent diffusion by the smaller eddies of the background turbulence, which therefore reduces the entrainment in jets.

Khorsandi (2011) and Khorsandi et al. (2013) investigated the velocity field of an axisymmetric turbulent jet at different Reynolds numbers in a homogeneous, isotropic background turbulence with negligible mean flow. Their results showed that the mean axial velocity decayed faster in a turbulent background, compared to a jet in quiescent surroundings. They also observed an increase in the jet's width, in its mean radial velocity (especially close to the jet's edges) and in the level of turbulence in the jet. The jet's structure was destroyed more quickly at lower jet Reynolds numbers, and all these effects were more important with higher background turbulence intensities. They also measured a decrease in the jet mass flow rate, which

confirmed that the entrainment into the jet is reduced in the presence of a turbulent background.

In the same flow as Khorsandi (2011, 2013), Perez-Alvarado (2016) studied the mixing of a passive scalar field of a jet in zero-mean-flow turbulent background. Compared to a jet in a quiescent background, he found that a jet in a turbulent background has lower mean scalar concentrations near the centerline, but higher ones near the edges of the jet. The r.m.s. concentrations of the jet in turbulent surroundings are also found to increase. Using probability density functions, he showed that the highest concentrations in a jet emitted into turbulent surroundings are still larger or equal to those of a jet in a quiescent background. This contradicts the notion of superposition of the dilution effects of the jet and turbulent background. By way of flow visualizations, he explained this intermittency of the scalar field by demonstrating the increased meandering of the jet due to the background turbulence. He suggested that there exists significant lateral advection of the jet by the background large scales (the meandering) and an enhanced turbulent diffusion when the jet structure is disrupted by the background turbulence (in agreement with Gaskin et. al. 2004 and Khorsandi et. al. 2013).

Afrooz (2019) extended the work of Khorsandi (2011) and Perez-Alvarado (2016) in the study of the passive scalar mixing in turbulent axisymmetric jets in an isotropic turbulent background with zero mean flow. The location of the jet's center of mass was shown to move around the geometric center, so he measured its location to evaluate the meandering of the jet. To remove the meandering effect in the growth of the jet's width, he then calculated the radius of gyration of the scalar concentration in a jet cross-section, and he found that it was still larger in a turbulent background.

Moeini et. al. (2020) experimentally investigated the effect of a turbulent coflow on a turbulent round jet. They observed increased spreading rate, mass flow rate, velocity variances, and inward mean radial velocities close to the edges of the jet. They therefore argued that the entrainment into the jet increases with the coflow turbulence intensity. However, these results were found for low ratios of the background turbulent kinetic energy to that of the jet such as the jet was not disrupted. Measurements at higher levels of coflow turbulence were therefore suggested to extend this work.

In summary, the effect of background turbulence on turbulent jets requires additional research to resolve these issues and questions. In particular, simultaneous measurements of the velocity and scalar fields are needed to further understand the entrainment and mixing processes. It is for this reason that such measurements are undertaken in the present work.

CHAPTER 3
Experimental apparatus and instrumentation

In this section, the experimental apparatus, which consists of a heated jet of air issuing into a turbulent coflow in a wind tunnel, is described in detail. This section also contains a description of the instrumentation and the calibration of the hot-wire anemometers and cold-wire thermometer used to measure the turbulent velocities and temperatures, respectively, as well as a validation of the passive nature of the scalar field. In the subsequent six sub-sections of this chapter, the (i) wind tunnel, (ii) jet setup, (iii) combined hot- and cold-wire probe, (iv) data acquisition and analysis and (v) calibration procedures will be described, and (vi) the passive nature of the temperature field will be confirmed.

3.1 Wind tunnel

The experiments were carried out in the McGill Aerodynamics Laboratory. An open-circuit wind tunnel (described in detail by Cohen (2018) and shown in figure 3–1) was used to generate the background coflow of various turbulence intensities. The first part of the tunnel consists of a muffler followed by a Cincinnati HDBI-240 blower with a 10 hp motor. It is controlled with a variable frequency drive (ABB ACH550-UH) that sets the coflow velocity in the wind tunnel. Downstream of the blower is a transition section, connecting the blower to the flow-conditioning section by way of a contraction in the vertical plane and an extension in the horizontal one.

The flow-conditioning section is composed of a diffuser, followed by a settling chamber with screens to uniformize the flow, and a 9:1 area ratio contraction to further reduce the level of turbulence in the flow. Finally, the wind tunnel has a $40 \times 40\ cm^2$ test section in which the experiments are undertaken. It is 4.5m-long and ends with a honeycomb used to avoid external perturbations to the flow inside. The top wall of the test section slightly diverges in the vertical direction to offset the boundary-layer growth and maintain a constant centerline velocity in the wind tunnel. Multiple ports are drilled along the bottom, top and one of the two side walls at different downstream positions. They are filled with plugs when not in use. The jet and the probe (described in the next sections) were inserted into the tunnel through them in the present study.

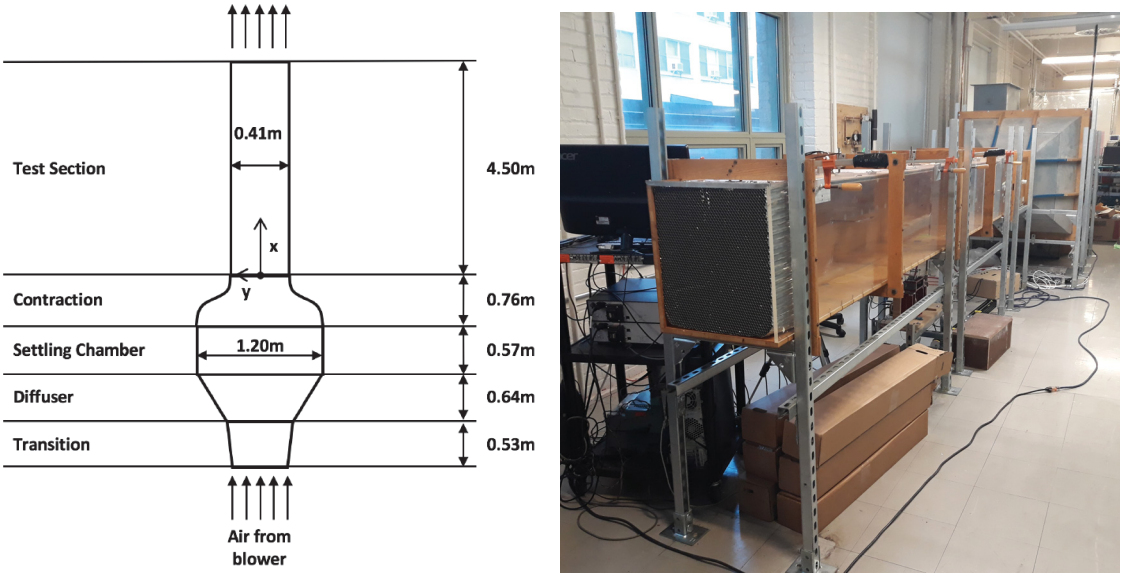

Figure 3–1: Schematic (Cohen 2018) and picture of the wind tunnel

Turbulence in the wind tunnel is generated by different grids that are inserted into the test section immediately after the contraction. Figure 3–2 shows pictures

of the two types of grids that have been employed in this study to investigate the effect of different levels of turbulence in the coflow on mixing within the jet. The lowest level of background turbulence was also studied with a quasi-laminar coflow obtained with no grid. The second level of background turbulence was obtained with a passive grid of 2-inches (5.08 cm) mesh length. Passive grids have been the main technique used to generate turbulence in wind tunnels for the last century (Simmons and Salter 1934, Stewart and Townsend 1951, Batchelor 1953, Comte-Bellot and Corrsin 1966, 1971). Such grids are composed of vertical and horizontal bars in a bi-planar configuration normal to the direction of the main flow. When turbulence is generated with grids, the flow becomes homogeneous and isotropic sufficiently far downstream of the grid ($x/M \geq 30$, where M is the mesh length of the grid, Isaza et al 2014). Unless exceptionally large wind tunnels are used, passive grids generate flows of relatively low (turbulent) Reynolds number.

Figure 3–2: Passive and active grids (Cohen 2018)

Following the work of Makita (1991), Mydlarski and Warhaft (1996) designed an active grid to be able to achieve higher levels of background turbulence in wind tunnels. Their active grid consisted of a 7x7 grid of rotating 0.64cm-diameter circular aluminium bars. 0.38mm-thick square aluminium wings were attached to the bars with static triangular wings adjacent to the walls. Holes were drilled in both the rotating and static wings near the walls to reduce the velocity deficit downstream of them and thus improve the flow's homogeneity. The mesh spacing was $M = 5.08\ cm$, so that the tunnel cross-section size was 8x8 M. Each bar was independently driven by a Superior Electric 5 W D.C. synchronous stepper motor with 200 steps per revolution. The same active grid as in Mydlarski and Warhaft (1996) was used in the present work. However, the grid controller was modernized. Specifically, the stepper motors are now connected to a controller, which is made of a combination of Arduino and Elegoo microcontrollers, as described in detail by Cohen (2018). The controller operates in a double-random asynchronous mode. Each grid bar rotates at an angular velocity Ω for a period ("cruise time") T. When this time is over, the bar reverses its direction and rotates at a new velocity for a new period. After each rotation period, the two variables Ω and T are randomly reset. This mode of operation allows the agitator wings to have a random movement and is the preferred one to generate homogeneous, isotropic turbulence using active grids (Mydlarski 2017).

Cohen (2018) partially characterized the wind tunnel flow at a single velocity. With no grid installed, three horizontal and three vertical velocity profiles at three downstream locations were taken. With passive and active grids, one horizontal and one vertical profile at two downstream positions were added. To quantify the decay of turbulence, the statistical moments of the velocity field were measured downstream

of the three grids at ten locations along the tunnel centerline. This work showed that, far enough from the grid, the flow is effectively homogeneous. Characterization of the flow was completed by Blais (2019), who measured statistical moments of the velocity field at 8 downstream locations throughout the tunnel test section, for four mean nominal velocities, with passive and active grids. Profiles with no grid in the tunnel were also taken at three downstream positions.

To further quantify the flow, the turbulence intensity (T_i) can be studied. It is defined as the ratio of the r.m.s. to mean velocity (equation 3.1). Cohen (2018) and Blais (2019) showed that the decay of T_i in the wind tunnel follows a power law, in agreement with previous results, such as those measured in Sirivat and Warhaft (1983) and Mydlarski and Warhaft (1996).

$$T_i \equiv u_{rms}/\overline{U} = \sqrt{B(\tfrac{x}{M})^n} \tag{3.1}$$

In this study, data have been taken at four distances from the grids (from 278.5 cm to 317 cm), with two different background velocities ($U_\infty = 5.5\ m/s$ and $7.5\ m/s$). Table 3–1 presents the mesh length M, the constants B and n for the two grids (from the work of Blais 2019), and the turbulence intensity T_i calculated for the four downstream positions. It can be observed that the background turbulence intensity slightly decreases with the downstream position and increases with the mean background velocity, as expected. In this study, we will consider it to be effectively constant, respectively equal to $T_i = 2.2\%$ and $T_i = 9.8\%$ for the 2" passive grid and the active grid. When no grid is installed, $T_i = 0.4\%$.

The integral length scale of the coflow (i.e. a scale characterizing the largest eddies of the flow) is defined as $l_x \equiv (\overline{u^2})^{3/2}/\epsilon$. For the two kind of grids, its value at the jet exit ($x = 257.5\ cm$) and at the four downstream positions (278.5 $cm \leq$

Table 3–1: Grids properties summary

Grid	Passive grid 2”		Active grid	
$M(cm)$	5.08			
$U_\infty(m/s)$	5.5	7.5	5.5	7.5
B	0.15	0.16	2.31	2.43
n	-1.42	-1.43	-1.36	-1.35
$T_i(\%)$ at $x = 278.5\ cm$	2.26	2.28	9.98	10.45
$T_i(\%)$ at $x = 289.5\ cm$	2.20	2.22	9.72	10.18
$T_i(\%)$ at $x = 300.5\ cm$	2.14	2.16	9.48	9.92
$T_i(\%)$ at $x = 317.0\ cm$	2.06	2.08	9.14	9.57

$x \leq 317\ cm$), for the two background velocities, was calculated from the values obtained by Blais (2019). For a given grid and background velocity, the evolution of l_x with the downstream distance is slow so the values were very similar over the range $278.5\ cm \leq x \leq 317\ cm$. The average value between the four downstream positions at which data were taken is given in table 3–2, as well as the value at the jet exit. For both grids, the integral length scale is slightly larger at the higher coflow velocity. More importantly, however, its value is about 5 times larger with the active grid than with the passive grid. In this work, the results will be presented and compared in terms of background turbulence intensity (T_i), but the integral length scale of the coflow is another parameter that can play a role in the behaviour of turbulent jets.

Table 3–2: Integral length scale

Grid	Passive grid 2”		Active grid	
$M(cm)$	5.08			
$U_\infty(m/s)$	5.5	7.5	5.5	7.5
$l_x(m)$ at the jet exit	0.032	0.038	0.17	0.19
$l_x(m)$ average for $x \in [278.5; 317]$	0.033	0.040	0.17	0.19

3.2 Jet setup

This subsection describes the jet that was designed and built for the present work. To this end, the jet air flow was conditioned and controlled before being connected to the jet that was installed inside the wind tunnel.

The jet flow conditioning apparatus starts with a compressed air flow, from which a valve and a 3/4" Amiflex flexible pipe bring air to an assembly of brass pipes and connectors, mounted on a wall and shown in figure 3–3a. There, the air is first filtered through Festo MS4 ($2\mu m$) and MS6 ($0.6\mu m$) filters, installed to remove any dust or particles that could damage the hot- and cold-wire sensors. Installed downstream of the filters was a needle valve, followed by a single scale pressure gauge (0 to 100 psi, McMaster-Carr, model number 3846K312) and an Alicat M-100SLPM-D mass flow meter, which were used to set the jet flow rate. Two different jet air velocities, $U_{jet} = 25m/s$ and $32m/s$, were chosen in this study. $U_{jet} = 32m/s$ was the highest velocity achievable with the apparatus and $U_{jet} = 25m/s$ was chosen to give rise to a significant difference in the jet's behaviour, allowing the observation of the destruction of the jet's structure within the measurement region. The clean air was subsequently heated by an Omega AHP-3741 horizontal in-line air heater, powered by a Powerstat Variable AC Transformer (model number 3PN116C, referred to as a Variac in this work) with an output voltage that could be varied from 0 to 140V. The heated air flowed from the heater to the jet by way of a 1/4" Amiflex flexible pipe.

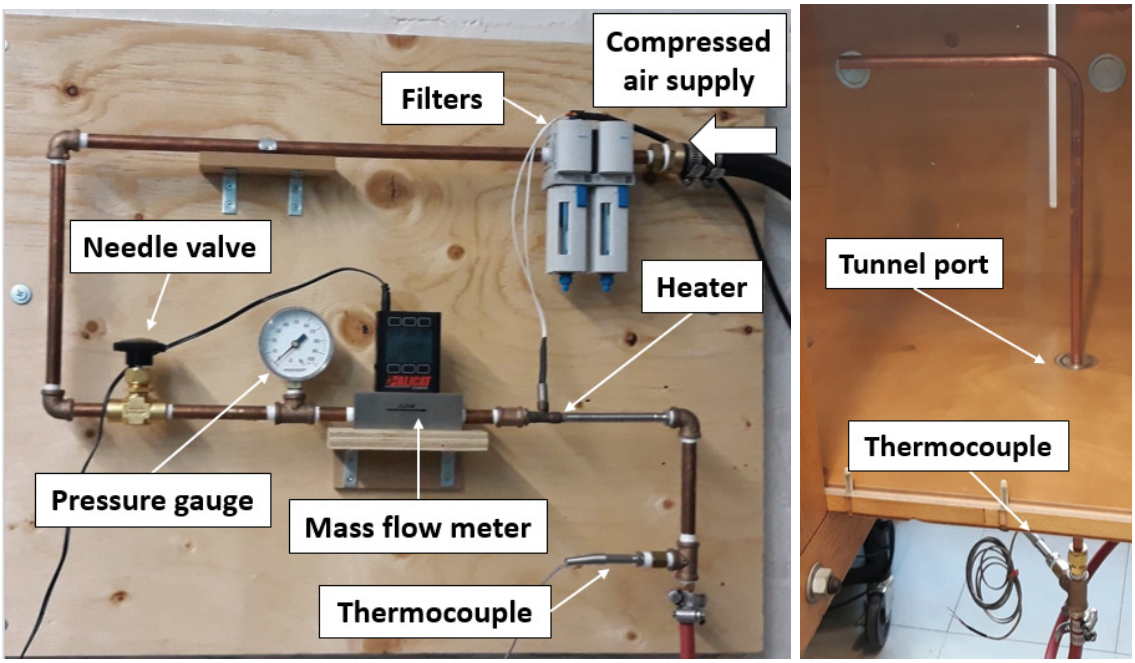

(a) Jet flow conditioning circuit (b) Jet tube

Figure 3–3: Jet set-up

The jet (shown in figure 3–3b) was made from WWG4WTG9 Acklands-Grainger copper tubing which was 60 cm long and had a diameter (D) of 8 mm. The Reynolds numbers associated with the two different jet velocities used in this work were therefore $Re = 12900$ and $Re = 16300$, respectively. The tube was bent at 90° and inserted into the wind tunnel through one of the ports. It was mounted vertically from the bottom wall and installed 240 cm downstream of the grid. This distance is larger than 30 times the grid mesh size M to be in the fully homogeneous isotropic region of the background flow. The jet tube was bent at 90° with a radius of curvature $R_c = 15/16" = 2.38\ cm$. The Dean number ($De = Re\sqrt{\frac{D}{2R_c}}$) was respectively equal to $De = 5300$ and 6700 for the two jet Reynolds numbers. When the air flows through the bend, static pressure perturbations appear and secondary flow cells are

introduced. For flows with a Dean number of 6400, a straight section with a minimum length of five times the tube diameter is needed after the bend for the flow to recover (Ferdman et al. 2000, Enayet et al. 1982). In this work, the length after the bend was 17.5 cm, which corresponds to 21 times the jet diameter. The entrance length (the length after which the flow becomes fully-developed) for a turbulent flow in a pipe is $L = 1.36 \cdot D \cdot Re^{1/4}$ (Cengel and Cimbala 2006), resulting in $L = 11.6\ cm$ and $12.3\ cm$, respectively for the two jet Reynolds numbers in this work. This length was achieved in the jet tube both before ($43.5\ cm$) and after the bend, so the flow at the jet's exit was fully-developed.

To provide a heated jet, the output voltage of the Variac had to be chosen wisely to find a balance between (i) keeping the scalar passive and not burning the heater or overheating the pipe, and (ii) having a good signal-to-noise ratio with large enough r.m.s. temperature values (θ_{rms}). The temperature difference ΔT (K) between the inlet and the outlet of the heater is linked to the air flow rate Q ($m^3 \cdot s^{-1}$) and the power P (W) by the relation

$$P = \rho \cdot c_p \cdot Q \cdot \Delta T \tag{3.2}$$

where $\rho = 1.2\ kg \cdot m^{-3}$ (the density of air) and $c_p = 1006\ J \cdot kg^{-1} \cdot K^{-1}$ (the specific heat capacity of air at 300K). The maximum power that could be supplied to the heater was approximately $P_{max} = 250 - 300W$ for the two chosen jet air velocities, which corresponds to a ΔT up to $200°C$ between the inlet (at room temperature $\approx 20°C$) and the outlet of the heater. As some elements in the apparatus could not bear temperatures higher than $100°C$, this was not the limiting factor. However, heat losses through the pipe between the heater exit and the jet had to be taken into account. After a few tests, the Variac output voltage was set to 100V. Knowing that

the heater resistance was approximately $R = 75\Omega$, the corresponding input power was therefore 133W. After a warming time of approximately 45 minutes, steady-state temperatures around $25-30°C$ were achieved at the jet exit. Knowing that the mean temperature values measured in the background flow varied between 20 and 23°C, it ensured temperature differences between the jet and the background that were large enough to be accurately measured by the cold-wire.

To record the temperature in the jet air supply circuit, two fixed type-E Omega TC-E-NPT-U-72 thermocouples were mounted downstream of the heater and at the entrance of the jet tube. The temperature at the jet exit was measured by a third thermocouple, a quick-disconnect type-E Omega EMQSS-062E-12, which was removed when data were taken, to not disturb the jet flow. An Omega DP63300-TC digital panel thermocouple meter was used to display and measure the temperature. Using thermocouple connectors and an extension grade wire (Omega), the three thermocouples could be individually connected or disconnected to the meter to record the air temperature in the circuit when needed.

3.3 The combined hot- and cold-wire (X-T) probe

The goal of this work was to study the velocity and scalar mixing of an axisymmetric turbulent jet in a turbulent coflow. Hot-wire anemometry (HWA) and cold-wire thermometry (CWT) were the two techniques used for this purpose. As described in detail by Bruun (1995), these relatively low-cost and compact techniques have many advantages. In particular, they have a high frequency response and spatial resolution, allowing for the measurement of length scales on the order of the smallest (Kolmogorov) scale ($< 1\ mm$), at frequencies up to several kiloHertz. They

are regularly used to measure instantaneous velocity and temperature variations in a fluid flow at a given point, with high signal-to-noise ratio.

Hot-wire anemometry relates the convective heat transfer from a heated wire element placed in a flow to the flow's velocity. A cylindrical sensor is electrically heated, at a temperature higher than that of the flow, by a constant temperature anemometer (CTA). A continually correcting Wheatstone bridge within the anemometer keeps adjusting the anemometer's output voltage to compensate the heat transfer and maintain the wire at a constant temperature (and resistance). The operating resistance of the heated sensor is equal to the resistance of the same wire at the ambient temperature, multiplied by a factor called the overheat ratio. According to Bruun (1995), this overheat ratio has to be well chosen to find a balance between achieving a high velocity sensitivity and avoiding oxidization of the sensor itself. In this work, an overheat ratio of 1.8 was used, which is a typical value employed for tungsten hot-wires.

In cold-wire thermometry, a constant current is passed through a sensor to infer the flow's temperature. This technique exploits the fact that the wire resistance, and therefore the anemometer output voltage, changes linearly with temperature (for small enough temperature changes). The size of the wire is so small (0.6 μm) that it responds rapidly to changes in the temperature of the flow. A constant current anemometer (CCA) is used and the current is kept at a low value ($100\mu A$) in order for the wire to not be sensitive to changes in the velocity of the flow.

To simultaneously measure the U- and V-velocities, as well as the temperature of the air, three wires were needed: two hot-wires and one cold-wire. For practical reasons related to the geometry and size of the wind tunnel ports, it was not possible to use two separate probes, such as an X-wire (a type of probe that can measure

the flow's velocities in two spatial directions) and a cold-wire. Therefore, a sensor with three wires on one probe, which will be referred to as the X-T probe, had to be designed and built.

A TSI 1294DG-60 probe was used as the basis for the X-T probe, but it had to be modified as it was originally made to measure velocities in three spatial directions. Initially in a triangle shape, the three pairs of prongs (to which the sensor wires were attached) were carefully bent to place them side by side and form two rows, as shown in figures 3–4 and 3–5. The three wires were then soldered between the pairs of prongs. The first and second wires were two hot-wires, inclined at $\pm 45°$ to form an X-wire and measure velocity in two spatial directions. They were made of 5 μm diameter tungsten wires and separated by 1 millimeter. The third wire was a cold-wire, used to measure temperature, and made of a 0.625 μm diameter platinum wire. It was oriented normal to the flow, and located 1.5 millimeter apart from the second wire and slightly upstream in order for the cold-wire sensor to not be affected by the heated wake of the hot wires.

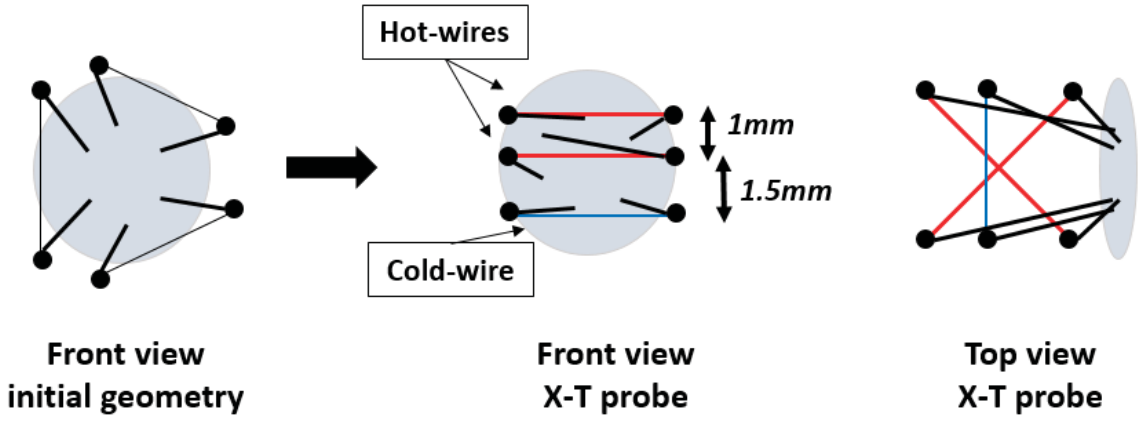

Figure 3–4: Schematic of the X-T probe

The resistance of a wire element at a uniform temperature is given by $R = \frac{\chi \cdot l}{A_w}$ (Bruun 1995), where χ is the wire resistivity (resistance per unit length (l) and per unit cross-sectional area (A_w)). At $20°C$, the resistivity of the two tungsten wires is equal to $\chi = 5.5\ \mu\Omega \cdot cm$ and the resistivity of the platinum wire is equal to $\chi = 9.8\ \mu\Omega \cdot cm$. The length to diameter ratios of the sensors had to be large enough ($l/d \geq 200$) to obtain a flat temperature profile between each pair of prongs of the probe (Bruun 1995). On the other hand, a hot-wire cannot resolve motions at smaller scales than itself, and its length should ideally not be longer than the Kolmogorov microscale, which was around $\eta = 4 \times 10^{-4}\ m$ in this flow. The typical lengths for hot- and cold-wires used in this work were respectively 1 mm and 0.5 mm, which resulted in resistances of about $R = 3\ \Omega$ for the hot-wires and $R = 150\ \Omega$ for the cold-wire.

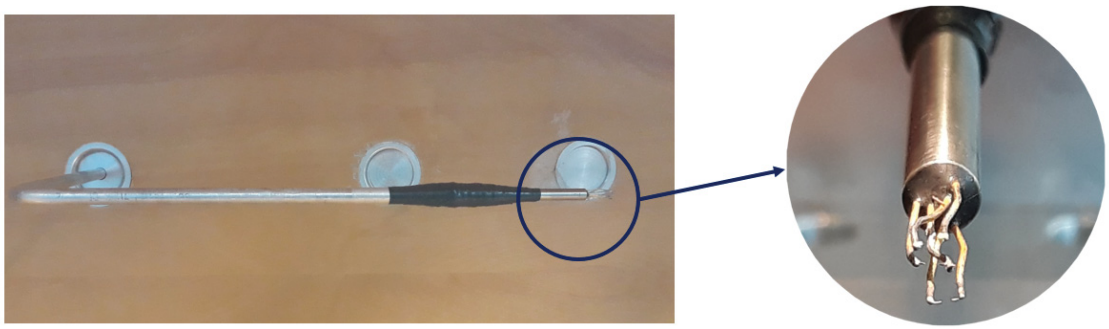

Figure 3–5: Picture of the X-T probe

A probe support was designed to be able to install the 3-wire probe in the wind tunnel. The TSI probe was 15 cm long with three 137-cm-long pairs of wires, each linked to a pair of prongs to which the hot- and cold-wires were soldered. A 91cm-long aluminium tube, with a diameter of 46 mm, was bent at 90° and the probe was inserted and fixed into it. The sensors were positioned horizontally to measure the jet velocities in the x- (axial) and y- (radial) directions. The 6 wires exiting the other end

of the aluminium tube were soldered to BNC connectors. This tube containing the probe was mounted on a MN10-0050-M02-21 Velmex Bislide traversing mechanism (accuracy of 0.076 mm over the entire travel distance) with a Vexta PK264-03A-P1 Stepper Motor, placed on a tripod next to the tunnel. It thus enabled motion of the probe in the y-direction to obtain velocity and temperature profiles spanning the entire jet width, as depicted in figure 3–6.

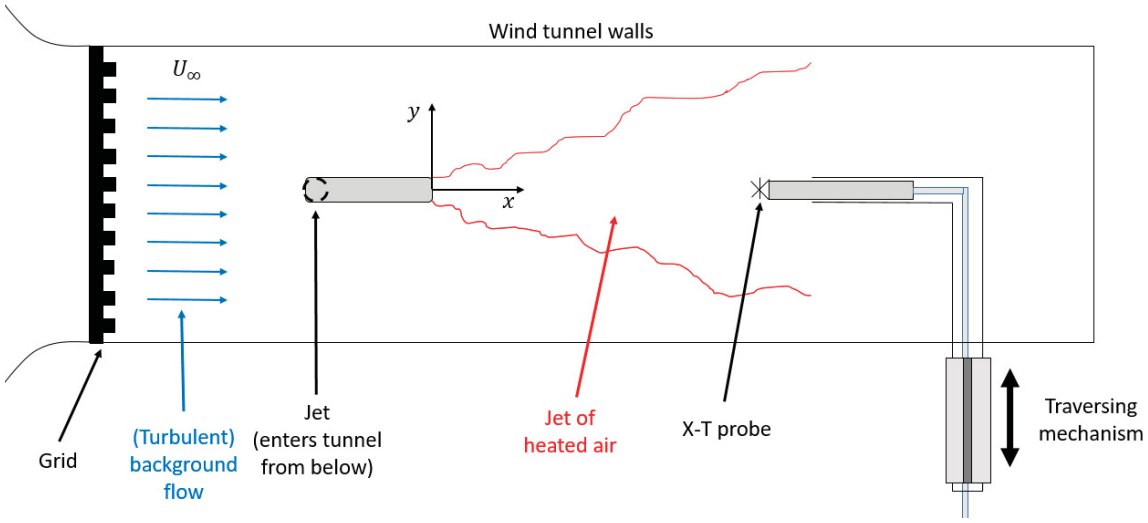

Figure 3–6: Experimental apparatus schematic, top view

3.4 Data acquisition and analysis

The hot-wires were operated using two DANTEC 55M10 constant temperature anemometers (CTA). 5-meter cables were needed to connect the wires to the anemometers. Given that the cables of the X-T probe already measured 1.37 meter, two 4-meter cables were connected to the probe's BNC connectors and the 37 centimeters in excess were compensated in the anemometer settings. The two hot-wires' resistances at ambient temperature were measured with the anemometers and multiplied by the 1.8 overheat ratio to obtain the operating resistances. The cold-wire was

operated with a constant current anemometer (CCA) built at the Université Laval (Quebec, Canada) (Lemay and Benaïssa 2001). The cable length between the probe and the CCA has minimal impact on the result so 5-meter cables were used.

The output voltages of the three anemometers were high- and low-pass filtered using a four-channel Krohn-Hite 3384 filter and a two-channel Krohn-Hite 3382 filter. The mean voltages and the fluctuating components of the signals were recorded separately. The high-pass filter frequency was set to 0.1 Hz to remove the DC components of the signals and to be able to amplify their fluctuating components. The Kolmogorov frequency of the flow was estimated for each data point using LabVIEW with a real-time spectrum analyzer, and the low-pass filter frequency was set slightly above it to eliminate high frequency noise. The filters were also set to amplify the high-pass filtered signal with a 20 dB gain in order to fully use the $\pm 5V$ data range of the 16-bit National Instruments PCI-6036E, DAQ A/D board and have the best resolution.

The outputs of the filtered signals were connected to a Tektronix TDS 1002 oscilloscope (to monitor the signal from each channel), and then to a National Instruments BNC-2110 BNC connector block. The signals were finally digitized by the A/D board. To control and acquire the data, LabVIEW 7.0 VIs (Virtual Instruments) were used. At each data point, measured at different radial locations in the jet, the statistical moments of the velocities and temperature were recorded. The data sets consisted of 61440 samples at a sampling frequency of 200Hz. Additional spectral data sets consisted of 1638400 data points. According to the Nyquist criterion, they were sampled at twice the low-pass filtering frequency. The acquired output data from the anemometers were voltages. To convert them into velocities and temperature, a computer code written in FORTRAN 90 was used. With the

calibration constants as inputs, it could calculate statistical moments, spectra or probability density functions (PDFs). Matlab programs were then written to analyze these statistics and visualize the data.

3.5 Calibration procedures

The methods used for the cold-wire and the hot-wires were different, however they were all calibrated with the TSI 1128 Air Velocity Calibrator. It produced a steady and laminar flow to perform the calibrations. A differential pressure transducer was used to measure the pressure difference between the jet plenum and its exit, which was then converted into a voltage. The latter was read by a multimeter and then converted into a velocity with a LabVIEW VI. The pressure in the jet's plenum, and therefore its velocity, were controlled by a valve. The calibration jet flow was heated by a 120V electric heating system.

3.5.1 Hot-wire calibration

Before their calibration, the newly-made hot-wires had to be 'aged' or 'burned in'. As they operate at high temperature, the hot-wires material properties need to reach a steady-state before being used. This step was done by operating the hot-wires for 24 hours prior to calibration and use. The hot-wires had to be aged only once before the first calibration, but this step needed to be repeated each time a hot-wire was broken and repaired.

The output voltages E_1 and E_2 of the two constant temperature anemometers can be respectively related to the velocities U_1 and U_2 over the hot wires using King's

Law:

$$E^2 = A + BU^n \tag{3.3}$$

In equation 3.3, n is a constant, but A and B depend on the temperature. As the flow under study had a variable temperature, we had to compensate the hot-wires for the effects of the non-isothermal flow. Lienhard (1988) proposed the following forms for A and B:

$$A = \overline{A}\ (T_{w,a} - T)\ (\tfrac{T+T_{w,a}}{2})^{0.84} \tag{3.4}$$

$$B = \overline{B}\ (T_{w,b} - T) \tag{3.5}$$

with $\overline{A}$, $\overline{B}$, $T_{w,a}$ and $T_{w,b}$ being four constants (and $T_{w,a}$ and $T_{w,b}$ representing the operating temperatures of the two hot wires). The first step for the calibration of the two hot wires was therefore to obtain the values of the five constants of King's Law. The probe was installed vertically (0° angle) above the calibration jet in the direction of the mean flow. The electric heating system was turned on to achieve the chosen temperature. This temperature was maintained while the output voltages of the anemometers were recorded for velocities from 2 to 20 m/s (chosen so that the velocities measured in the jet under study fell within this range). Five calibrations were performed at five different temperatures. The temperature variation during one calibration was kept to less than $1°C$. A least-squares fit was used to obtain the voltage versus velocity (E^2 vs U) calibration curves for the two inclined hot-wires at each temperature. Typical calibration curves for one wire are shown in figure 3–7.

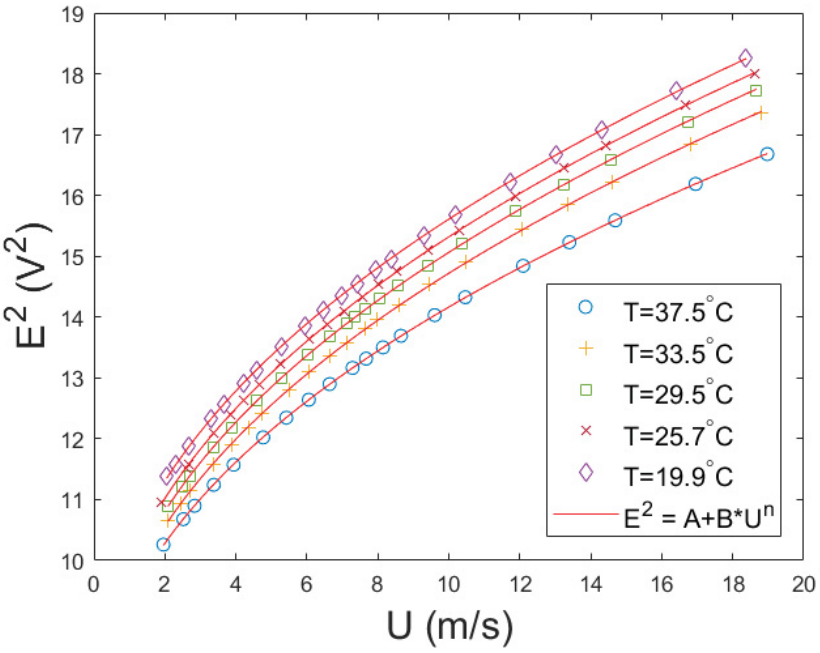

Figure 3–7: King's Law calibration for one hot-wire at different temperatures

As the hot-wires were not perpendicular to the flow but inclined at an angle close to $\pm 45°$, they were cooled down by both the longitudinal and transverse components of the flow. One therefore needs to determine the longitudinal and transverse velocity components ($\tilde{U}$ and $\tilde{V}$) from U_1 and U_2. To this end, the effective angle method described by Browne et al. (1988) was followed. Considering one of the two inclined hot-wires, the effective velocity (U_{eff}) is defined as the velocity that would produce the same output voltage from the anemometer as U if the wire were normal to the flow:

$$U_{eff} = U \cdot f(\theta_{eff}) \tag{3.6}$$

In this equation, $f(\theta_{eff}) = (cos^2(\theta_{eff}) + k^2 \cdot sin^2(\theta_{eff}))^{1/2}$ and the constant k^2 (representing the effects of longitudinal cooling) was set to 0.03 (Browne et al. 1988). The

effective angle θ_{eff} for each of our two hot-wires was then calculated with a yaw calibration. At one fixed velocity, the output voltages of the anemometers were recorded with the wires at different angles to the direction of the mean flow. From the vertical position (0° angle) above the calibration jet, the probe was inclined to 9 yaw angles from $-24°$ to $+24°$ in increments of 6°. Because θ_{eff} is effectively independent of temperature, this calibration was done at ambient temperature and the velocity was chosen to be close from the mean velocity of the jet during the experiments. The effective angle, respectively θ_{eff_1} and θ_{eff_2}, of each hot-wire were then calculated by averaging the values obtained for every yaw angle.

Assuming that the two inclined hot-wires experience the same instantaneous velocity S, at an angle β from the mean flow direction (see figure 3–8), and that the effective velocity due to S is the same as the effective velocity due to U, the following equations are obtained:

$$U_1 \cdot f(\theta_1) = S \cdot f(\theta_1 - \beta) \tag{3.7}$$

$$U_2 \cdot f(\theta_2) = S \cdot f(\theta_2 + \beta) \tag{3.8}$$

These equations were solved for S and β and could then be used to determine the longitudinal ($\tilde{U} = S \cdot cos(\beta)$) and transverse ($\tilde{V} = S \cdot sin(\beta)$) velocity components.

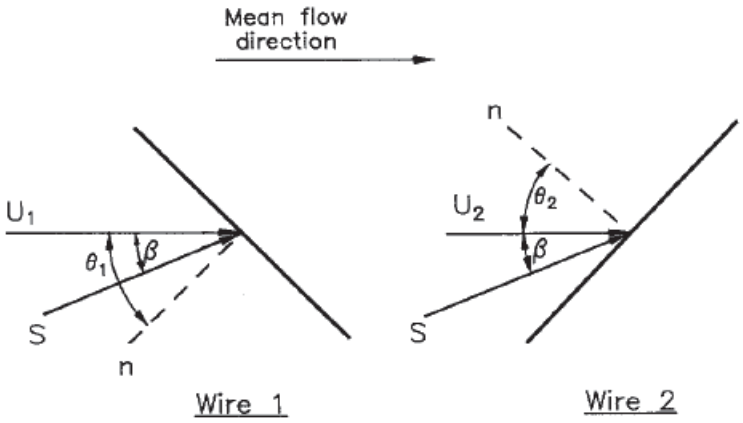

Figure 3–8: Side-view of the hot-wires shown separated, for the yaw calibration (figure from Browne et al. 1988)

Table 3–3 shows typical calibration constants obtained for the two hot-wires of the X-T probe.

Table 3–3: Typical hot-wire calibration constants

Wire	1	2
n	0.44835	0.44265
$\overline{A} \times 10^4$	2.459	2.605
$\overline{B} \times 10^2$	2.372	2.547
$T_{w,a}(K)$	485.3	476.2
$T_{w,b}(K)$	426.1	419.6
$\theta_{eff}(^\circ)$	40.067	30.652

3.5.2 Cold-wire calibration

The cold-wire operates at the flow temperature so aging is not needed and it can be calibrated right after being soldered to the probe.

Before starting the calibration itself, the dynamic compensation, current and gain of the constant current anemometer (CCA) were adjusted. The dynamic compensation was done by using a square wave generator. The goal was to minimize the effect of a perturbation on the CCA's output signal. To adjust the current, a resistor box was connected between the CCA input and a voltmeter. Then, the current value had to be chosen so that it was small enough to minimize the sensor's sensitivity to velocity but large enough to have a good signal-to-noise ratio. For a $0.625\mu m$ diameter cold wire, the recommended current is 0.10 mA (Lemay 2001). The gain was lastly set to optimize the output voltage span and to clearly read the slope between the CCA output voltage and the flow temperature. The CCA input was connected to the resistor box and its output to a voltmeter.

The response of the cold-wire to a temperature variation depends on its cut-off frequency ($f_c = \frac{1}{2\pi\tau_w}$), where τ_w is the cold-wire time constant. To have a good temporal resolution of the temperature fluctuations, f_c should not be significantly smaller than the highest frequency in the flow (the Kolmogorov frequency), which was around 5 kHz in this study. The current injection technique proposed by Lemay and Benaïssa (2001) was used to measured the wire time constant τ_w. The CCA output voltage was recorded while the square wave generator was turned on. This way, the wire was periodically exposed to a high current, which made its temperature rise above the ambient temperature, and then forced to cool down by convection. This cooling period was fitted as an exponential decay with the following equation, proposed by Lemay and Benaïssa (2001):

$$E = C_1 \cdot e^{-t/\tau_E} + C_2 \cdot e^{-t/\tau_w} + C_3 \tag{3.9}$$

where $\tau_E = 3\mu s$ is the electronics time constant (Lemay and Benaïssa 2001) and C_1, C_2 and C_3 are three constants. For our cold-wire, we obtained a cut-off frequency value around 4.6 kHz.

For the cold-wire calibration, the goal was to know the relation between the constant current anemometer (CCA) and the flow temperature. To this end, the calibration jet was warmed up by the electric heater, which was then turned off to let the flow slowly cool. The velocity was set to a constant value around $10m/s$, which is close to the mean velocity of the experiment. When the temperature was around $30°C$, the calibration could begin. The CCA output voltage (E) and the jet exit temperature (T) were simultaneously recorded every $0.5°C$ for about 15 points. Figure 3–9 shows a typical calibration curve in which we see a linear relation between E and T of the form:

$$E = C \cdot T + D \tag{3.10}$$

where C and D are calibration constants determined by a least-squares fit to the calibration data.

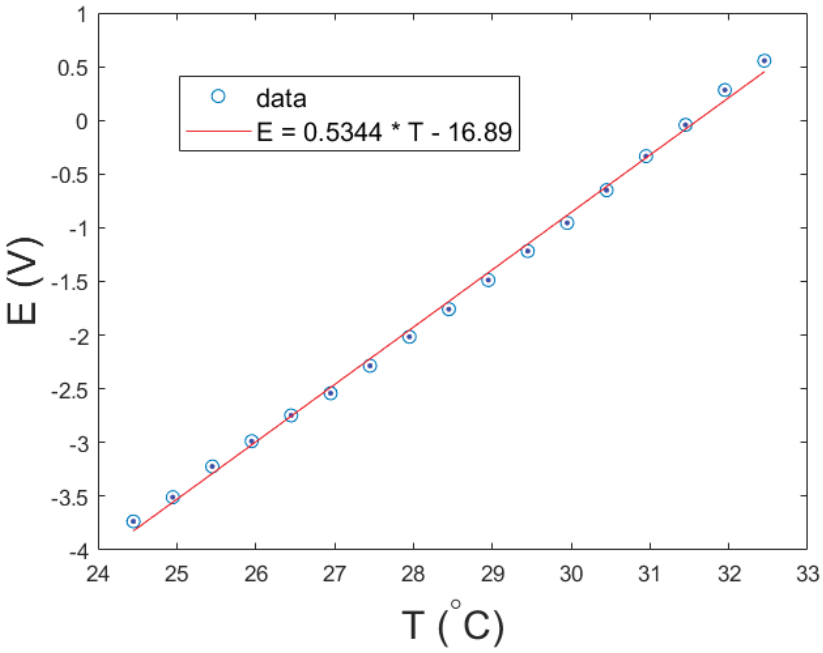

Figure 3–9: Typical cold-wire calibration

3.6 Passivity of the scalar

A scalar is considered to be passive when its concentration is small enough to have no significant dynamical effects on the fluid motion by way of density differences in the flow (and negligible ensuing buoyancy effects). In this work, we need to ensure that temperature difference between the jet and the coflow is sufficiently small to be justly deemed a passive scalar. To this end, the influence of the scalar field on the velocity field is quantified by (i) comparing the mean and r.m.s. velocity profiles for isothermal and heated jets, and (ii) comparing the ratio of the buoyant production rate of turbulent kinetic energy to its dissipation rate (per unit mass).

Figure 3–10 compares the mean and r.m.s. radial profiles of the U- and V-velocities for (i) an isothermal jet (at the same ambient temperature as the coflow),

and (ii) a heated jet with a mean temperature difference of $2.5°C$ at the jet's centerline. With the exception of the jet's temperature, both data sets were taken under the same experimental conditions, with a turbulence intensity (T_i) of 0.4%, at $x/D = 26.5$, with $U_{jet} = 32m/s$ and $U_\infty = 5.6m/s$. As concluded from figure 3–10, there is no significant difference in the measured velocity field between the isothermal and heated jets; the variations are within experimental error, which is a first confirmation of the passive nature of the scalar field.

The second method to quantify the effect of the scalar field on the fluid motion is the estimation of the ratio of the buoyant production of turbulent kinetic energy ($g_i\overline{u_i\theta}/\overline{T}$) to the dissipation rate of turbulent kinetic energy per unit mass (ϵ), which are both terms in the turbulent kinetic energy budget. Given that the jet is axisymmetric, this ratio is approximated by $(g\ \overline{v\theta})/(\overline{T}\ \epsilon)$. The gravitational vector is in the z-direction in the present experiments but measurement of the velocity fluctuations in this direction were not undertaken due to the design of the wind tunnel. To estimate the dissipation rate of turbulent kinetic energy, the assumption of local isotropy is used along with Taylor's frozen flow hypothesis (given that $u_{rms}/\overline{U} << 1$), to obtain $\epsilon = \dfrac{15\nu}{\overline{U}^2}\overline{\left(\dfrac{du}{dt}\right)^2}$. The values obtained for the ratio of buoyant production to dissipation of turbulent kinetic energy for this flow were less than 1%. This result therefore also confirms that the effect of buoyancy remains small and that the scalar can be deemed passive.

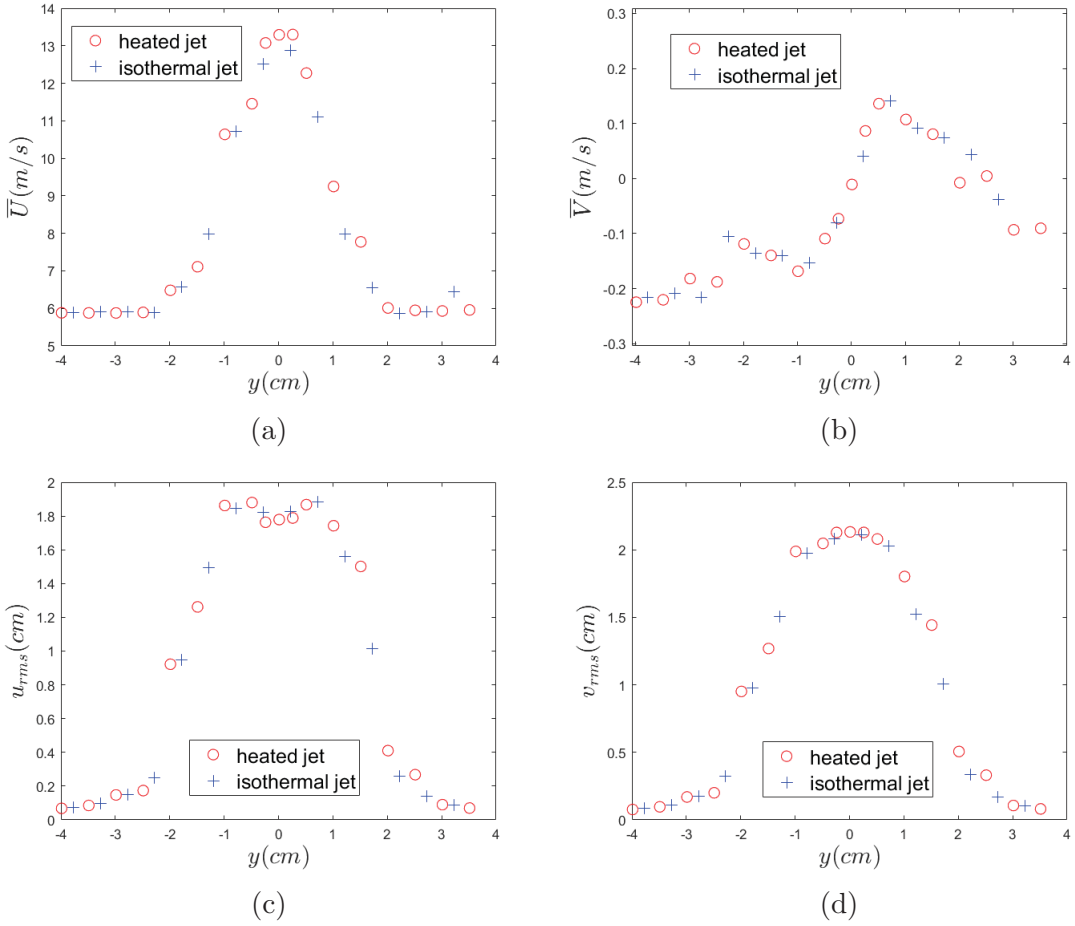

Figure 3–10: Mean axial (a) and radial (b) velocities, and r.m.s. axial (c) and radial (d) velocities for a heated ($\circ$) and isothermal ($+$) jet ($T_i = 0.4\%$, $x/D = 26.5, U_{jet} = 32m/s$ and $U_\infty = 5.6m/s$).

CHAPTER 4
Results and discussion

The present chapter begins with a validation of the measurement technique used herein. However, the main part of this chapter presents measurements of the evolution of a heated turbulent jet released into coflows with three levels of background turbulence. 48 cases are investigated, consisting of data sets measured at 4 downstream distances, with 2 jet velocities and 2 coflow velocities, at the 3 aforementioned levels of background turbulence. Results are presented and the (mean and r.m.s.) velocity and temperature fields, combined velocity-temperature statistics, spectra, probability density functions (PDFs), and conditional expectations of the velocity and temperature fields are discussed. Transverse (radial) profiles of the different quantities were measured along the y-direction (Cartesian coordinate system), with $y = 0$ corresponding to the centerline of the axisymmetric jet. In this chapter, we therefore denote the radial position as y instead of r, as measurements are made for both positive and negative values of y.

For each level of background turbulence, attempts were made to keep the background velocity (U_∞) the same from case to case. Despite this effort, the measured background velocity varied slightly between the data sets. To avoid unnecessary complications in the presentation of the results, data are quoted at the average background velocities in conjunction with the two jet exit velocities, which are tabulated

in table 4–1. Moreover, this table summarizes the four nominal ratios of the jet-to-background mean velocities ($\lambda = U_j/U_\infty$) that were studied in this work[1] .

Table 4–1: Jet-to-coflow velocity values.

$U_j(m/s)$	25	32	25	32
$U_\infty(m/s)$	7.4	7.5	5.5	5.6
λ	3.4	4.3	4.6	5.7

4.1 Measurement technique validation

In this section, results obtained for a jet issuing into a nominally laminar background flow ($T_i = 0.4\%$) are compared with previous studies of turbulent jets also issuing into laminar coflows. Antonia and Bilger (1973) (herein referred to as AB), Smith and Hughes (1977) (SH), and Chu et al. (1999) (CLC) made measurements of the velocity field. Only Antonia and Bilger (1973) specified the turbulence intensity of their coflow, which was equal to 0.1%. The techniques used in these studies to measure the fluid's velocities (hot-wire anemometry (HWA), Pitot-static tube (PT) and laser Doppler anemometry (LDA)), are summarized in table 4–2.

[1] The values of λ were calculated with three significant digits in the values of U_∞ and U_j, even if only two are displayed in table 4–1. The values of U_j, U_∞ and λ for each of the 48 cases are tabulated in Appendix A

Table 4–2: Overview of the works used in the validation of the measurement technique (velocity field).

	PW	AB	SH	CLC
Technique	HWA	PT / HWA	HWA	LDA
λ	3.4, 4.3, 4.6, 5.7	3.0, 4.5	1.75, 3.5	[11.3-19.8]
Re_j	12900, 16300	32100, 48200	117000, 233000	[6000-11000]

Results for the scalar field will be compared with the works of Chu et al. (1999) (CLC) and Davidson and Wang (2002) (DW). As summarized in table 4–3, both studies employed laser-induced fluorescence (LIF) to measure concentration in the flow, whereas temperature was the scalar under consideration in the present work (PW), which was measured by way of cold-wire thermometry (CWT).

Table 4–3: Overview of the works used in the validation of the measurement technique (scalar field).

	PW	CLC	DW
Technique	CWT	LIF	LIF
λ	3.4, 4.3, 4.6, 5.7	[8.8-20.5]	[9.7-70.9]
Re_j	12900, 16300	[6000-11000]	[1900-5100]

Note that the majority of the comparisons are made with data for which $\lambda = 3.4$, as this value is the closest to that used in the previous works with which a comparison will be made.

Figure 4–1 depicts the mean velocity excess ($\Delta\overline{U} = \overline{U} - U_\infty$), normalized by its value at the centerline ($\Delta\overline{U}_c = \overline{U}_c - U_\infty$), plotted as a function of the radial position (y), normalized by the half-width of the mean axial velocity excess profile ($y_{1/2_{\Delta\overline{U}}}$).

In general, the half-width ($y_{1/2}$) of a quantity is defined as the radial position at which the quantity falls to half of its centerline value. Gaussian curve fits to data from the aforementioned investigations are compared with the results of the present work at four downstream positions with $\lambda = 3.4$. The data points at the different x/D collapse onto one single curve, confirming that the mean axial velocity excess profiles are (i) self-similar at these downstream positions, and (ii) consistent with the data of the three other studies.

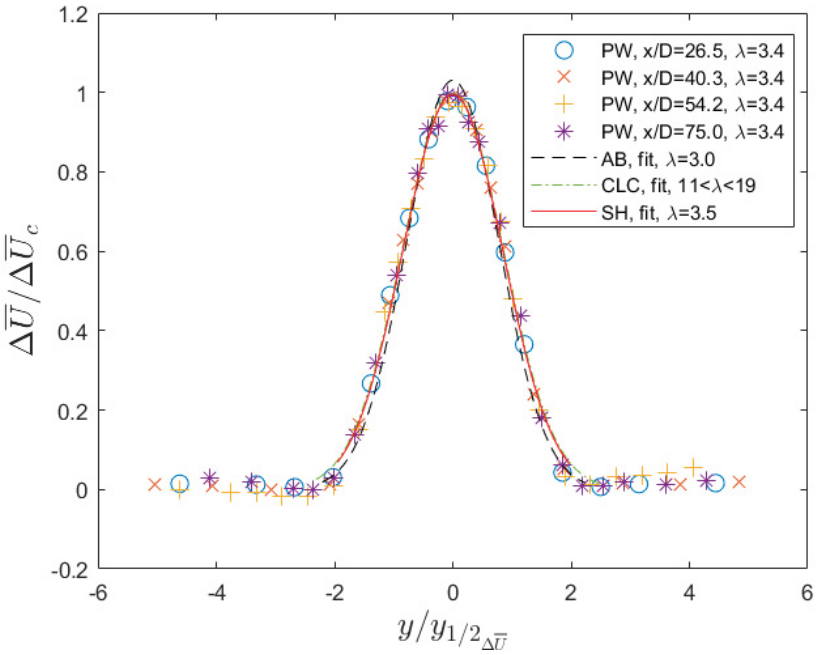

Figure 4–1: Radial profiles of the mean axial velocity excess for turbulent jets issued into nominally laminar coflows.

In figure 4–2, the downstream evolutions of both the centerline mean axial velocity excess (normalized by its value at the jet exit, $\Delta U_j = U_j - U_\infty$, figure 4–2a) and the half-width of the mean axial velocity excess of the present work, for $\lambda = 3.4$ and 4.3 (figure 4–2b), are compared with the results of Antonia and Bilger (1973) for $\lambda = 3.0$

and 4.5. (The majority of the data of Smith and Hughes (1977) were taken at smaller x/D than the data of Antonia and Bilger (1973) and the present work. Because the jet may not be fully developed at these downstream distances ($4 \leq x/D \leq 40$), their data were not used to validate the present downstream evolutions of ΔU_j and $y_{1/2_{\Delta\overline{U}}}$, given the differences in the evolution of the jet this causes). Both evolutions approximately follow a power law (decay and growth, respectively), so the data were fit by least-squares to power law curve fits ($\Delta\overline{U}_c/\Delta U_j = A_1(x/D)^{n_1}$ and $y_{1/2_{\Delta\overline{U}}}/D = A_2(x/D)^{n_2}$). For simplicity in this work, we chose to set the virtual origin to zero for every power law. Table 4–4 summarizes the best-fit decay/growth exponents (n_1 and n_2). Similar to a jet in a quiescent background, the values of $\Delta\overline{U}_c/\Delta U_j$ approximately decay as x^{-1}. The agreement is better for larger values of λ, which is consistent with the fact that a jet in a quiescent background corresponds to the limit $\lambda \to +\infty$. The results of the present validation are in good agreement with the previous studies for the evolution of the half-width of the mean axial velocity excess, which approximately grows as $x^{0.6}$.

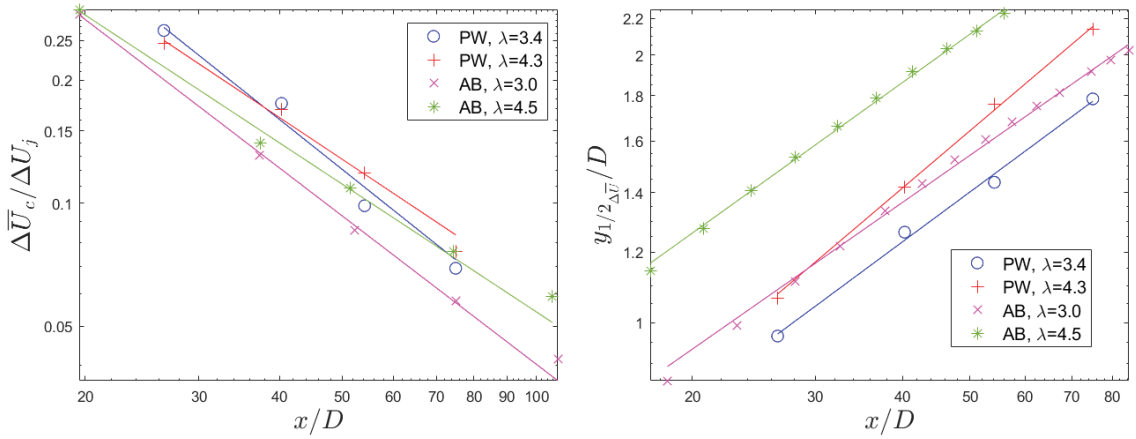

(a) (b)

Figure 4–2: Downstream evolution of the normalized centerline mean axial velocity excess (a) and the half-width of the mean axial velocity excess (b) for turbulent jets issued into nominally laminar coflows.

Table 4–4: Power law decay/growth exponents (n_1 and n_2) for $\Delta\overline{U}_c/\Delta U_j$ and $y_{1/2_{\Delta\overline{U}}}/D$ for turbulent jets issued into nominally laminar coflows

	PW		AB	
	$\lambda = 3.4$	$\lambda = 4.3$	$\lambda = 3.0$	$\lambda = 4.5$
$\frac{\Delta\overline{U}_c}{\Delta U_j} = A_1(\frac{x}{D})^{n_1}$	-1.26	-1.05	-1.21	-1.04
$\frac{y_{1/2_{\Delta\overline{U}}}}{D} = A_2(\frac{x}{D})^{n_2}$	0.58	0.67	0.55	0.56

The radial profiles of the r.m.s. axial velocity (u_{rms}) are depicted in figure 4–3 (for the four values of x/D and $\lambda = 3.4$) and compared with the results of Antonia and Bilger (1973) at $x/D = 38$ and 76 ($\lambda = 3.0$), and Smith and Hughes (1977) at $x/D = 26$ and 40 ($\lambda = 3.5$). The radial position is non-dimensionalized by the half-width of the mean axial velocity excess (as in figure 4–1). When normalized by the centerline value ($u_{rms,c}$), the data are in good agreement, except for the magnitude

of the off-axis peaks. Although present in the current work and that of Antonia and Bilger (1973), the double peaks are less visible than in the data of Smith and Hughes (1977). This may be related to the slightly larger value of λ and by the level of background turbulence intensity (which is not specified) in Smith and Hughes (1977). Indeed, the more the jet is impacted by the turbulent background, the faster these double peaks disappear (to be discussed shortly).

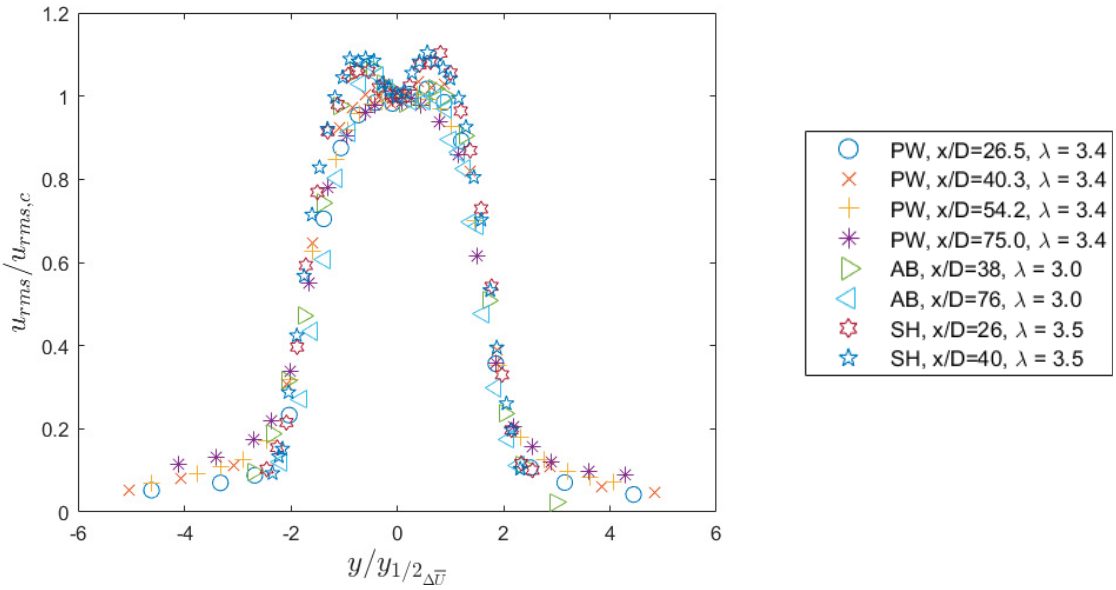

Figure 4–3: Radial profiles of the r.m.s. axial velocity for turbulent jets issued into nominally laminar coflows.

The radial profile of the r.m.s. radial velocity (v_{rms}) was only presented in Smith and Hughes (1997), and for $\lambda = 1.75$ – lower than any value studied herein. Their results are compared with the results of the present work at the four downstream positions for $\lambda = 3.4$, in figure 4–4a. When normalized by the centerline value of v_{rms}, the profile of Smith and Hughes (1997) is slightly larger at the center of the jet, but otherwise in good agreement with the present work.

Figure 4–4b depicts the radial profile of the mean Reynolds stress ($\overline{uv}$), normalized by the product of the centerline axial and radial r.m.s. velocities. The present data measured at $x/D = 40.3$ with $\lambda = 3.4$ are compared with the data presented in Antonia and Bilger (1973) at $x/D = 30$ with $\lambda = 3.0$, and in Smith and Hughes (1977) at $x/D = 40$ with $\lambda = 1.75$ (they did not present this result for $\lambda = 3.5$). The value of $v_{rms,c}$ was not available in Antonia and Bilger (1973) so isotropy is assumed ($u_{rms} \approx v_{rms}$) and their results are normalized by the centerline variance of the longitudinal velocity ($u^2_{rms,c}$). The results are in good agreement. The positive values reached by the curves from Antonia and Bilger (1973) and Smith and Hughes (1977) are slightly larger than their negative values. A small asymmetry was also noticeable in the present work but it was corrected, as will be discussed later.

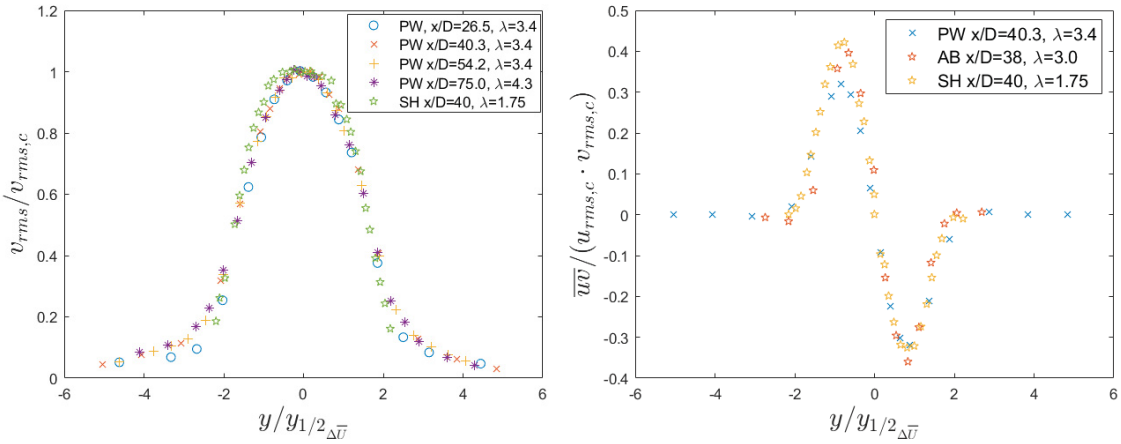

(a) (b)

Figure 4–4: Radial profiles of (a) $v_{rms}/v_{rms,c}$, and (b) $\overline{uv}/(u_{rms,c} \cdot v_{rms,c})$ for turbulent jets issued into nominally laminar coflows.

Figure 4–5 depicts the mean temperature excess ($\Delta\overline{T} = \overline{T} - T_\infty$), normalized by its value at the centerline ($\Delta\overline{T}_c = \overline{T}_c - T_\infty$), plotted as a function of the radial position (y), normalized by the half-width of the mean temperature excess profile

($y_{1/2_{\Delta\overline{T}}}$). The present data are compared with fits to the mean concentration (C) measurements of Chu et al. (1999) and Davidson and Wang (2002) for various x/D and λ. Similar to the velocity, the data collapse onto a single curve, which confirms the self-similarity of the mean temperature excess profiles at the downstream positions studied. Moreover, the present data are in good agreement with the two other works.

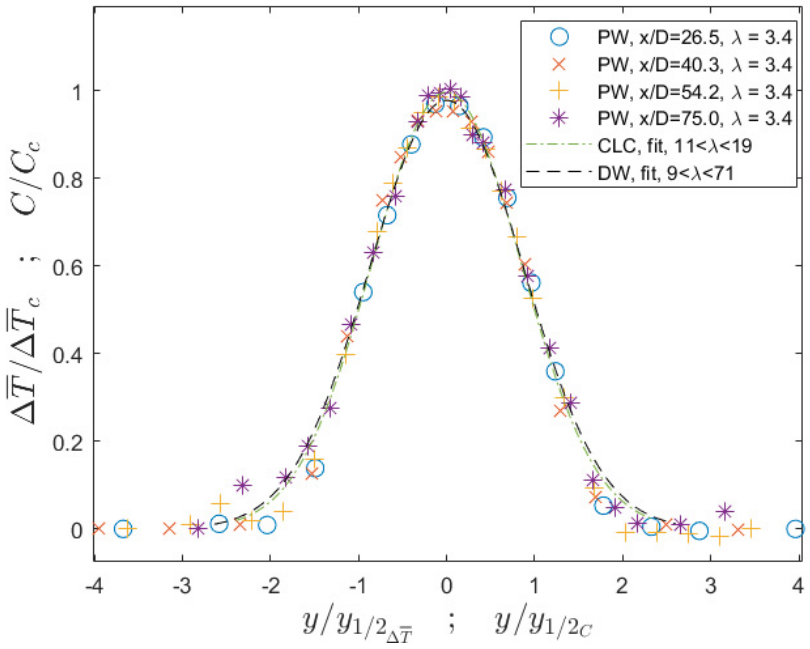

Figure 4–5: Radial profiles of the mean temperature excess for turbulent jets issued into nominally laminar coflows.

Chu et al. (1999) and Davidson and Wang (2002) studied the evolution of $\frac{C_c}{C_j}(\lambda - 1)$, where C_j and C_c are respectively the mean concentration at the jet exit and at the jet centerline, with the downstream distance (x) normalized by the momentum length of the flow, $l_m = \frac{\sqrt{Me_0}}{U_\infty}$, where Me_0 is the initial excess momentum of the jet. It was not possible to properly extract the data points from the figures of these works

but Chu et al. (1999) measured the normalized centerline mean concentration in the strong jet region (i.e. $x/l_m \leq 15$) and found that it decays as $(x/l_m)^{-1}$. Davidson and Wang (2002) extended their measurements to higher values of x/l_m. Their data were in agreement with an $(x/l_m)^{-1}$ decay in the strong jet region, and they showed that the normalized centerline mean concentration decays as $(x/l_m)^{-2/3}$ in the weak jet region.

Chu et al. (1999) and Davidson and Wang (2002) also studied the evolution of the half-width of the mean concentration profile ($y_{1/2_C}$), normalized by l_m, with the normalized downstream distance (x/l_m). Again, they measured $y_{1/2_C}$ in the strong jet region and Davidson and Wang (2002) extended the measurements to the weak jet region. They showed that $y_{1/2_C}$ grows as $(x/l_m)^1$ in the strong jet region and as $(x/l_m)^{1/3}$ in the weak jet region.

In the present work, data were taken in an intermediate range of the values of x/l_m, between the strong and weak jet regions. The power law exponents obtained for the respective decay and growth of the centerline values and the half-width of the mean temperature excess are summarized in table 4–5. The exponents are similar to the values obtained for the velocity field. $\Delta\overline{T}_c/\Delta T_j$ is found to approximately decay as x^{-1} and $y_{1/2_{\Delta\overline{T}}}/l_m$ approximately grows as $x^{0.7}$. These values are in agreement with the results of Chu et al. (1999) and Davidson and Wang (2002) and are closer to the values found in the strong jet region ($n_1 = -1$ and $n_2 = 1$) than the ones found in the weak jet region ($n_1 = -2/3$ and $n_2 = 1/3$).

Table 4–5: Power law decay/growth exponents (n_1 and n_2) for $\Delta\overline{T}_c/\Delta T_j$ and $y_{1/2_{\Delta\overline{T}}}/l_m$ for turbulent jets issued into nominally laminar coflows

	PW	
	$\lambda = 3.4$	$\lambda = 4.3$
$\frac{\Delta\overline{T}_c}{\Delta T_j}(\lambda - 1) = A_1(\frac{x}{l_m})^{n_1}$	-1.08	-1.04
$\frac{y_{1/2_{\Delta\overline{U}}}}{l_m} = A_2(\frac{x}{l_m})^{n_2}$	0.77	0.69

Lastly, note that radial profiles of the r.m.s. concentration were not reported in Chu et al. (1999) nor Davidson and Wang (2002).

4.2 Results

The results pertaining to this thesis are presented and discussed in the following subsections, which cover the mean velocity and temperature fields, the r.m.s. velocity and temperature fields, the combined velocity-temperature statistics as well as the velocity and temperature spectra, PDFs, and conditional expectations.

4.2.1 Mean velocity and temperature fields

Figures 4–6 and 4–7 plot typical radial profiles of the mean axial velocity and temperature excesses, normalized by their respective value at the jet exit. (Plotting all the results for the 48 cases studied herein would be excessive and counterproductive.) To be consistent with standard scaling used for jets emitted into quiescent backgrounds, they are plotted as function of the radial position (y), normalized by the downstream distance (x). The radial profiles are presented for different downstream distances, for the three levels of background turbulence, and for $\lambda = 3.4$. This

value of λ is chosen because it corresponds to the slowest jet in the fastest coflow (i.e. the smallest λ), and therefore represents the velocity ratio at which the jet should be the most impacted by the coflow (to be discussed shortly). It can be observed that the profiles for $T_i = 0.4\%$ and 2.2% are very similar to each other in the majority of the figures, which indicates that the effect of the turbulent background on *mean* profiles may not be observed until T_i increases to larger values. Nevertheless, at $x/D = 75.0$ (the farthest downstream distance in this work), a distinct decrease can be observed in the temperature profiles when comparing the $T_i = 2.2\%$ to the $T_i = 0.4\%$ cases. This was also observed in the analogous figures for the three other values of λ (not shown). In some figures, the profiles for $T_i = 2.2\%$ have the same width but reach slightly higher values than the ones for $T_i = 0.4\%$. This is attributed to experimental error − particularly to the uncertainty in the measurement of the velocity and temperature at the jet exit (U_j and T_j), which is further discussed in Appendix B. When the background turbulence intensity increases to 9.8%, both the centerline velocity and temperature excesses are substantially reduced and the profiles significantly broaden. For the $\lambda = 3.4$ case depicted in figures 4–6 and 4–7, $\Delta\overline{U}$ and $\Delta\overline{T}$ are close to zero at $x/D = 75.0$ when $T_i = 9.8\%$, which suggests that the jet's structure is almost completely destroyed on average by the effect of the background turbulence in this limiting case.

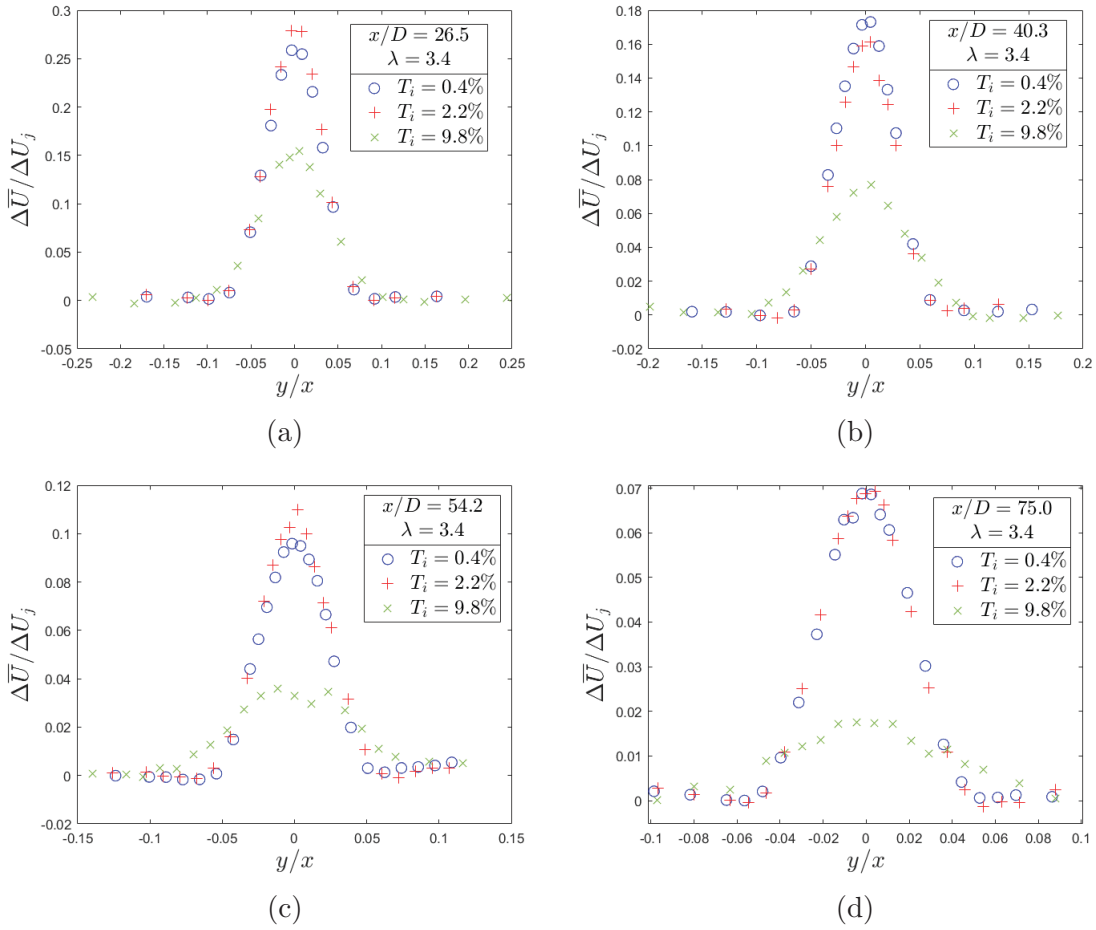

Figure 4–6: Radial profiles of $\Delta\overline{U}/\Delta U_j$ for $\lambda = 3.4$ and the three values of T_i, at (a) $x/D = 26.5$, (b) 40.3, (c) 54.2, and (d) 75.0.

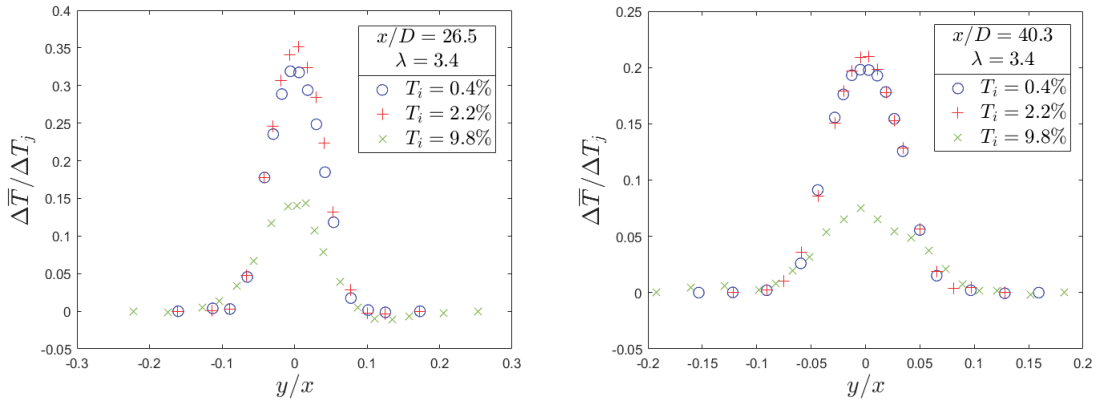

(a) $x/D = 26.5$

(b) $x/D = 40.3$

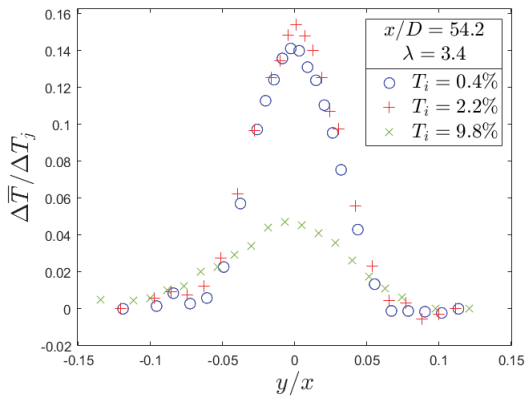

(c) $x/D = 54.2$

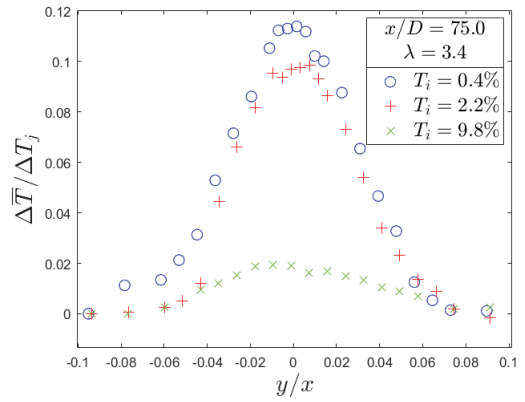

(d) $x/D = 75.0$

Figure 4–7: Radial profiles of $\Delta\overline{T}/\Delta T_j$ for $\lambda = 3.4$ and the three values of T_i, at (a) $x/D = 26.5$, (b) 40.3, (c) 54.2, and (d) 75.0.

To examine the effect of the ratio of jet-to-background velocity (λ) on the jet's development, figure 4–8 compares the radial profiles of the normalized mean axial velocity and mean temperature excesses for each value of λ, at $x/D = 40.3$. For clarity, only the profiles for the lowest and the highest background turbulence intensities are shown, given that the results for the $T_i = 2.2\%$ case are very similar to those for $T_i = 0.4\%$. When the mean velocity and temperature excesses are normalized by their respective value at the jet exit, the results are similar for the two intermediate

values of λ (4.3 and 4.6), as expected due to the small difference between these two values. However, the relevance of λ will be further discussed in subsequent sections. It can be observed that at fixed jet velocities (U_j constant), the mean velocity and temperature excesses are smaller when the background velocity is larger (i.e. $\lambda = 3.4$ and 4.3), which suggests that a faster coflow accelerates the decay of the jet. Similarly, for cases with constant background velocity (U_∞), the jet decays faster when the initial jet's velocity is smaller (i.e. $\lambda = 3.4$ and 4.6). Since less momentum is initially injected (relative to the background flow), the jet is "weaker", and therefore more "affected" by the coflow. Moreover, these effects are more significant when the background turbulence intensity increases. That is why the jet at lower λ (3.4) and higher T_i (9.8%) has the lower mean velocity and temperature values.

Figure 4–9 plots the decay of the centerline mean axial velocity and temperature excesses, normalized by their respective value at the jet's exit, for the three different levels of background turbulence intensity and the four values of λ. Consistent with the radial profiles, there are only small differences in the evolution of these quantities for the $T_i = 0.4\%$ and $T_i = 2.2\%$ cases. However, when $T_i = 9.8\%$, the values of both fields are significantly smaller, and the difference increases with the downstream position. From figure 4–9, it can be observed that the decay of $\Delta\overline{U}_c/\Delta U_j$ and $\Delta\overline{T}_c/\Delta T_j$ approximately follows a power law. The data were therefore similarly fit by least-squares to a power law curve fit ($\Delta\overline{U}_c/\Delta U_j = A_1(x/D)^{n_1}$ and $\Delta\overline{T}_c/\Delta T_j = A_2(x/D)^{n_2}$) and the corresponding decay exponents (n_1 and n_2) are summarized in table 4–6. It can be observed that the centerline mean velocity decays faster than the centerline mean temperature for all values of λ and T_i. Thus the velocity field

seems to be more impacted by the coflow than the scalar field. Moreover, the decay rate is increased for both fields when the background turbulence intensity increases.

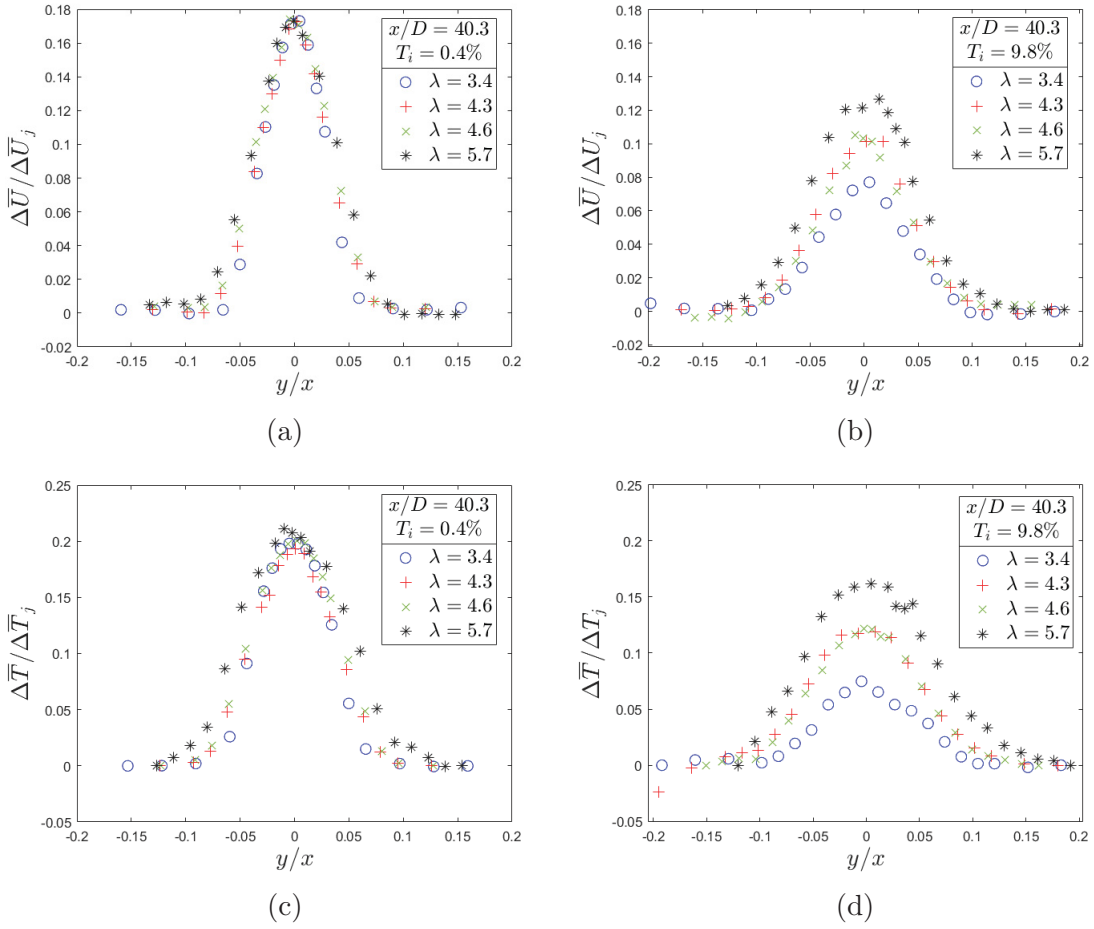

Figure 4–8: Radial profiles of $\Delta\overline{U}/\Delta U_j$ and $\Delta\overline{T}/\Delta T_j$ at $x/D = 40.3$ for the different λ, when $T_i = 0.4\%$ and $T_i = 9.8\%$.

Table 4–6: Decay exponents (n_1 and n_2) for $\Delta\overline{U}_c/\Delta U_j$ and $\Delta\overline{T}_c/\Delta T_j$

	$\lambda = 3.4$		$\lambda = 4.3$		$\lambda = 4.6$		$\lambda = 5.7$	
$T_i(\%)$	$\Delta\overline{U}_c$	$\Delta\overline{T}_c$	$\Delta\overline{U}_c$	$\Delta\overline{T}_c$	$\Delta\overline{U}_c$	$\Delta\overline{T}_c$	$\Delta\overline{U}_c$	$\Delta\overline{T}_c$
0.4	-1.26	-1.09	-1.05	-1.05	-1.30	-0.98	-1.20	-0.90
2.2	-1.36	-1.28	-1.26	-1.10	-1.32	-1.00	-1.22	-1.06
9.8	-1.92	-1.70	-1.61	-1.34	-1.73	-1.55	-1.68	-1.40

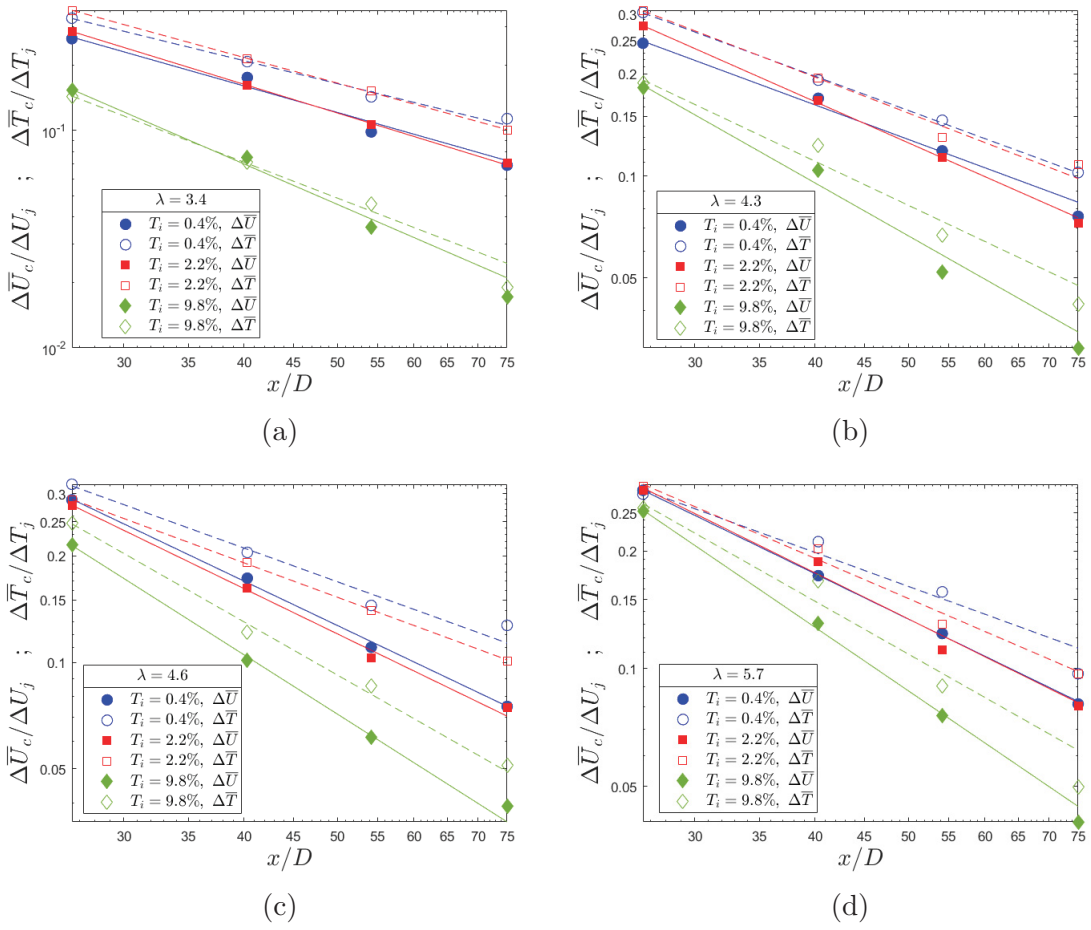

Figure 4–9: Downstream decay of the normalized centerline mean axial velocities and temperatures for different λ and T_i.

To quantify the radial spread of the jet, the downstream evolution of the half-widths of the mean velocity ($y_{1/2_{\Delta\overline{U}}}$) and temperature ($y_{1/2_{\Delta\overline{T}}}$) excesses are compared in figure 4–10 for the three background turbulence intensities and the four values of λ. For all T_i and λ, the half-widths increase with the downstream distance and were similarly fit by least-squares to a power law curve fit ($y_{1/2}/D = A(x/D)^n$). The values of the exponent are summarized in table 4–7.[2]

For both fields, there are, again, only small differences in the evolution of the half-widths when $T_i = 0.4\%$ and $T_i = 2.2\%$. However, the velocity and temperature half-widths are larger and grow faster for the highest background turbulence intensity, which is consistent with the radial spread observed in figures 4–6 and 4–7. It can be observed that the radial profiles of the temperature field are wider than the corresponding profiles of the velocity field. A similar result was observed by Perez-Alvarado (2016), who attributed it the increased radial transport of scalar due to the meandering of the jet, due to the background turbulence. Nevertheless, firm conclusions cannot be drawn regarding the difference in the growth exponents of the two fields i) given the small difference observed in certain cases, and ii) without additional measurements at larger λ. The data of table 4–7 indicate that the temperature half-width increases faster than the velocity half-width at the low turbulence

[2] It was found that excluding the temperature data at $x/D = 75.0$ for $T_i = 9.8\%$ from the power law curve fits significantly increased the quality of the curve fits (R^2 coefficient), except for $\lambda = 3.4$. This can be explained by the fact that, at the highest background turbulence intensity and the highest downstream position, the jet's structure is the most impacted and the temperature excess is small so there was significantly more uncertainty in the measurement of the half-widths.

intensities and for the smallest values of λ. However, it is not always the case when λ increases or when $T_i = 9.8\%$.

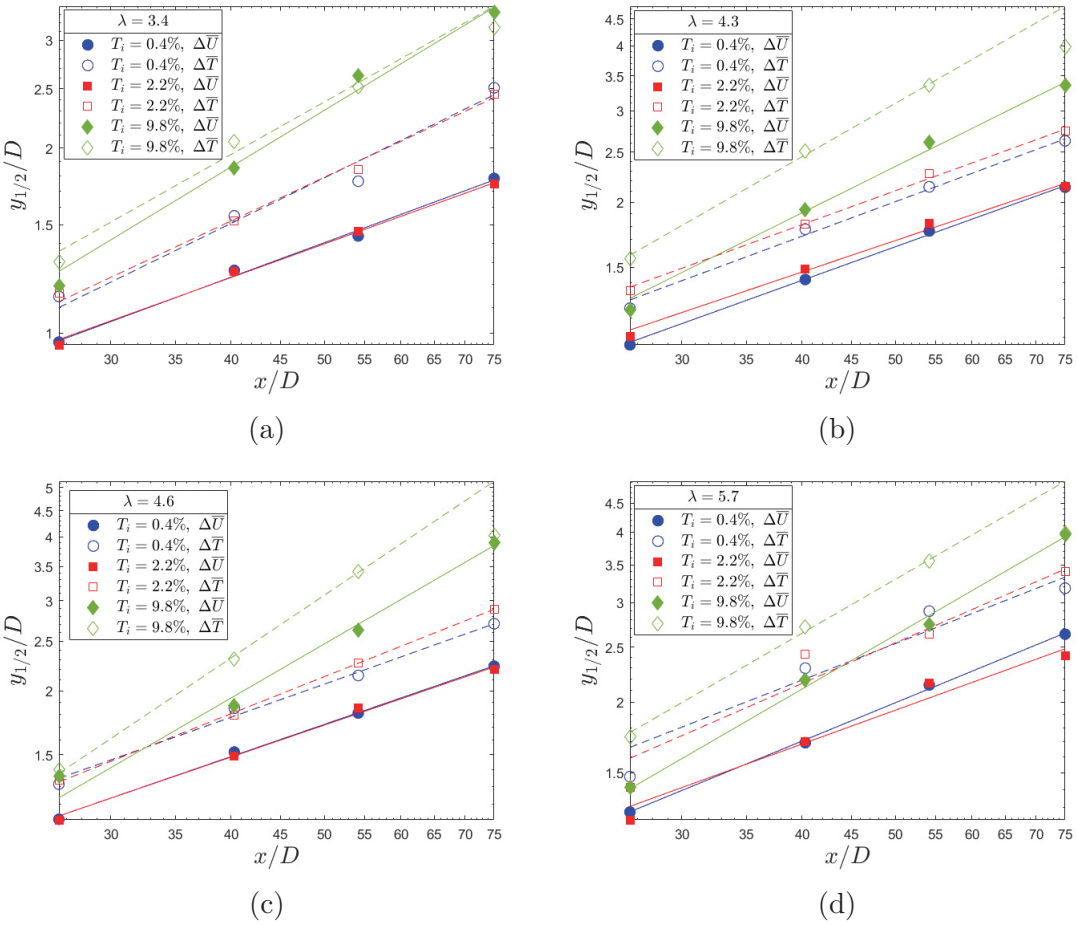

Figure 4–10: Half-widths of $\Delta\overline{U}$ and $\Delta\overline{T}$ for the different λ and T_i.

Table 4–7: Growth exponents (n_1 and n_2) of $y_{1/2_{\Delta\overline{U}}}$ and $y_{1/2_{\Delta\overline{T}}}$

λ	3.4		4.3		4.6		5.7	
$T_i(\%)$	$\Delta\overline{U}$	$\Delta\overline{T}$	$\Delta\overline{U}$	$\Delta\overline{T}$	$\Delta\overline{U}$	$\Delta\overline{T}$	$\Delta\overline{U}$	$\Delta\overline{T}$
0.4	0.58	0.77	0.67	0.69	0.65	0.67	0.70	0.67
2.2	0.57	0.74	0.62	0.67	0.65	0.75	0.62	0.74
9.8	0.95	0.88	0.92	1.06	1.09	1.27	0.99	0.99

4.2.2 R.m.s. velocity and scalar fields

The radial profiles of the r.m.s. axial velocity, radial velocity, and temperature, normalized by their respective centerline values, are shown in figures 4–11, 4–12 and 4–13 for $\lambda = 3.4$, at the four downstream positions.[3] For the two components of velocity, the r.m.s. values in the jet decrease with increasing downstream position (and asymptote towards their respective values in the coflow). The same behavior is observed for the r.m.s. temperature profiles, but it is not explicitly displayed in figure 4–13 due to the normalization by the centerline value. Indeed, an important difference between the velocity field and the temperature field is that the coflow is isothermal with no temperature fluctuations. θ_{rms} will therefore always tend to 0 as y tends to infinity, whereas the r.m.s. velocities will tend to their respective values in the background flow, such that, far enough downstream, the profiles of the r.m.s. velocities will become flat ($u_{rms} = u_{rms,c} = u_{rms,\infty}$). As expected, the radial

[3] Another possible way to plot these results, similar to the mean quantities, would have been to subtract the r.m.s. velocity and temperature of the coflow and to use excess r.m.s. values. However, major features of the evolution of the r.m.s. velocities and temperature were not clearly displayed when plotting the data in this manner.

profiles of the r.m.s. velocities and temperature also become wider when x/D and T_i increase.

It can also be noted that an off-axis double-peak is observed in some profiles of u_{rms} and θ_{rms}. The locations of the peaks correspond to the radii at which the gradients of the mean axial velocity and temperature profiles are maximum (Karnik and Tavoularis 1989). These are therefore the radial locations at which turbulent production ($\overline{u_i u_j}\overline{S}_{ij}$, where $\overline{S}_{ij}$ is the mean strain rate of the flow, or $\overline{u_i\theta}\dfrac{\partial\overline{T}}{\partial x_i}$) in the jet is the highest. This double-peak is also observed in jets emitted into quiescent backgrounds. In the present work, double peaks are observed for the lowest background turbulence intensities when $\lambda = 3.4$ (especially for the temperature field), but they disappear when $T_i = 9.8\%$, indicating a change in the structure of the jet. This change is presumably due to increased turbulent transport due to the high-turbulence-intensity background flow. Indeed, these peaks are an indicator of the balance between (i) the turbulent production of velocity and temperature fluctuations by the local mean velocity and temperature gradients, respectively, and (ii) the turbulent transport of these fluctuations by the eddies of the flow (Karnik and Tavoularis 1989). Moreover, the absence of peaks in the v_{rms} profiles may be attributed to a reduced degree of turbulent production due to the smaller magnitude of the $\overline{V}$ velocity in such nearly-parallel flows.

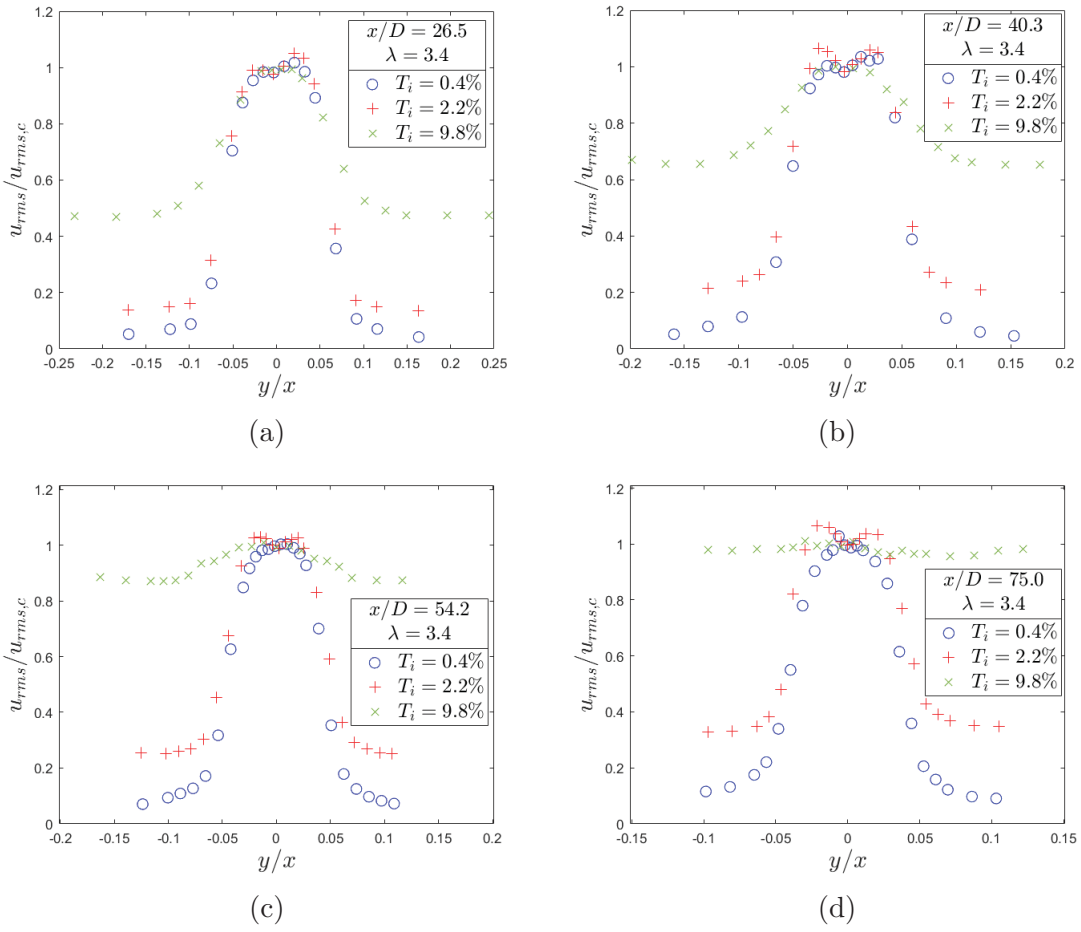

Figure 4–11: Radial profiles of the normalized r.m.s. axial velocity for $\lambda = 3.4$ at different x/D and T_i.

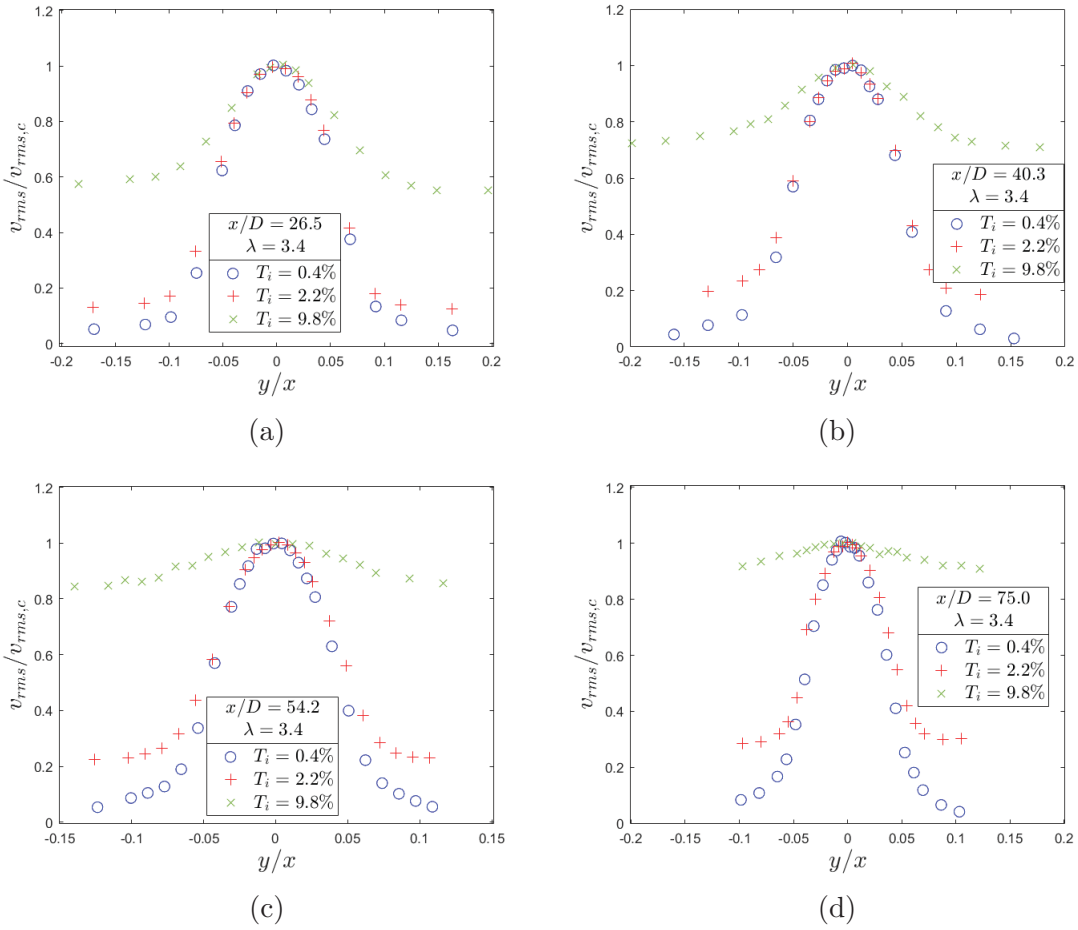

Figure 4–12: Radial profiles of the normalized r.m.s. radial velocity for $\lambda = 3.4$ at different x/D and T_i.

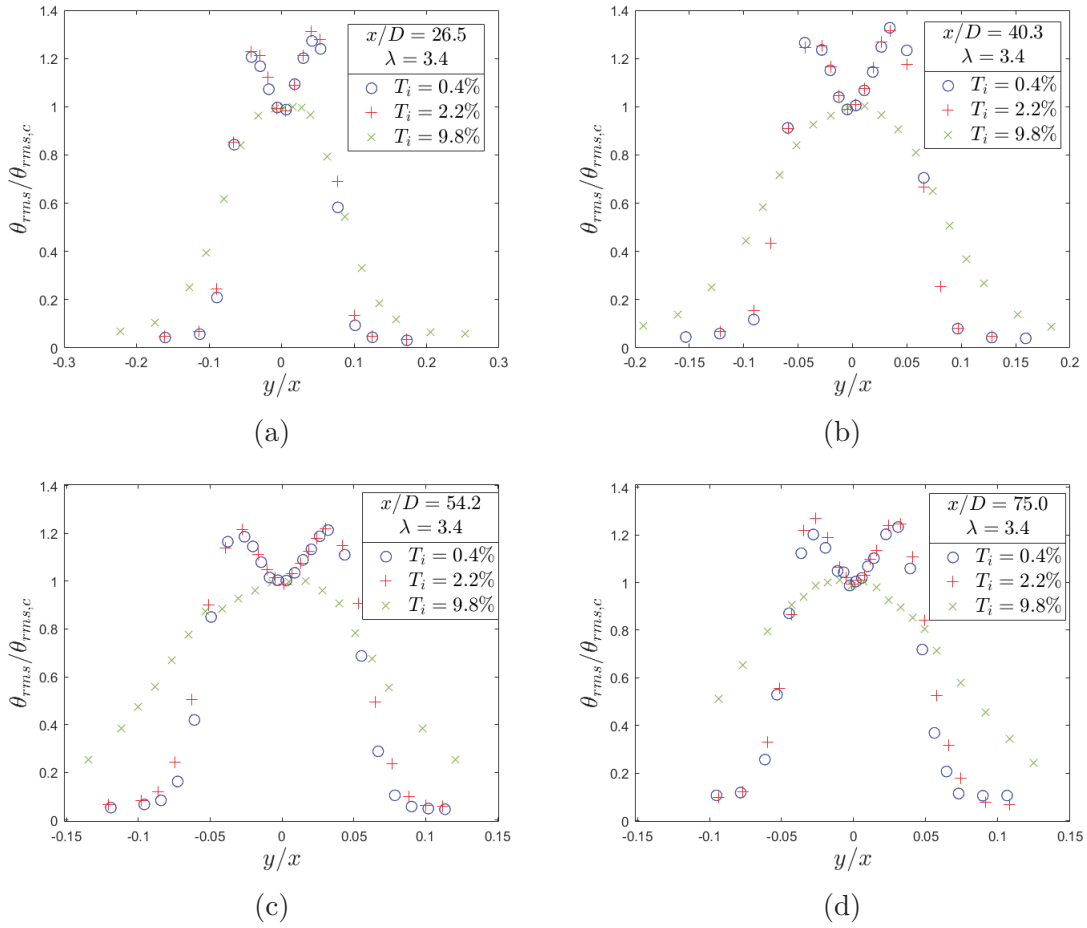

Figure 4–13: Radial profiles of the normalized r.m.s. temperature for $\lambda = 3.4$ at different x/D and T_i.

To study the effect of the jet-to-background velocity ratio, figure 4–14 compares the normalized profiles of u_{rms}, v_{rms} and θ_{rms} at a fixed downstream location ($x/D = 40.3$), for different values of λ, for $T_i = 0.4\%$ and $T_i = 9.8\%$. When the background turbulence intensity is low, the differences in the profiles for the different values of λ are relatively small. Their shape stays the same and the profiles are slightly larger as λ increases. However, when $T_i = 9.8\%$, an increase in the coflow velocity or a decrease in the jet's initial velocity (i.e. smaller λ) lead to flatter profiles

(similar to the mean quantities). It was observed in figures 4–11 and 4–13 that the off-axis double-peaks in the u_{rms} and θ_{rms} profiles had disappeared when $T_i = 9.8\%$, for $\lambda = 3.4$. However, figure 4–14 shows that these peaks are still present when $T_i = 9.8\%$, but only for the highest value of λ as they become single-peaked when λ decreases. Thus, the combined effects of λ and T_i are complex.

The downstream evolution of the centerline r.m.s. velocities and temperature is plotted in figure 4–15 for $\lambda = 4.6$ and the three values of T_i. To be able to compare these three quantities, the decay of the r.m.s. excesses ($\Delta u_{rms,c} = u_{rms,c} - u_{rms,\infty}$; $\Delta v_{rms,c} = v_{rms,c} - v_{rms,\infty}$; $\Delta\theta_{rms,c} = \theta_{rms,c}$), respectively normalized by the velocity and temperature excesses at the jet exit, are plotted. For the sake of brevity, only the figure for $\lambda = 4.6$ is displayed and table 4–8 summarizes the growth exponents (n_1, n_2, n_3) obtained for the four λ, three T_i and each parameter ($\Delta u_{rms,c}$, $\Delta v_{rms,c}$ and $\Delta\theta_{rms,c}$). It can be observed that the decay of the centerline axial and radial r.m.s. velocities excesses slightly increases when $T_i = 2.2\%$, compared to the $T_i = 0.4\%$ case, for all values of λ (except for $\Delta v_{rms,c}$ when $\lambda = 5.7$). Moreover, the decay of $\Delta u_{rms,c}$ and $\Delta v_{rms,c}$ is found to significantly increase when the background turbulence intensity increases to $T_i = 9.8\%$, as well as when λ decreases (weaker jet), especially at the highest background turbulence intensity. At $x/D = 75.0$, the values of the centerline r.m.s. velocities excesses drop when $T_i = 9.8\%$, which is consistent with the flat r.m.s profiles previously observed. However, the r.m.s. temperature seems to decay at approximately the same rate for all vaues of T_i, and this rate is similar to the one of the r.m.s. velocities for the two lowest background turbulence intensities. As previously discussed, this may be explained by the lack of temperature fluctuations in the coflow.

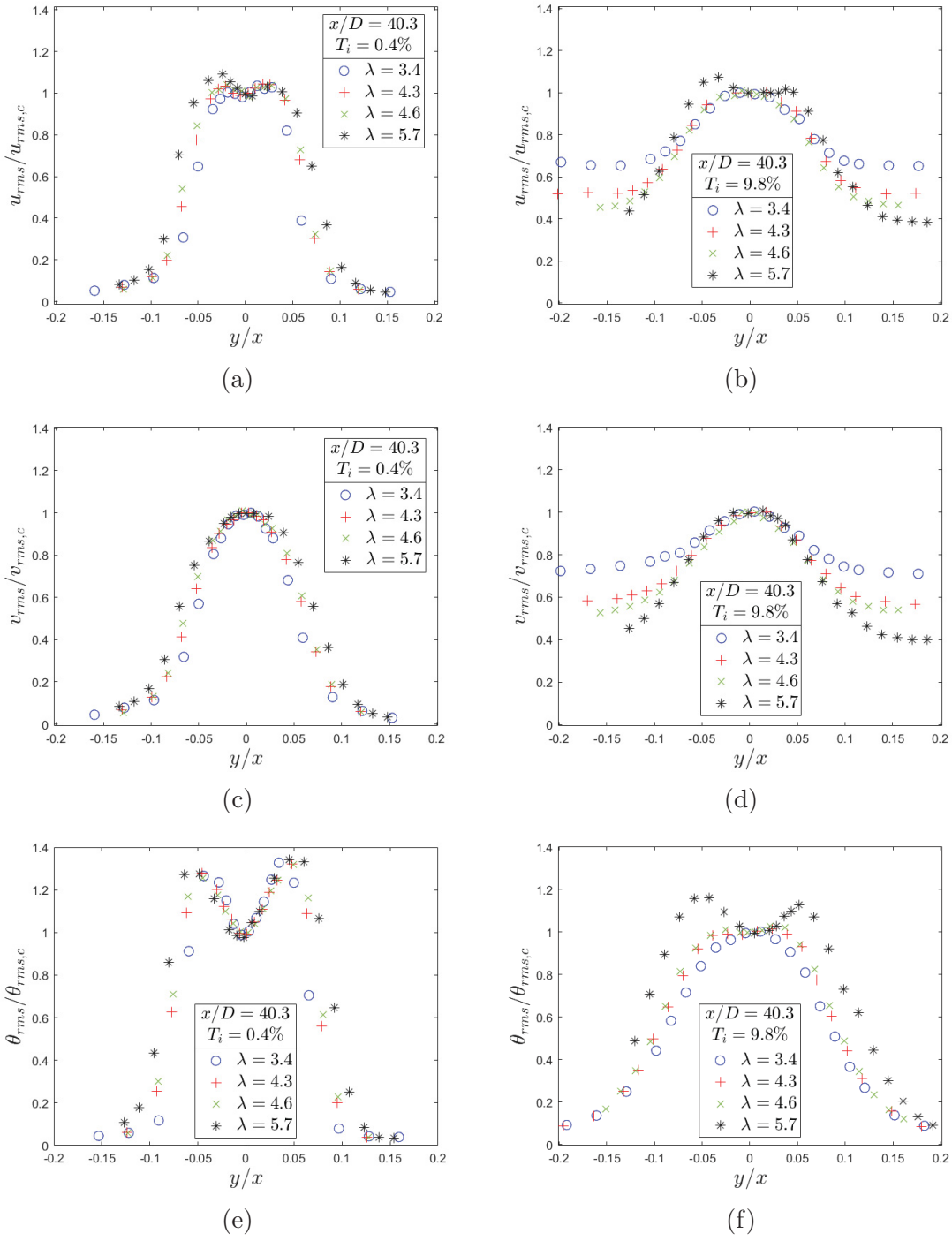

Figure 4–14: Radial profiles of the normalized r.m.s. quantities at $x/D = 40.3$ for different λ, when $T_i = 0.4\%$ and $T_i = 9.8\%$

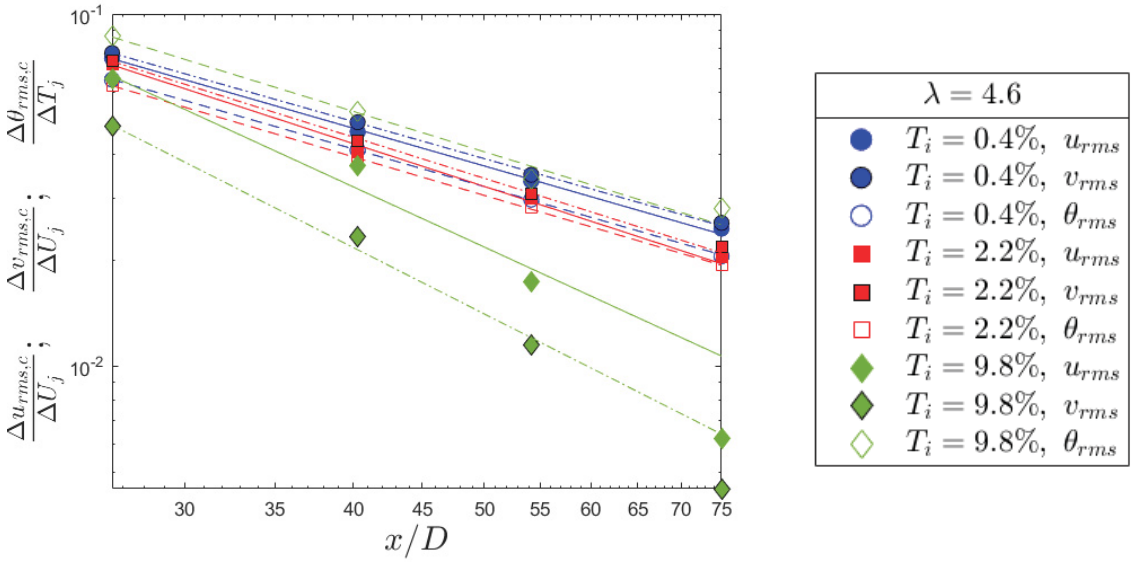

Figure 4–15: Downstream decay of the normalized centerline r.m.s. velocities and temperature for $\lambda = 4.6$ and the three values of T_i.

Table 4–8: Growth exponents (n_1, n_2, n_3) of $\frac{\Delta u_{rms,c}}{\Delta U_j}$, $\frac{\Delta v_{rms,c}}{\Delta U_j}$ and $\frac{\Delta \theta_{rms,c}}{\Delta T_j}$

λ	3.4			4.3		
$T_i(\%)$	$\Delta u_{rms,c}$	$\Delta v_{rms,c}$	$\Delta \theta_{rms,c}$	$\Delta u_{rms,c}$	$\Delta v_{rms,c}$	$\Delta \theta_{rms,c}$
0.4	-0.98	-0.90	-1.01	-0.90	-0.87	-0.89
2.2	-1.16	-1.22	-1.05	-1.22	-1.16	-0.95
9.8	-2.26	-2.05	-1.06	-1.65	-1.69	-0.84
λ	4.6			5.7		
$T_i(\%)$	$\Delta u_{rms,c}$	$\Delta v_{rms,c}$	$\Delta \theta_{rms,c}$	$\Delta u_{rms,c}$	$\Delta v_{rms,c}$	$\Delta \theta_{rms,c}$
0.4	-1.10	-1.09	-1.10	-0.95	-1.16	-0.54
2.2	-1.25	-1.20	-1.13	-1.05	-1.05	-0.63
9.8	-1.76	-1.94	-1.18	-1.31	-1.58	-0.79

4.2.3 Combined velocity-scalar statistics

One of the principal benefits of undertaking simultaneous measurements of both velocities and temperature in the jet is the ability to measure combined velocity-scalar statistics. These can be used to quantify the transport of the scalar (and momentum) by the velocity fluctuations and are therefore of primary importance to the understanding of mixing and entrainment in turbulent jets.

To this end, correlation coefficients, defined as:

$$\rho_{uv} = \frac{\overline{uv}}{u_{rms}v_{rms}} \quad ; \quad \rho_{u\theta} = \frac{\overline{u\theta}}{u_{rms}\theta_{rms}} \quad ; \quad \rho_{v\theta} = \frac{\overline{v\theta}}{v_{rms}\theta_{rms}} \tag{4.1}$$

have been measured and their radial profiles are respectively plotted in figures 4–16, 4–17 and 4–18 for the four downstream positions and three background turbulence intensities, with $\lambda = 3.4$.

Given the underlying symmetries of this experiment, the values of ρ_{uv} and $\rho_{v\theta}$ must be positive for $y < 0$ and negative for $y > 0$, as expected exhibiting odd symmetry in the y-direction. Indeed, when the external fluid is entrained into the jet, the radial velocity will have opposite directions on each side of the jet. The profiles of $\rho_{u\theta}$ must exhibit even symmetry in the y-direction, as also expected given the underlying symmetries of this flow. Any part of the $\rho_{u\theta}(y)$ profiles that exhibits odd symmetry, and any part of the $\rho_{uv}(y)$ or $\rho_{v\theta}(y)$ profiles that exhibits even symmetry must be error of some sort. In the present work, these symmetries were not perfect for all data sets, so the profiles were corrected by only keeping the respective even and odd parts of the correlation coefficients:

$$\rho_{u\theta_{corrected}} = \left[\rho_{u\theta_{measured}}(y) + \rho_{u\theta_{measured}}(-y)\right]/2 \tag{4.2}$$

$$\rho_{uv_{corrected}} = \left[\rho_{uv_{measured}}(y) - \rho_{uv_{measured}}(-y)\right]/2 \tag{4.3}$$

$$\rho_{v\theta_{corrected}} = \left[\rho_{v\theta_{measured}}(y) - \rho_{v\theta_{measured}}(-y)\right]/2 \tag{4.4}$$

From these figures, one observes that the radial profiles of each correlation coefficient are, again, similar for the $T_i = 0.4\%$ and $T_i = 2.2\%$ cases. For each correlation coefficient, the profiles become wider in the radial direction when the jet evolves downstream (not explicitly observable in the presented figures because of the chosen normalization of y by x). At a fixed x/D, this spread is more significant for the $T_i = 9.8\%$ case, compared to the $T_i = 0.4\%$ and 2.2% cases (especially for $\rho_{v\theta}$, as discussed in the next paragraphs).

The magnitude of ρ_{uv} is similar at every x/D when $T_i = 0.4\%$ and 2.2%. However, it is smaller and decreases with increasing x/D when $T_i = 9.8\%$, presumably because the strong background turbulence is more effective at mixing and uniformizing the jet.

For $\rho_{u\theta}$, the same behavior is observed but the maximum values reached when $T_i = 9.8\%$ are initially higher than the ones reached for $T_i = 0.4\%$ and 2.2% and they then decrease with increasing x/D to values below those measured at $T_i = 0.4\%$ and 2.2%. This demonstrates the important role played by the background turbulence in transporting of the scalar. Moreover, the initial strong transport of the scalar by the longitudinal velocity fluctuations ($\rho_{u\theta} \approx 0.7$) for the $T_i = 9.8\%$ case is so effective that it decays to smaller values much more rapidly (i.e. at smaller x/D) than the cases with lower background turbulent intensities. Moreover, the $\rho_{u\theta}(y)$

profiles exhibit off-axis double-peaks at every x/D for the lowest values of T_i, but the profiles flatten out as the jet evolves downstream for $T_i = 9.8\%$ (similar to the u_{rms} and θ_{rms} profiles).

The magnitude of $\rho_{v\theta}$ is slightly lower when $T_i = 9.8\%$ than when $T_i = 0.4\%$ and 2.2%. However, the most noticeable difference is the significantly increased width of the $\rho_{v\theta}$ profiles (in the transverse direction), which highlights the important role played by the strong background turbulence in diffusing the scalar across the flow.

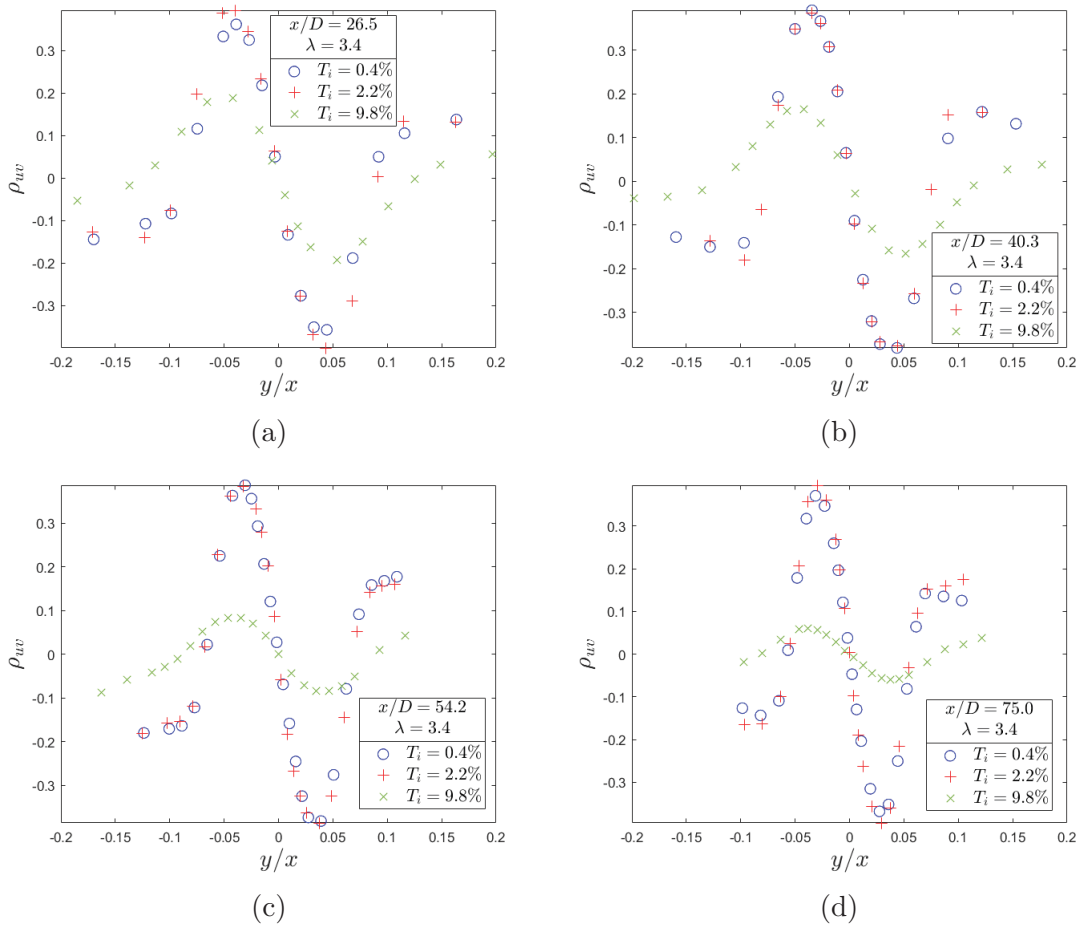

Figure 4–16: The correlation coefficient of u and v for $\lambda = 3.4$, at the four downstream distances, and for three background turbulence intensities.

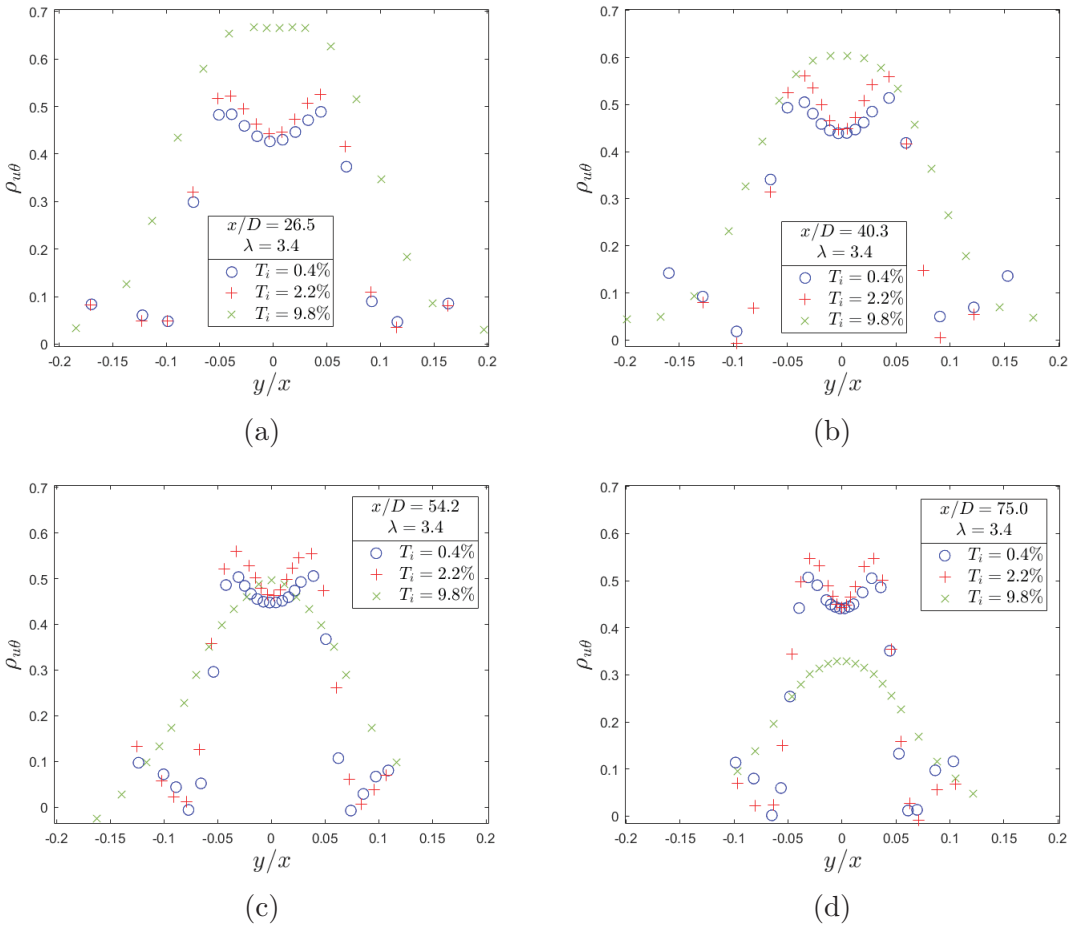

Figure 4–17: The correlation coefficient of u and θ for $\lambda = 3.4$, at the four downstream distances, and for three background turbulence intensities.

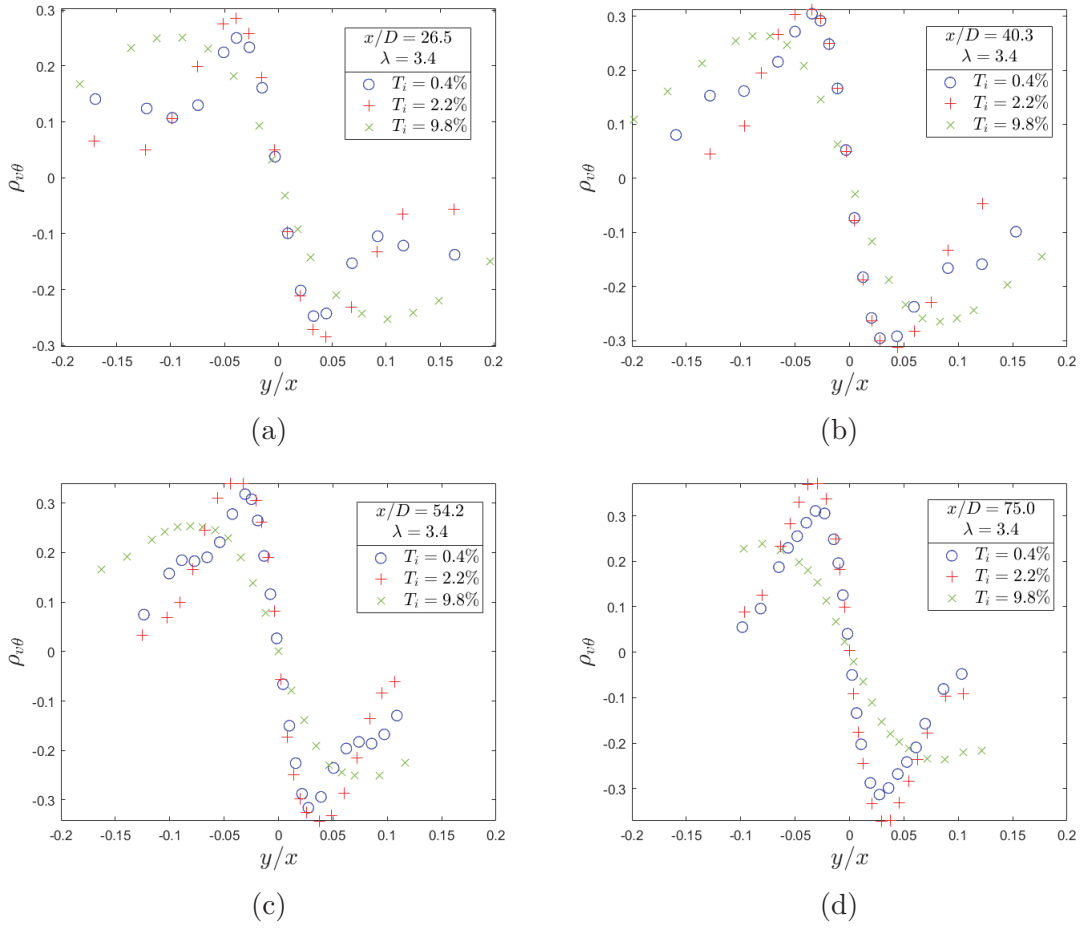

Figure 4–18: The correlation coefficient of v and θ for $\lambda = 3.4$, at the four downstream distances, and for three background turbulence intensities.

The variation of the profiles of the three correlation coefficients with λ is shown in figure 4–19 for $T_i = 0.4\%$ and $T_i = 9.8\%$. At the lowest background turbulence intensity, the correlation coefficients profiles are very similar for all λ, despite a slightly larger radial extent of $\rho_{u\theta}$ when λ increases.

When $T_i = 9.8\%$, it would appear that U_∞ may be a more significant parameter than λ, given that the pairs of profiles of ρ_{uv} and $\rho_{v\theta}$ for $\lambda = 3.4$ and 4.3, and for $\lambda = 4.6$ and 5.7 seem to be more similar than the profiles for $\lambda = 4.3$ and 4.6.

When the background turbulence is strong, the jet parameters may therefore be less significant. When $T_i = 9.8\%$, it can be observed that the widths of the radial profiles of the three correlation coefficients increase and the magnitudes of ρ_{uv} and $\rho_{v\theta}$ decrease with increasing values of U_∞, indicating that a faster coflow is also more effective at mixing and uniformizing the jet.

Moreover, similar to the u_{rms} and θ_{rms} profiles, the double peaks in $\rho_{u\theta}$ are present for all λ when $T_i = 0.4\%$ but, in the $T_i = 9.8\%$ case, they are only visible for $\lambda = 5.7$ and they disappear when λ decreases (U_∞ increases or U_{jet} decreases) as the jet is becomes more affected by the background turbulence.

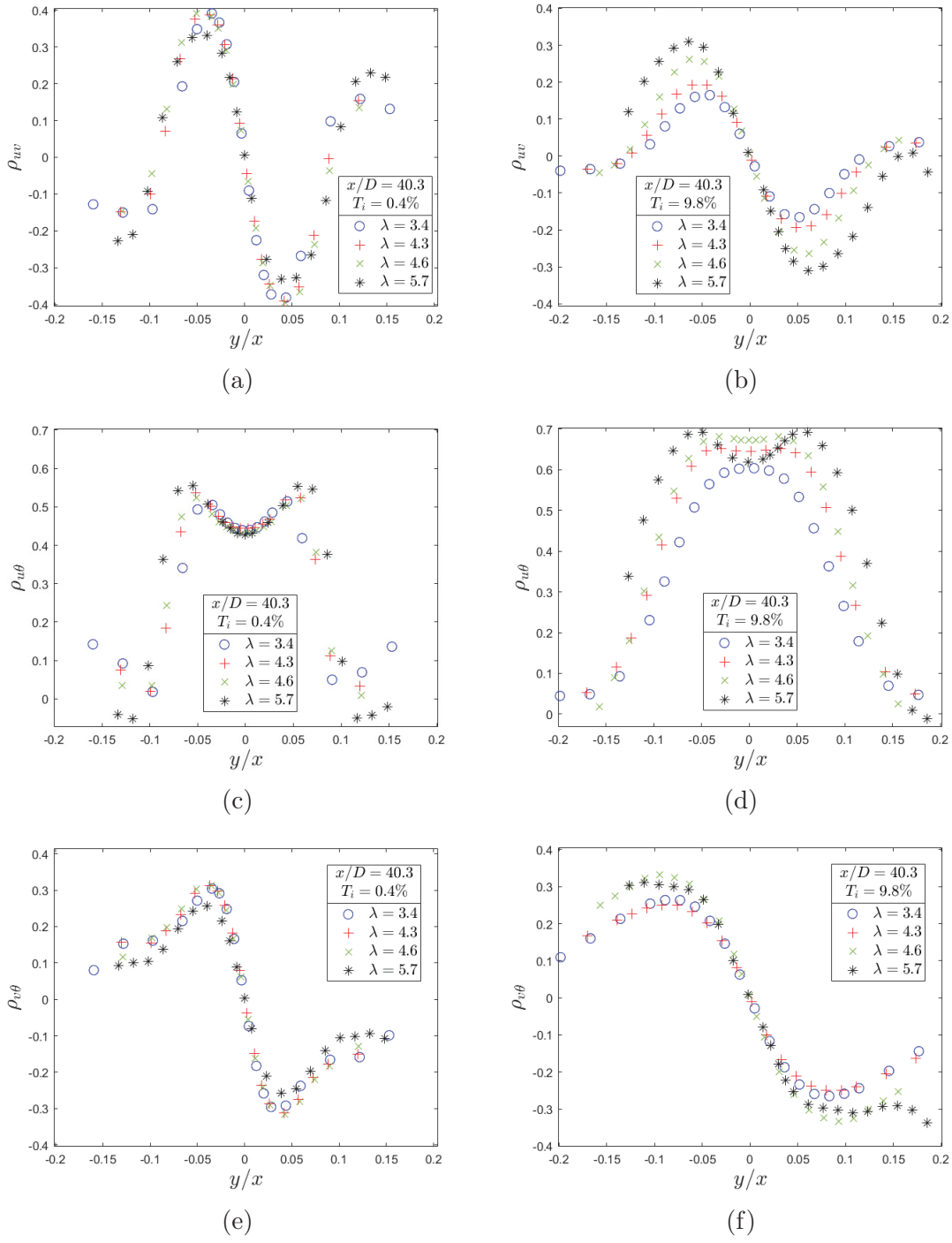

Figure 4–19: The correlation coefficients at $x/D = 40.3$ for the different values of λ, when $T_i = 0.4\%$ and $T_i = 9.8\%$.

4.2.4 Spectra

The 1-D spatial power spectral densities (referred to as spectra from hereon in) of the two velocity components and the temperature (F_{uu}, F_{vv} and $F_{\theta\theta}$) along the jet's centerline are plotted in figure 4–20 as a function of the longitudinal wavenumber, $\kappa_1 = \frac{2\pi}{\overline{U}} f$, normalized by the Kolmogorov length scale $\eta = \left(\frac{\nu^3}{\epsilon}\right)^{1/4}$. For each background turbulence intensity, the spectra are similar for all values of λ, so spectra with $\lambda = 3.4$ are only plotted and comparisons are made for the three background turbulence intensities at two downstream distances. Moreover, given the non-dimensionalization, the spectra are similar at the different downstream positions for each background turbulence intensity. In all the spectra, three distinct areas are visible: the energy containing range at large scales (small $\kappa\eta$), the inertial subrange (with the approximate -5/3 power law slope) and the dissipation range (when $\kappa\eta$ approaches 1). Differences in the spectra are most noticeable at low wavenumbers, in which the spectra reach higher values for $T_i = 9.8\%$, compared to the $T_i = 0.4\%$ case. The effect of background turbulence is therefore the most noticeable at large scales, where the large eddies have the most significant impact on the jet's structure. At intermediate and small scales, the spectra for $T_i = 9.8\%$ collapse with the ones for $T_i = 0.4\%$ and 2.2% (consistent with Kolmogorov theory), except for the temperature spectra at $x/D = 75$. Given the far downstream distance and the high background intensity for this case, the temperature excess is so small, this difference may be attributable to a reduced signal to noise ratio in the temperature measurements.

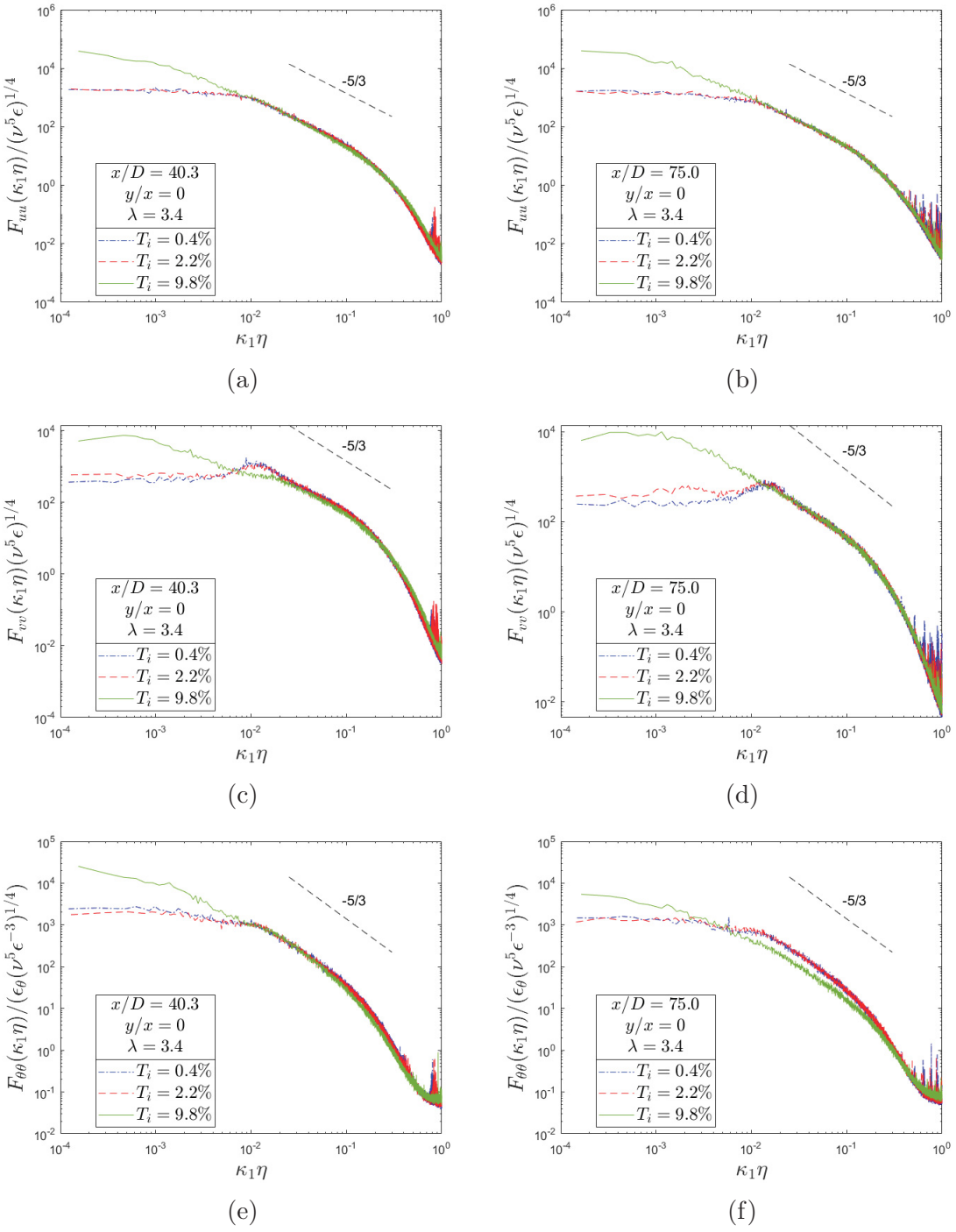

Figure 4–20: Spectra of the two velocity components and the temperature for the three values of T_i at two downstream positions, for $\lambda = 3.4$.

The correlation coefficients that were previously discussed provided information on the radial positions at which the velocities and the temperature were the most correlated. At a fixed location in the jet, coherence spectra are now used to measure the degree of correlation between the two fields in the spectral domain. For the velocity and temperature fields, three coherence spectra are defined:

$$C_{uv}(\kappa_1\eta) = \frac{|F_{uv}|^2}{F_{uu}F_{vv}} \quad ; \quad C_{u\theta}(\kappa_1\eta) = \frac{|F_{u\theta}|^2}{F_{uu}F_{\theta\theta}} \quad ; \quad C_{v\theta}(\kappa_1\eta) = \frac{|F_{v\theta}|^2}{F_{vv}F_{\theta\theta}} \tag{4.5}$$

where F_{uv}, $F_{u\theta}$ and $F_{v\theta}$ are the cross-spectra, which can be decomposed into their real (co-spectrum) and imaginary (quadrature spectrum) parts.

Given the even symmetry of both the longitudinal velocity and temperature fields, along with the odd symmetry of the transverse velocity field, C_{uv} and $C_{v\theta}$ are effectively equal to zero along the centerline for all values of $\kappa_1\eta$. Only the centerline spatial coherence spectra of the axial velocity and the temperature ($C_{u\theta}$) are therefore plotted in figure 4–21 for the four values of λ and two background turbulence intensities, at $x/D = 40.3$. For both background turbulence intensities, the values of $C_{u\theta}$ are also almost zero when $\kappa\eta > 0.1$ but they increase in the inertial subrange, when $\kappa\eta$ decreases (i.e. when the length scale increases). The noise observed in the coherence spectra at the smallest scales ($\kappa\eta \approx 1$) is not surprising, given that coherence spectra are the ratio of two spectra, and that the signal to noise ratio is its lowest at the smallest scales. At large scales, the values of $C_{u\theta}$ remain approximately constant for $T_i = 0.4\%$, whereas they exhibit a peak for the $T_i = 9.8\%$ case that appears to increase with increasing λ (i.e. as the jet becomes stronger relative to the coflow).

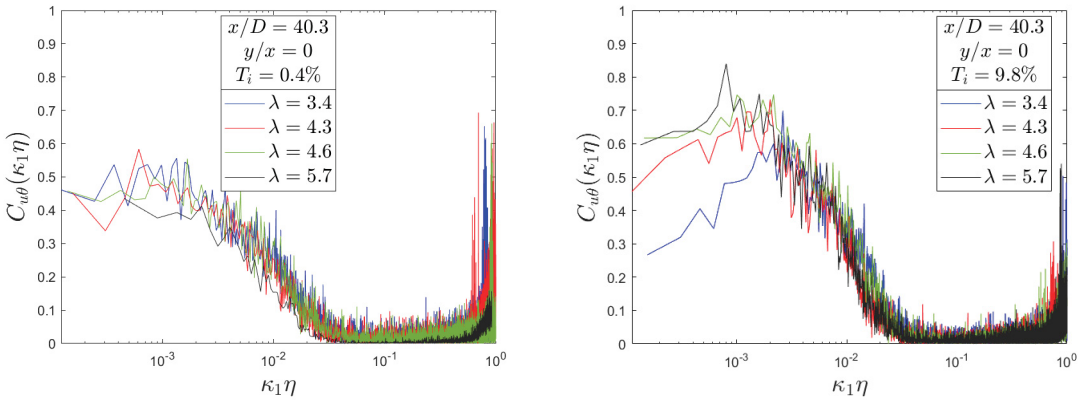

(a) (b)

Figure 4–21: Centerline coherence spectra of the longitudinal velocity and the temperature for the four values of λ and two background turbulence intensities, at $x/D = 40.3$.

Spectral data were not taken at the exact same (non-dimensionalized) radial locations in the jet for every level of background turbulence intensity and value of λ (given that the exact shape of the correlation coefficient profiles could not be determined *a priori* until the data were analyzed), which therefore prevents a detailed comparison of the coherence spectra. Nevertheless, figure 4–22 depicts some examples of measured coherence spectra at two radial positions: $y/x = -0.03$ (which lies between the centerline and half-width of the jet) and $y/x = -0.06$ (which lies between the half-width and the edge of the jet). At off-axis locations, C_{uv} and $C_{v\theta}$ will be non-zero. The study of $C_{v\theta}$ is particularly interesting as it provides information on the size of the scales that are responsible for entrainment.

When $T_i = 0.4\%$ (measured at $y/x = -0.03$), a single peak can be observed at intermediate scales, for $\kappa\eta \approx 10^{-2}$, in the three coherence spectra. When $T_i = 9.8\%$ (measured at $y/x = -0.06$), this peak is still noticeable, especially for C_{uv} and $C_{v\theta}$, but there is also a significant increase in the coherence at large scales (small values of

$\kappa\eta$). Even though the coherences were not plotted at the same y/x, these observations suggest that the intermediate scales are the main agent of entrainment for jets in laminar coflows, whereas entrainment in jets emitted into turbulent backgrounds is modified by the additional role of large scales of the ambient turbulence. Rephrased in terms of mechanisms, the observed coherence at intermediate scales arises from "nibbling" (Matthew and Basu 2002; Westerweel 2005, 2009), whereas the large-scale coherence is presumably due to turbulent transport by the largest eddies of the background turbulence.

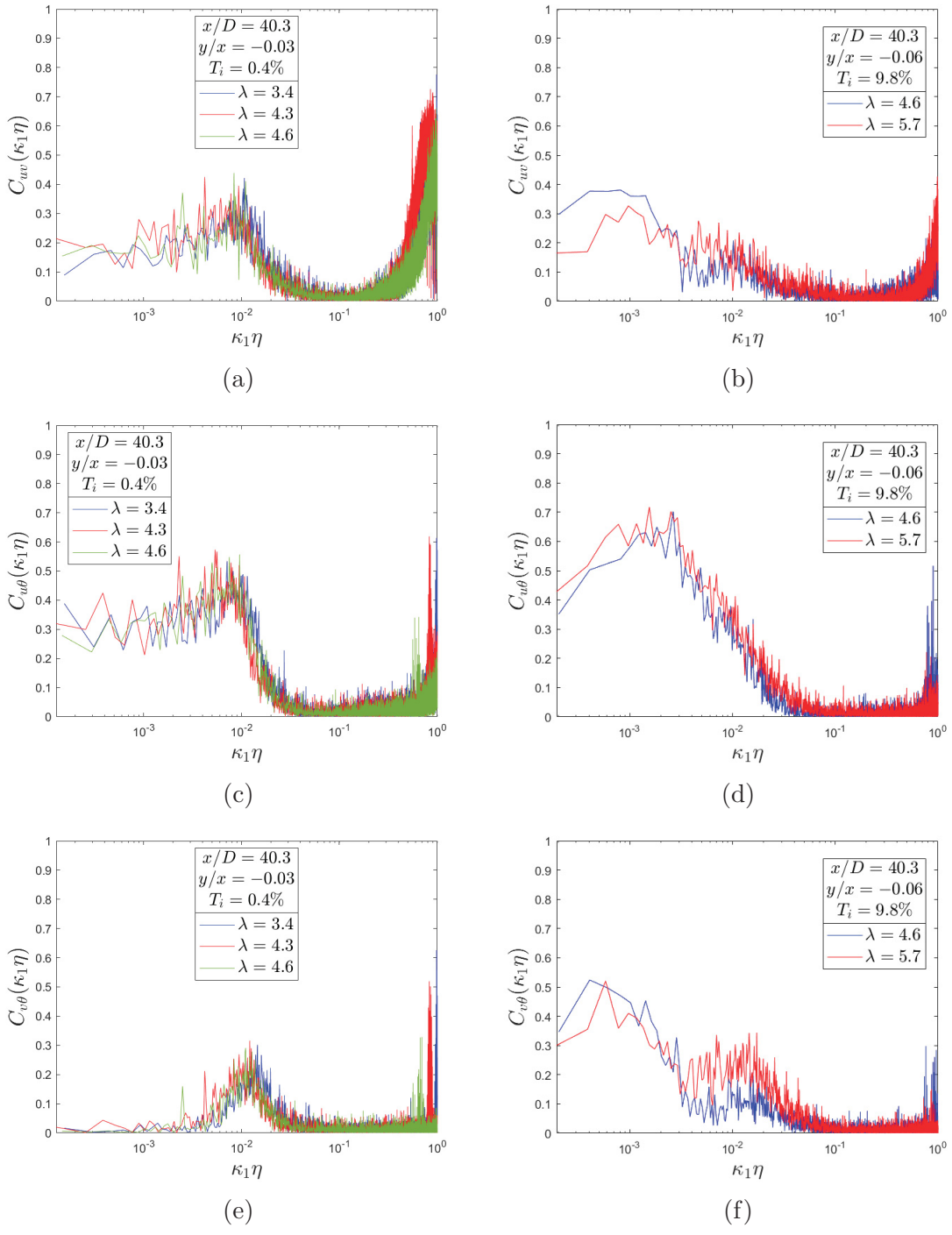

Figure 4–22: Coherence spectra for two background turbulence intensities and different values of λ, at $x/D = 40.3$ and two values of y/x.

4.2.5 PDFs

The probability density functions (PDFs) of the instantaneous velocities and temperature excesses are respectively shown in figures 4–23, 4–24 and 4–25 for the four values of λ and two background turbulence intensities, at $x/D = 40.3$. The PDFs are plotted at the three non-dimensional radial positions ($y/x = 0$, -0.03 and -0.06).

For $T_i = 0.4\%$, the PDFs of the normalized instantaneous axial velocity excess at $y/x = 0$ are unimodal and symmetric. As expected, the value at which they peak (the mode) is consistent with the mean centerline value at $x/D = 40$ ($\Delta\overline{U}/\Delta U_j(0) \approx 0.17$ for all λ, according to figure 4–8). When the radial position increases, the mean velocity excess in the jet decreases, so the mode of each PDF shifts towards zero, a smaller range of axial velocity values at that location is measured, and the height of the peak of each PDF therefore increases. For $T_i = 9.8\%$, a similar evolution is observed, but some differences can be noticed. At $y/x = 0$, the velocity values at which the PDFs peak are smaller for $T_i = 9.8\%$, compared to the $T_i = 0.4\%$ case, and they decrease with increasing λ, which is consistent with the mean values observed in figure 4–8. Moreover, the heights of the peaks are lower for $T_i = 9.8\%$, compared to the $T_i = 0.4\%$ case, because a larger range of velocities are measured, due to the increased mixing due to the turbulent background. The behavior is similar for the radial velocity, but the values found in the jet are smaller and the symmetry of the PDFs is better preserved at all radial positions.

The PDFs of the normalized instantaneous temperature excess have a different behavior. They evolve from having a peak around the mean value to having one at zero, and they are bimodal during the transition. This second peak around zero corresponds to cold fluid from the background flow that is entrained into the warm

jet. When the radial position increases, the probability of finding cold fluid from the background flow increases, while the probability of finding warmer fluid decreases. For $T_i = 0.4\%$, the PDFs of the temperature excess are unimodal at $y/x = 0$ and peak around the centerline mean value of $\Delta\overline{T}/\Delta T_j$. The second peak around zero is not noticeable at the jet's centerline and only starts to appear at $y/x = -0.03$. However for $T_i = 9.8\%$, the cold fluid is found deeper inside the jet as the second peak is already visible at the jet's centerline. This can be attributed to (i) an enhanced entrainment of the background flow into the jet, and (ii) the meandering in space of the jet around the stationary sensor. Moreover, the transition between the two peaks happens at smaller radial positions when λ decreases for both values of the background turbulence intensity, because the weaker jet is mixed more rapidly.

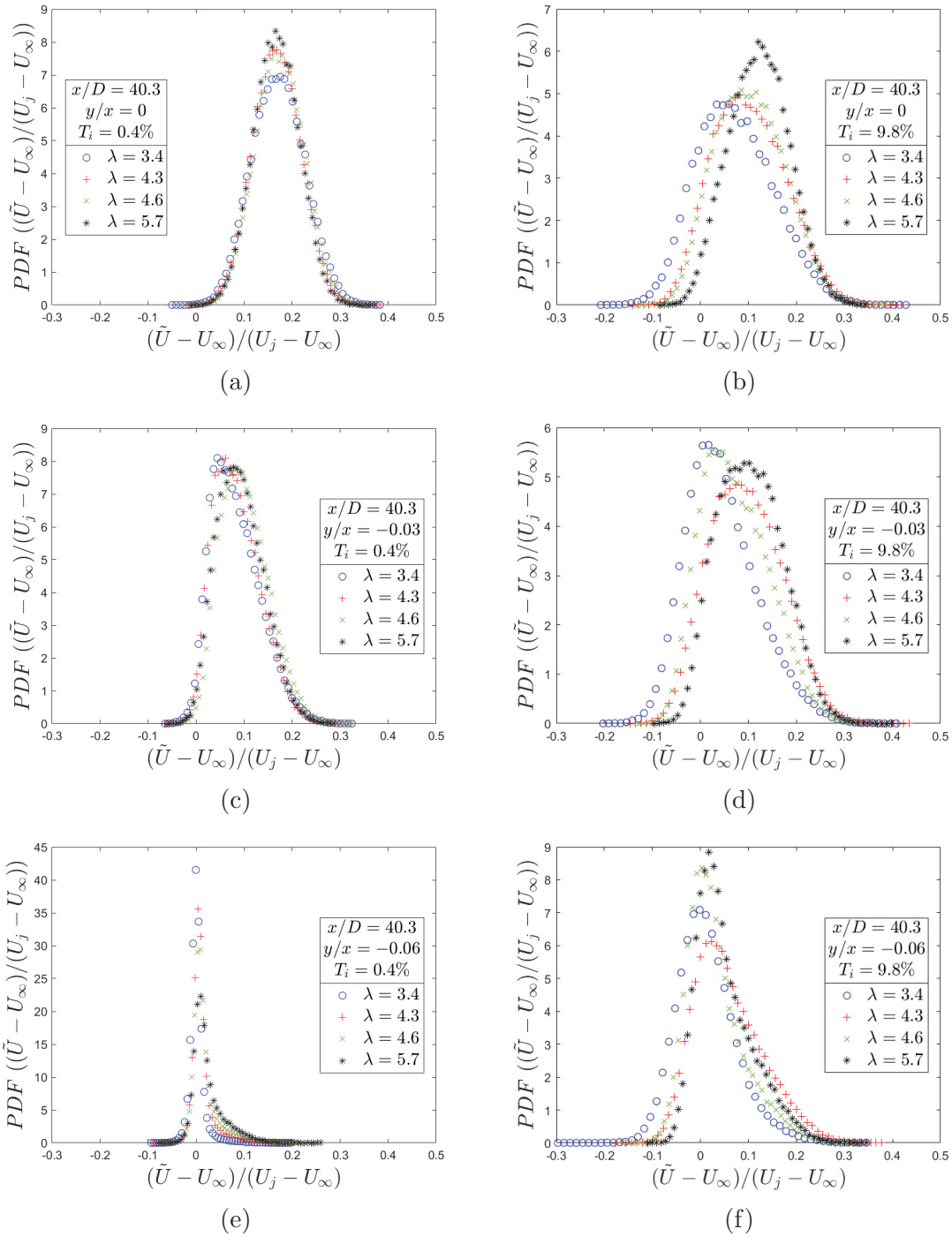

Figure 4–23: PDFs of the normalized instantaneous axial velocity excess for the four values of λ and two background turbulence intensities, at $x/D = 40.3$ and three radial positions.

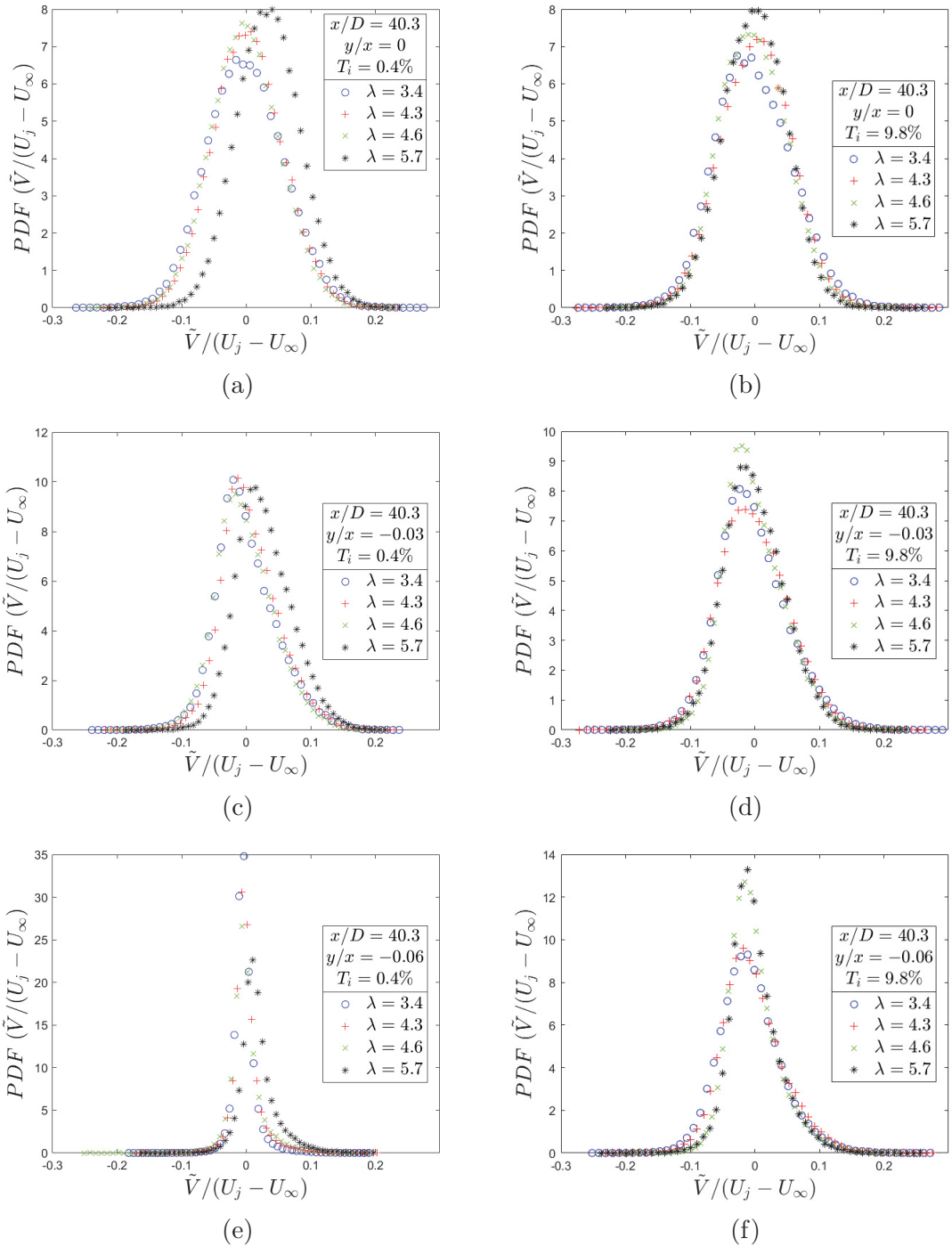

Figure 4–24: PDFs of the normalized instantaneous radial velocity for the four values of λ and two background turbulence intensities, at $x/D = 40.3$ and three radial positions.

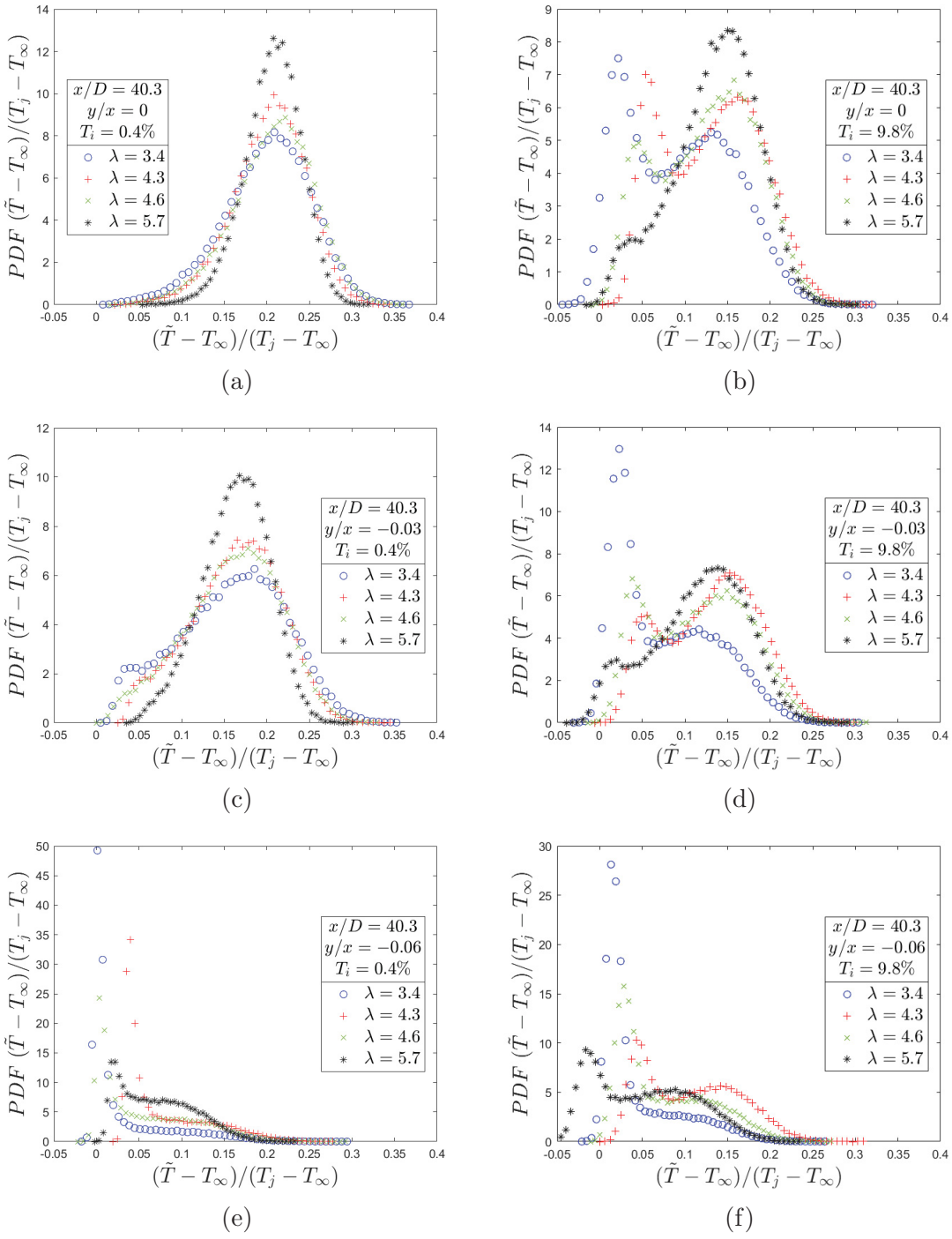

Figure 4–25: PDFs of the normalized instantaneous temperature excess for the four values of λ and two background turbulence intensities, at $x/D = 40.3$ and three radial positions.

The three possible joint-PDFs of the two components of velocity and the temperature at the three different radial positions are plotted in figures 4–26, 4–27 and 4–28 for $\lambda = 3.4$ and two background turbulence intensities, at $x/D = 40.3$. They are consistent with the PDFs discussed above, as must be the case; the width of the joint-PDFs of the two components of velocity decreases when T_i decreases and when $|y/x|$ increases. Their maximum values are higher for the $T_i = 0.4\%$ case, compared to $T_i = 9.8\%$, and they increase with the radial position. For the joint-PDFs of the temperature and each component of the velocity, the transition from unimodal to bimodal PDFs is visible when the radial distance increases. Moreover, this transition is faster for the highest background turbulence intensity. As previously discussed, the second peak is already visible at the jet centerline for $T_i = 9.8\%$, but not for $T_i = 0.4\%$.

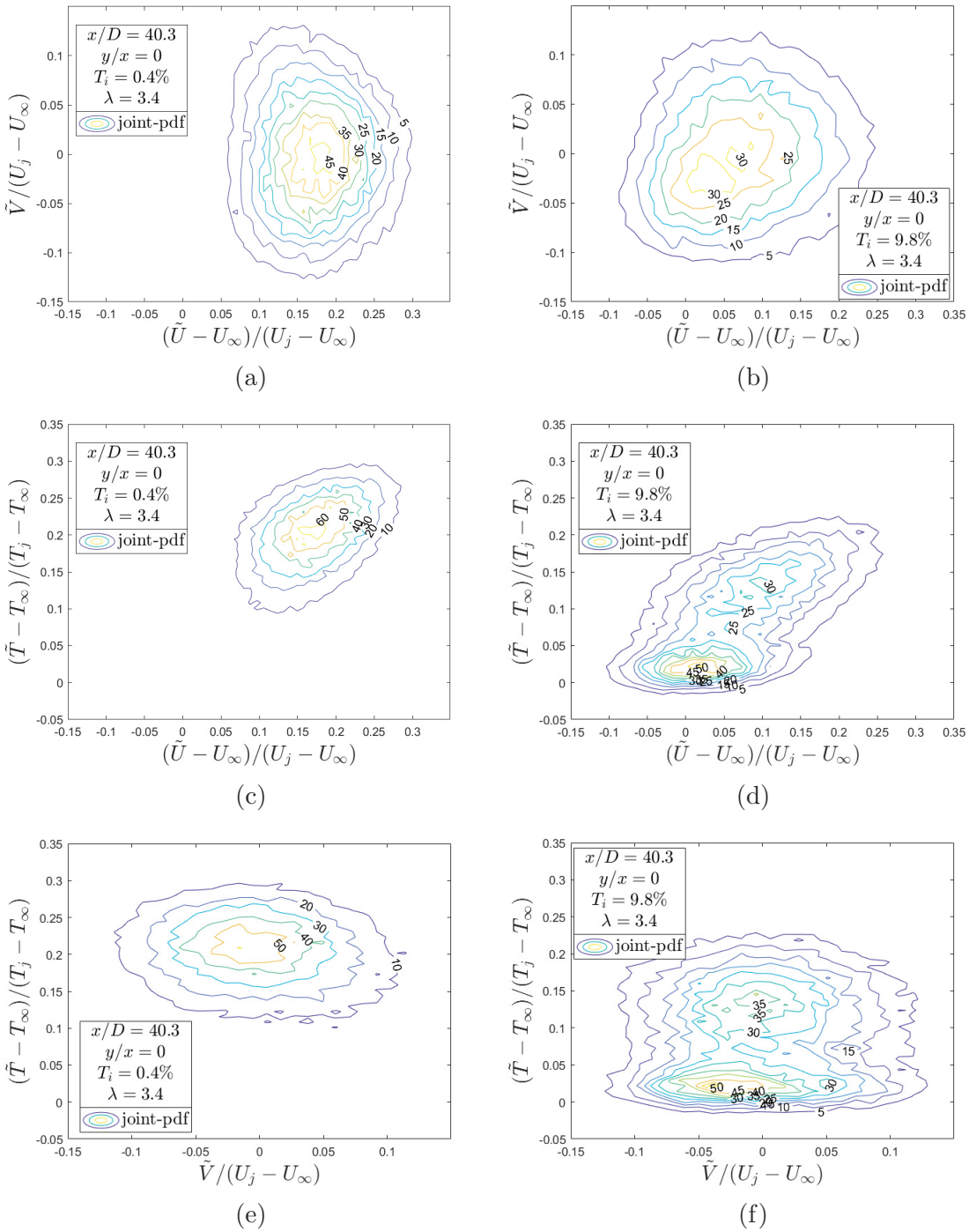

Figure 4–26: Joint-PDFs at $x/D = 40.3$ and $y/x = 0$, for $\lambda = 3.4$ and for $T_i = 0.4\%$ and $T_i = 9.8\%$.

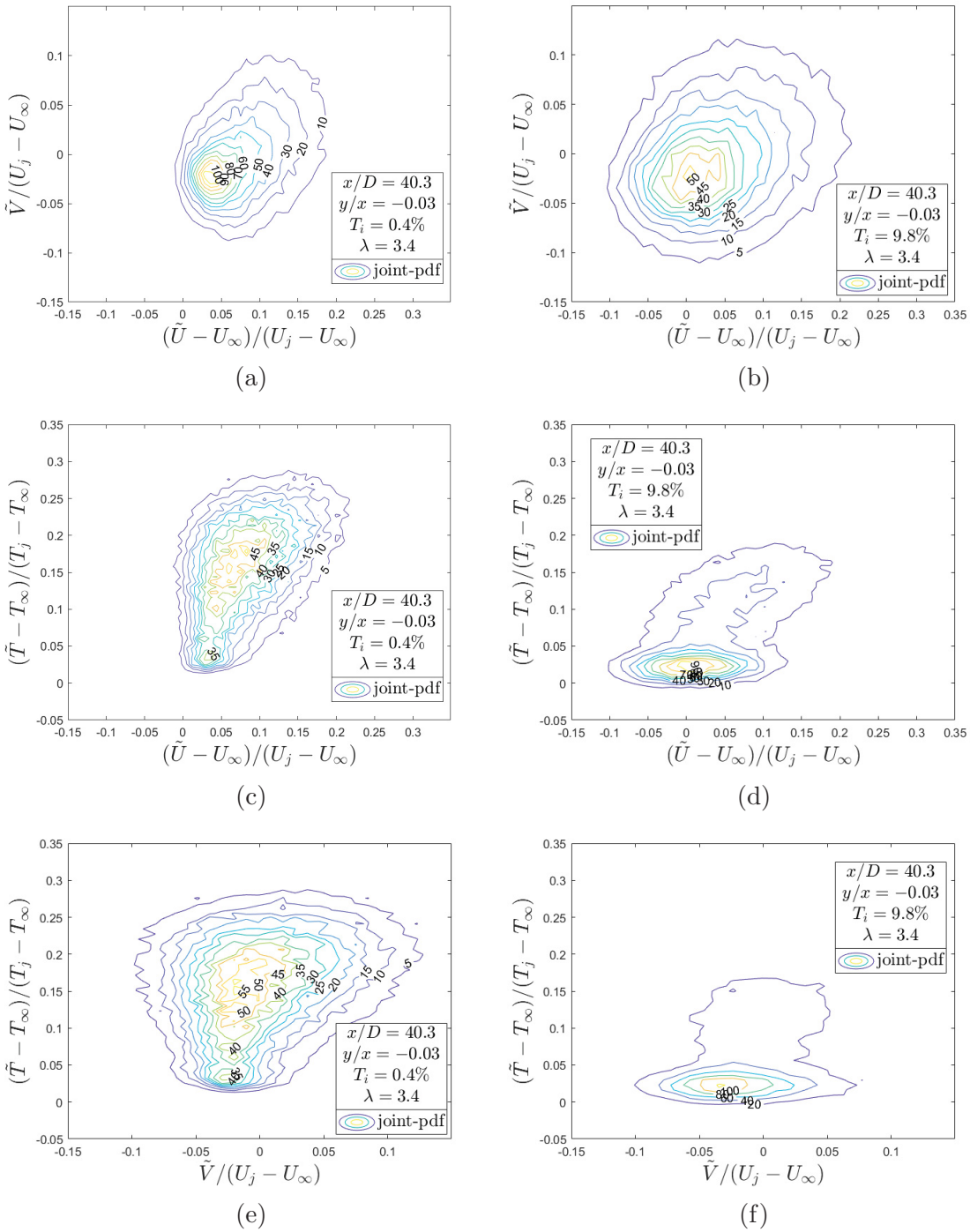

Figure 4–27: Joint-PDFs at $x/D = 40.3$ and $y/x = -0.03$, for $\lambda = 3.4$ and for $T_i = 0.4\%$ and $T_i = 9.8\%$.

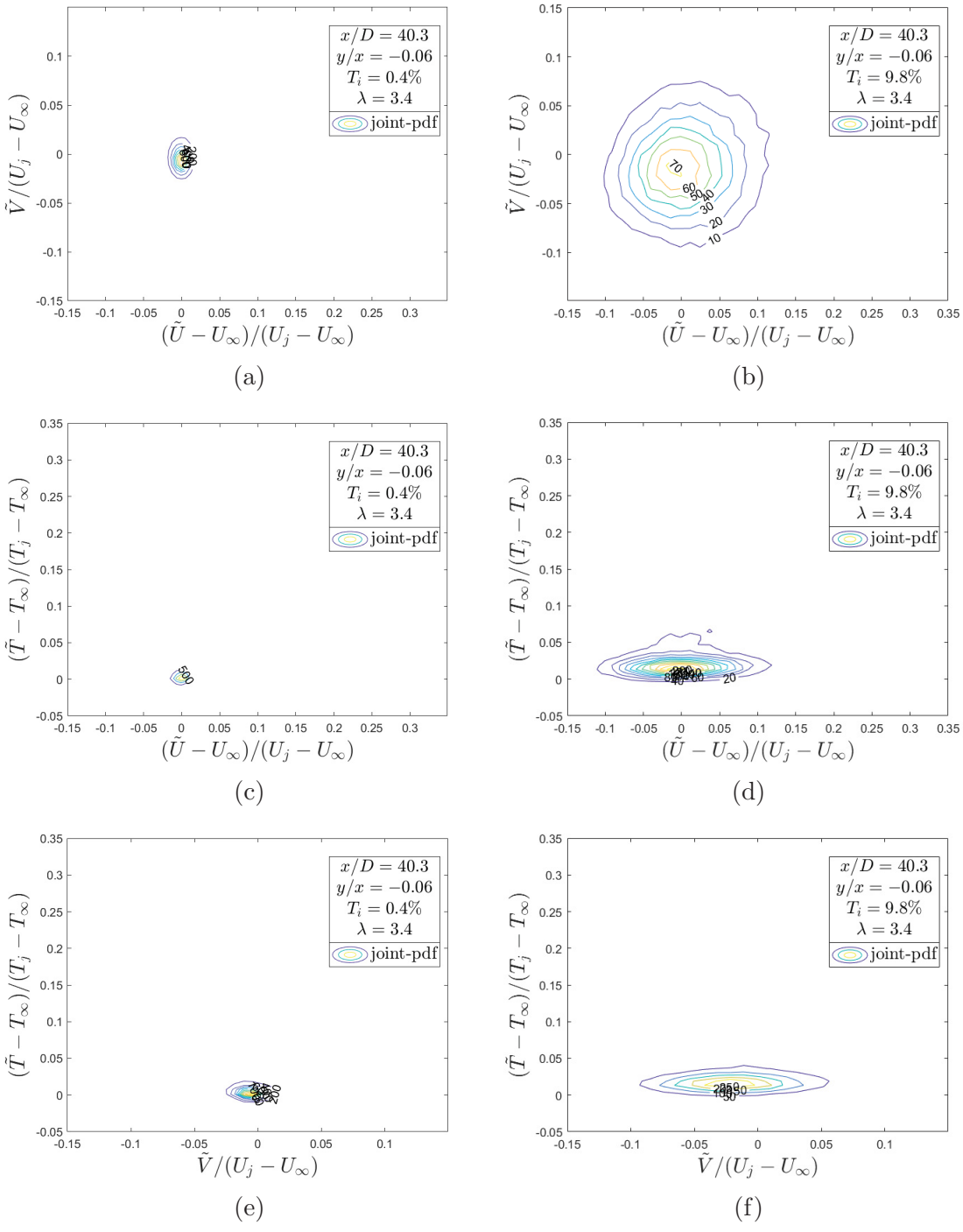

Figure 4–28: Joint-PDFs at $x/D = 40.3$ and $y/x = -0.06$, for $\lambda = 3.4$ and for $T_i = 0.4\%$ and $T_i = 9.8\%$.

4.2.6 Conditional expectations

To further investigate issues related to entrainment, figures 4–29, 4–30 and 4–31 depict the expectation of the radial velocity fluctuations conditioned on the axial velocity fluctuations and the expectation of the temperature fluctuations conditioned on the axial and radial velocity fluctuations, respectively. The results are shown at the three radial positions, with two background turbulence intensities, for $\lambda = 3.4$, and at $x/D = 40.3$.

At the jet centerline ($y/x = 0$), the conditional expectation of v on u is effectively flat. The observed deviations from the flat curve come from slight misalignment with the center of the jet. Indeed, the data point from which these conditional expectations were calculated is the closest to the jet centerline, which may in fact be located at a slightly positive value of y. At $y/x = -0.03$ and -0.06, it can be observed that the expectation of v conditioned on u are slightly steeper when $T_i = 9.8\%$, which means that axial velocity fluctuations are associated with larger radial velocity fluctuations.

For both values of T_i, the expectations of the temperature fluctuations conditioned on the axial velocity fluctuations generally exhibit a linear trend. The most noticeable difference in these plots is their dependence on λ when T_i is low (0.4%), which is much stronger than in the $T_i = 9.8\%$ case. Moreover, this dependence becomes even more prominent as $|y/x|$ increases. Furthermore, these conditional expectations are also steeper when the values of λ and T_i increase, which suggests that the axial velocity fluctuations transport of temperature fluctuations intensifies when λ and T_i increase.

Similar to the expectation of v on u, the expectation of θ conditioned on v is effectively flat at the jet centerline. In addition to the slight misalignment with the

center of the jet, the geometry of the probe and the inevitable separation between the wires result in $\tilde{V}$ and $\tilde{T}$ being measured at locations separated by 2 mm. At $y/x = -0.03$ and -0.06, the expectations of the temperature fluctuations conditioned on the radial velocity fluctuations show similar behaviours for both values of T_i. In terms of entrainment, a steeper conditional expectation of θ on v means that an axial velocity fluctuation of a given magnitude may potentially transport larger temperature fluctuations and therefore increase the mixing. When $T_i = 0.4\%$, it can be observed that the expectation of θ conditioned on v is steeper when the value of λ increases and that the dependence on λ increases with increasing $|y/x|$. However, when $T_i = 9.8\%$, no significant dependence on λ is noticeable. At $y/x = -0.03$, the conditional expectations of θ on v are quite similar for both values of T_i (and slightly steeper for $\lambda = 5.7$ when $T_i = 0.4\%$) but at $y/x = -0.06$, they are generally steeper when $T_i = 9.8\%$. This is consistent with the $\rho_{v\theta}$ profiles (figure 4–18) and may be associated with enhanced turbulent diffusion of the scalar across the flow due to the strong background turbulence.

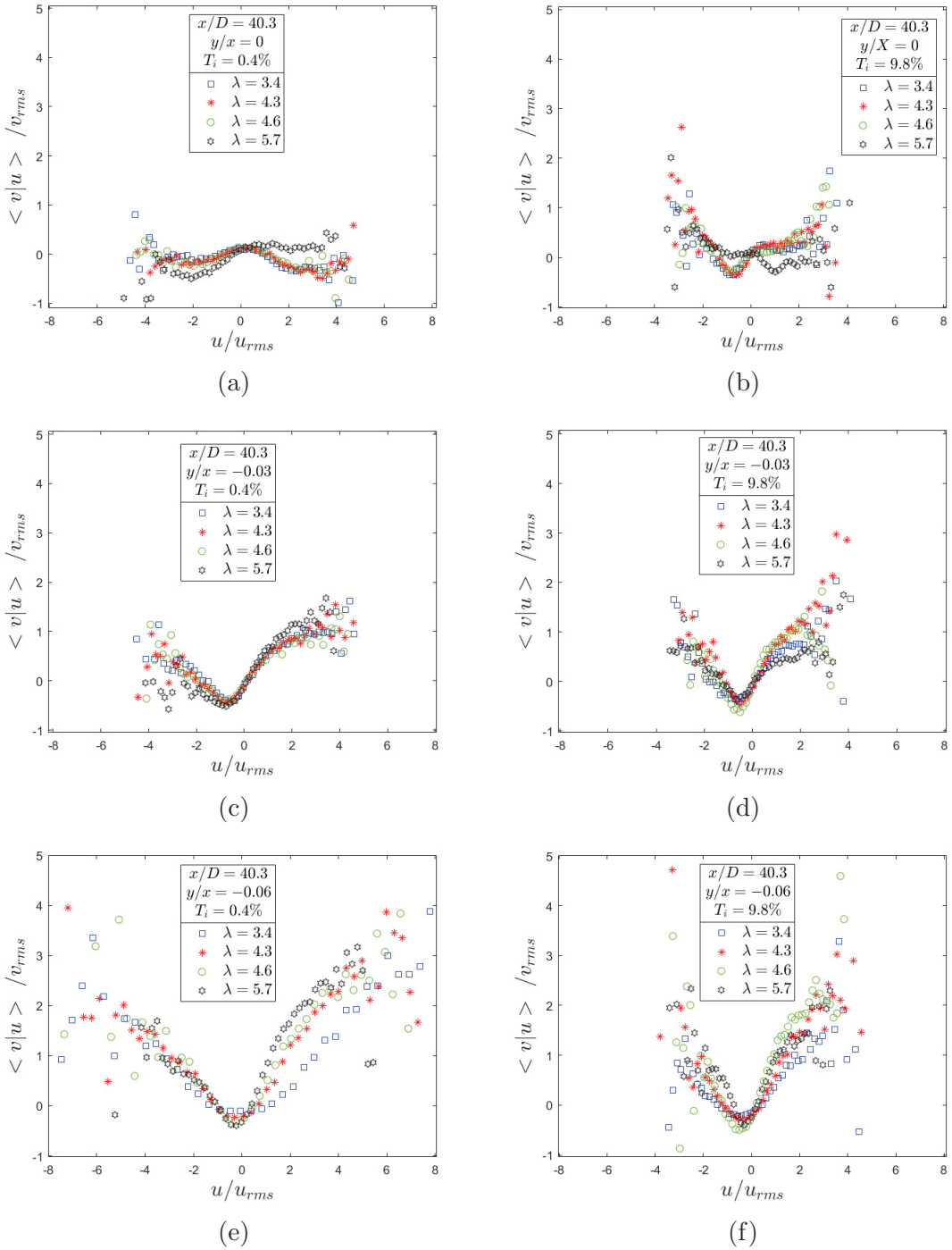

Figure 4–29: Conditional expectation of the radial velocity fluctuations on the axial velocity fluctuations for the three radial positions and two background turbulence intensities, at $x/D = 40.3$ and for $\lambda = 3.4$

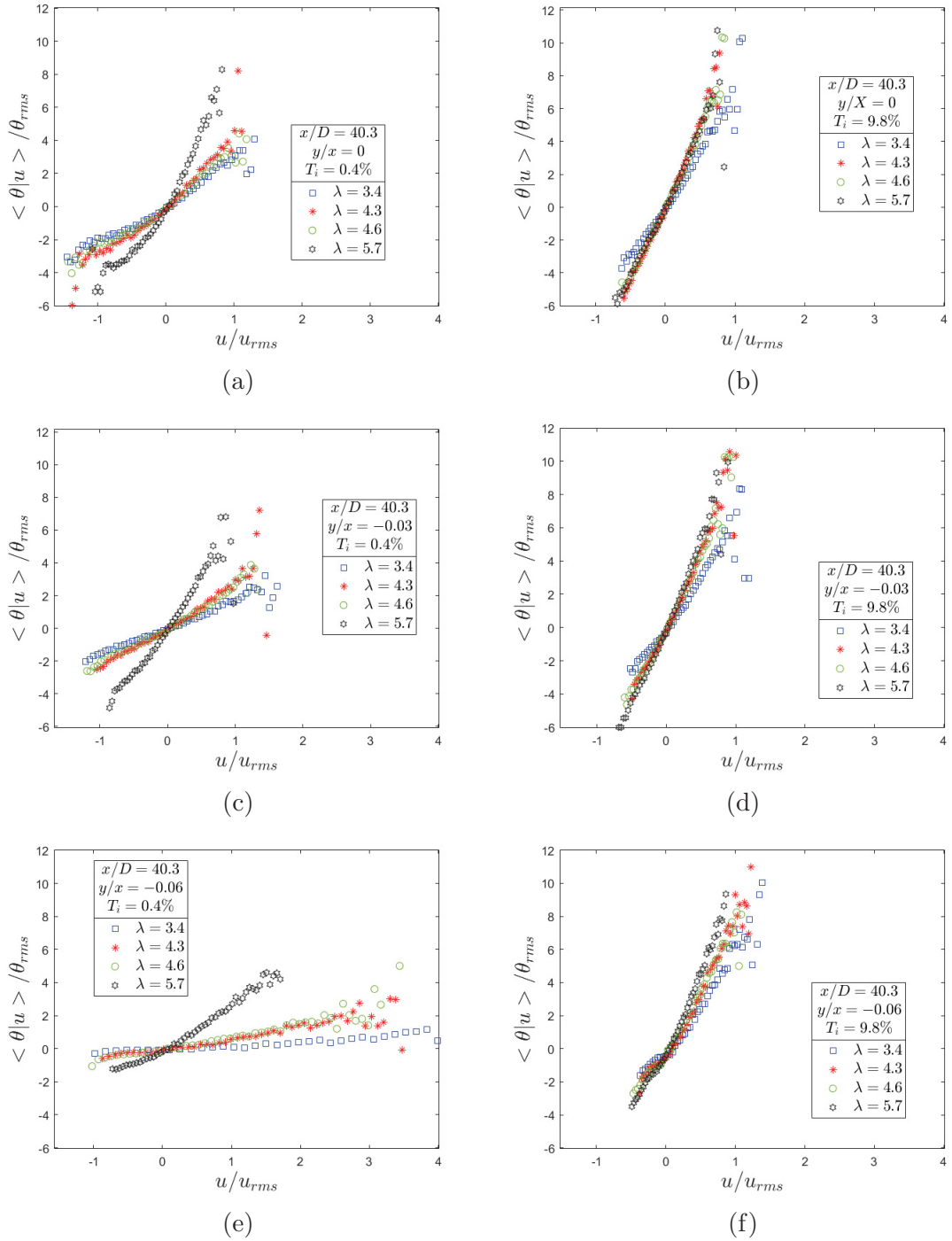

Figure 4–30: Conditional expectation of the temperature fluctuations on the axial velocity fluctuations for the three radial positions and two background turbulence intensities, at $x/D = 40.3$ and for $\lambda = 3.4$

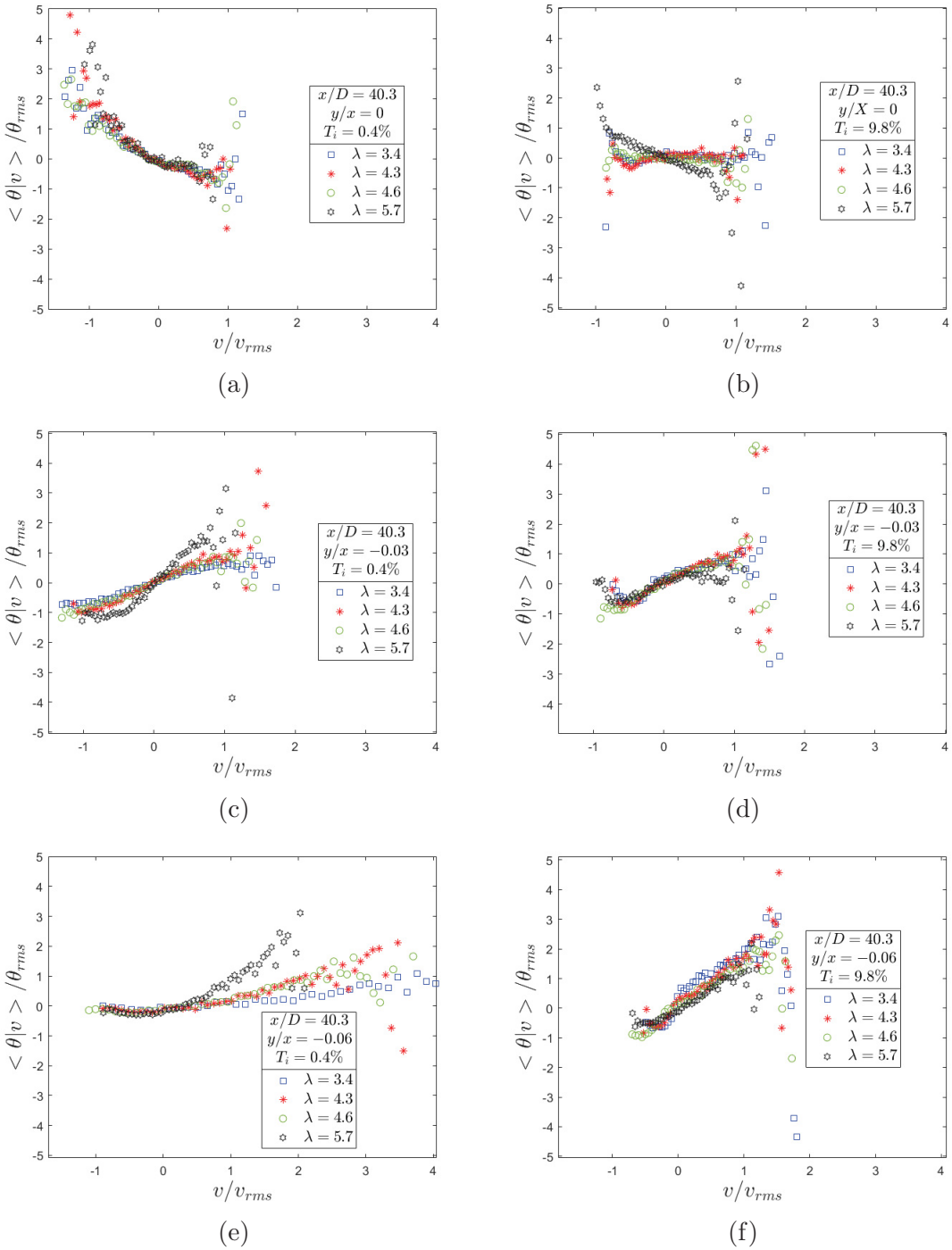

Figure 4–31: Conditional expectation of the temperature fluctuations on the radial velocity fluctuations for the three radial positions and two background turbulence intensities, at $x/D = 40.3$ and for $\lambda = 3.4$

CHAPTER 5
Concluding remarks

5.1 Summary

The main objective of this work was to experimentally study the effect of background turbulence on the dynamics and mixing of an axisymmetric turbulent jet of heated air emitted into a turbulent coflow. To this end, coflows of various turbulence intensities were generated in a wind tunnel by means of passive and active grids (and also the absence of a grid). An experimental set-up was also designed and built to generate the axisymmetric jet. To undertake simultaneous measurements of the velocity and temperature fields, hot-wire anemometry and cold-wire thermometry were used in conjunction with a three-wire sensor that was designed and built. Data were recorded at four downstream positions from the jet exit, for two jet velocities, two coflow velocities and in three different levels of background turbulence intensity, for a total of 48 sets of measurements. To the best of the author's knowledge, this work is the only one simultaneously measuring the longitudinal and radial components of velocity and the temperature, for a turbulent jet emitted into a turbulent background.

From the measurements, it was observed that the evolution of the turbulent jet was similar when it was emitted into a nominally laminar ($T_i = 0.4\%$) background flow or one having a low turbulence intensity ($T_i = 2.2\%$). However, it was found that a higher level of background turbulence intensity in the coflow ($T_i = 9.8\%$) accelerated the downstream evolution of the jet. Specifically, the measured radial

profiles of the mean axial velocity and temperature excesses had lower centerline values and larger radial extents for the $T_i = 9.8\%$ case, when compared to the $T_i = 0.4\%$ and 2.2% cases. The rates of decay of the mean centerline values and the growth of the profile half-widths with the downstream distance also increased for the highest background turbulence intensity. Similar to the mean quantities, the radial spread of the r.m.s. profiles and the decay of the centerline r.m.s. velocity values were enhanced by the more intense turbulent background (which was not strongly observed for the rate of decay of the centerline r.m.s. temperatures). Moreover, the evolution of mean and r.m.s. quantities with λ suggested that the effect of background turbulence was more significant on weaker jets, as the (average) jet is destroyed more quickly when its initial velocity decreases or when the coflow velocity increases.

In agreement with the individual profiles of the velocities and the temperature, measurements of combined velocity-temperature statistics also showed the efficiency of the strongest background turbulence in mixing and diluting the jet. Smaller magnitudes of the correlation coefficient of the Reynolds stress (ρ_{uv}) and increased radial spread of the correlation coefficient of the scalar flux ($\rho_{v\theta}$) were measured when $T_i = 9.8\%$. The profiles of $\rho_{u\theta}$ for the $T_i = 9.8\%$ case showed a strong initial transport of temperature by the axial velocity fluctuations, which was so effective that the magnitude of $\rho_{u\theta}$ rapidly decayed with increasing downstream position, when compared to the $T_i = 0.4\%$ and 2.2% cases. Moreover, the off-axis double peaks, observed when $T_i = 0.4\%$ in the radial profiles of u_{rms}, θ_{rms} and $\rho_{u\theta}$, disappeared at the smallest values of λ when $T_i = 9.8\%$. This indicates a change in the jet's structure presumably linked to increased turbulent transport associated with the turbulent background.

Power and coherence spectra were examined to investigate the scales at which the background turbulence impacts the jet and the effect of the background turbulence on the entrainment mechanism. The power spectra of the two components of the velocity and temperature demonstrated that the large eddies in the flow are the most impacted by an increase in the intensity of the background turbulence. The effect of the turbulent background on the large scales was also observed by way of the coherence spectra. When $T_i = 0.4\%$, they exhibited a single peak at intermediate scales, which presumably arises from nibbling, whereas a significant increase in the coherence at large scales was observed when $T_i = 9.8\%$, indicating a more important role of these large scales in the transport of temperature within the jet.

The velocity and temperature fluctuations inside the jet were evaluated using probability density functions, which were calculated at three radial positions. When the level of background intensity increased, a larger range of velocities was measured in the jet, and cold fluid from the surroundings was found deeper inside the jet. Both results suggest increased mixing due to the stronger turbulent background.

The measurements of conditional expectations demonstrated that the axial velocity fluctuations were associated with larger radial velocity fluctuations and larger temperature fluctuations. Moreover, the conditional expectation of θ on v also highlighted the increased turbulent diffusion of the scalar in the radial direction across the flow due to the strong background turbulence.

In general, the dependence of the different quantities on λ and T_i was found to be complex, and to differ depending on the statistics that were measured. For instance, the differences in the mean and r.m.s. velocity and temperature profiles for the different values of λ were more significant when $T_i = 9.8\%$, compared to the $T_i = 0.4\%$ case. The same trend was observed for the correlation coefficients, whereas

the opposite one was observed for the expectations of the temperature fluctuations conditioned on the axial and radial velocity fluctuations.

Finally, the present work, which was aimed at extending our understanding of the mixing of turbulent jets emitted into turbulent coflows, also has implications to modelling of these jets. When the coflow is turbulent, the multiplicity of scales present in the flow complicates the notion of self-similarity and the choice of the characteristic scale for turbulent entrainment models. Moreover, the complex dependence of the jet mixing on λ and T_i should be further investigated and taken into account in future models. Finally, it is of interest to predict the observed change in the entrainment mechanism and the enhanced role of large scales of the background turbulence.

5.2 Suggestions for future works

The first recommendation for extending this work would be to use the simultaneous measurements of velocity and scalar fields to calculate the total mass, momentum and scalar flow rates, including the mean and turbulent components. For jets emitted into turbulent backgrounds with a mean flow, their governing equations may be different than equations (2.10), (2.12) and (2.13), because the mean and r.m.s. velocities do not decay to zero as $y \to \infty$. This calculation will undoubtedly help further examination of the effect of the background turbulence on entrainment in jets.

Further experiments would also allow for a more systematic and detailed comparison of coherence spectra between different levels of background turbulence. Additional measurements would help confirm the impact of the background turbulence

on the entrainment mechanism at large scales, especially ones measured at transverse locations that correspond to the half-widths of the jet, where the correlation is strong.

In the present work, the (average) jet was almost "destroyed" at $x/D = 75.0$ for $\lambda = 3.4$. Additional measurements farther downstream, and with smaller values of λ, would therefore be beneficial to see the complete destruction of the jet's structure for other parameters. It would be of particular interest to assess how the destruction of the jet depends on parameters such as T_i, λ, etc. In particular, it was previously mentioned that the evolution of the jet can be impacted by the combined effect of the background turbulence intensity (T_i) and the background integral length scale (l). Additional measurements would be beneficial to decouple the effects of these two parameters on the jet's behaviour.

Further studies in which the length scale of the jet is varied would also be of particular benefit, since this was not examined in the present work. (Only one jet diameter was used in the present experiments.) There would be merit in repeating the present experiments for different values of D/l, where l is the integral length scale of the background turbulence.

APPENDIX A
Values of U_j, U_∞ and λ for the 48 cases

Table A–1: Values of U_∞ and λ for data sets number 1 to 12 ($U_j = 25m/s$)

x/D	26.5		40.3		54.2		75.0	
	U_∞	λ	U_∞	λ	U_∞	λ	U_∞	λ
$T_i = 0.4\%$	7.15	3.50	7.19	3.48	7.14	3.50	7.18	3.48
$T_i = 2.2\%$	7.58	3.30	7.22	3.46	7.30	3.43	7.15	3.50
$T_i = 9.8\%$	7.58	3.30	7.84	3.19	7.82	3.20	8.12	3.08
	Average values: $U_\infty = 7.44$, $\lambda = 3.37$							

Table A–2: Values of U_∞ and λ for data sets number 13 to 24 ($U_j = 32m/s$)

x/D	26.5		40.3		54.2		75.0	
	U_∞	λ	U_∞	λ	U_∞	λ	U_∞	λ
$T_i = 0.4\%$	7.15	4.47	7.22	4.43	7.74	4.13	7.07	4.52
$T_i = 2.2\%$	7.55	4.24	7.20	4.45	7.25	4.42	7.15	4.07
$T_i = 9.8\%$	7.54	4.24	8.06	3.97	7.83	4.09	8.00	4.00
	Average values: $U_\infty = 7.48$, $\lambda = 4.29$							

Table A–3: Values of U_∞ and λ for data sets number 25 to 36 ($U_j = 25m/s$)

x/D	26.5		40.3		54.2		75.0	
	U_∞	λ	U_∞	λ	U_∞	λ	U_∞	λ
$T_i = 0.4\%$	5.55	4.51	5.31	4.71	5.23	4.78	5.32	4.70
$T_i = 2.2\%$	5.63	4.44	5.40	4.63	5.31	4.71	5.32	4.70
$T_i = 9.8\%$	5.94	4.21	5.88	4.25	5.43	4.60	5.45	4.59
	Average values: $U_\infty = 5.48$, $\lambda = 4.57$							

Table A–4: Values of U_∞ and λ for data sets number 37 to 48 ($U_j = 32m/s$)

x/D	26.5		40.3		54.2		75.0	
	U_∞	λ	U_∞	λ	U_∞	λ	U_∞	λ
$T_i = 0.4\%$	5.84	5.48	5.52	5.80	5.70	5.61	5.21	6.14
$T_i = 2.2\%$	5.74	5.57	6.22	5.14	5.42	5.90	5.35	5.98
$T_i = 9.8\%$	5.68	5.63	5.82	5.50	5.67	5.64	5.50	5.82
	Average values: $U_\infty = 5.64$, $\lambda = 5.68$							

APPENDIX B
Sources of error and uncertainty analysis

This section presents an uncertainty analysis for the temperature (B.1) and velocity (B.2) measured with the X-T probe. It is followed by the calculation of the uncertainties in the combined velocity-temperature statistics (B.3) and in the measurements of the velocity and temperature at the jet exit (B.4). The uncertainty analysis models used in this section are from Taylor (1997) and Jørgensen (2002). They are based on a propagation of uncertainties and a coverage factor of 2, to obtain uncertainties with a confidence level of 95%.

B.1 Uncertainty in the temperature measurements

The uncertainty in the temperature measurements comes from the following sources: (i) constant current anemometer, (ii) DAQ board, (iii) curve fit to the calibration data, (iv) ambient conditions variations, and (v) probe position and alignment.

The dynamic compensation and adjustment of the current and gain that were done before the cold-wire calibration ensure a good signal-to-noise ratio and a low sensitivity to velocity of the sensor. Moreover, the obtained cut-off frequency was on the order of the highest frequency in the flow, resulting in a good temporal resolution of the temperature fluctuations. The uncertainty in the temperature measurements arising from the constant current anemometer will therefore be deemed negligible, compared to the other sources of error.

The resolution uncertainty (in percentage) of the data acquisition board is calculated from the following equation (Jørgensen 2002):

$$uncertainty = \left(\frac{1}{\sqrt{3}} \frac{1}{T} \frac{\partial T}{\partial E} \frac{E_{AD}}{2^n} \right) \times 100 \tag{B.1}$$

where $\frac{\partial T}{\partial E}$ is the slope of the calibration curve ($1.9°C/V$), E_{AD} is the A/D board input range (10V) and n is the resolution in bits (16) of the acquisition system. For the lowest temperature value recorded in the jet during the experiments ($T = 20.0°C$), the relative standard uncertainty is therefore equal to 0.0008%

During the calibration, the thermocouple measured temperatures with a resolution of $\pm 0.1°C$ and this error is assumed to follow uniform distribution. The relative standard uncertainty (in percentage) is therefore:

$$uncertainty = \frac{0.1}{\sqrt{3}} \left(\frac{1}{T} \right) \times 100 \tag{B.2}$$

where T is the nominal value of the temperature read by the thermocouple. The minimum temperature measured during the calibration was $T = 24.5°C$ in the present work so the maximum uncertainty is 0.24%.

The uncertainty caused by the fit to the calibration data (E *vs.* T) is calculated using the standard deviation of the curve-fitting errors. As previously discussed, it is assumed that the uncertainty in the output voltage (E) is negligible. To obtain these errors, the difference between each measured temperature ($T_{i,measured}$) and its corresponding temperature evaluated by the curve fit (T_{fit}) is calculated and then divided by T_{fit} to obtain relative errors. From these errors, the relative standard

uncertainty (in percentage) is obtained as follows:

$$uncertainty = \sqrt{\frac{1}{N-2}\sum_{i=1}^{N}\left(\frac{T_{fit}(E_i) - T_{i,measured}}{T_{fit}(E_i)}\right)^2} \times 100 \tag{B.3}$$

where $N-2$ corresponds to the number of data points minus the number of degrees of freedom used to obtain the coefficients of the least-squares fit line. In the present work, the relative standard uncertainty is 0.45%.

Variations of the coflow mean temperature were measured on both sides of the jet over the course of an experiment, due to drifts in the ambient temperature and pressure. These variations only affect the mean temperature and not the fluctuations. To account for these variations, data points were taken in order from one side of the jet to the other, and the background flow temperature is assumed to vary linearly with time. The coflow mean temperature values were then subtracted from the mean temperature measurements, thus obtaining the mean temperature excess.

The relative uncertainty in the temperature measurements due to the probe positioning is calculated as follows:

$$uncertainty = \left(\frac{\delta y}{T}\frac{dT}{dy}_{max}\right) \times 100 \tag{B.4}$$

where $\delta y = 7.6 \times 10^{-4} cm$ is the accuracy of the traversing mechanism, $(dT/dy)_{max} = 2.04°C \cdot cm^{-1}$ is the largest mean temperature gradient measured in the jet and $T = 22.8°C$ is the temperature at that point of maximum gradient. The value obtained for this relative uncertainty is 0.007%. Moreover, the resistance of the cold-wire does not depend on the direction of the flow but only on its temperature so minor misalignments of the probe do not affect the temperature measurements.

Table B–1 summarizes the uncertainties in the temperature measurements in order of decreasing importance.

Table B–1: Uncertainties in the temperature measurements

Source of error	Relative standard uncertainty
Calibration curve fit	0.45%
Temperature measurement during calibration	0.24%
Probe positioning	0.007%
DAQ board	0.0008%
Anemometer	negligible

The total relative uncertainty with a 95% confidence level is calculated by the following formula:

$$\text{total uncertainty} = 2\sqrt{\sum_{i=1}^{n}(\text{uncertainty}_i)^2} \tag{B.5}$$

Using the values in table B–1, the total relative uncertainty obtained is 1.02%.

B.2 Uncertainty in the velocity measurements

Similar to the temperature, the uncertainty in the velocity measurements comes from the following sources: (i) constant temperature anemometer, (ii) DAQ board, (iii) calibration equipment and curve fit, (iv) temperature measurements, and (v) probe positioning and alignment.

The first source of error in the measurement of velocity comes from the anemometer but it will be considered negligible in comparison with other error sources. Indeed,

constant temperature anemometers have good signal-to-noise ratio, good repeatability and low drift. Moreover, the typical frequency response of hot-wires is on the order of 100 kHz, whereas the maximum frequency encountered in the present flow was generally an order of magnitude smaller, so the temporal resolution of the hot-wires will not add to the uncertainty.

The uncertainty in the velocity measurements due to the data acquisition board is calculated in the same way as the uncertainty in the temperature measurements, from the following equation (Jørgensen 2002):

$$uncertainty = \left(\frac{1}{\sqrt{3}} \frac{1}{U} \frac{\partial U}{\partial E} \frac{E_{AD}}{2^n} \right) \times 100 \tag{B.6}$$

where $\frac{\partial U}{\partial E}$ is the slope of the calibration curve (largest value is $31.6 m/s/V$), E_{AD} is the A/D board input range (5V) and n is the resolution in bits (16) of the acquisition system. For the lowest velocity value recorded in the jet during the experiments ($U = 5.2 m/s$), the relative standard uncertainty is therefore equal to 0.0027%.

It has been established that the relative standard uncertainty associated with typical hot-wire calibration equipment is 1% (Jørgensen 2002). An additional uncertainty in the velocity measurements is caused by the curve fit to the calibration data (E^2 *vs.* U) and is calculated with the standard deviation of the curve-fitting errors (similar to the uncertainty in the temperature). Moreover, the hot-wire calibration was performed at different temperatures so the King's Law calibration constants A and B (equations 3.3) had to be corrected, as explained in Chapter 3. Fitting equations 3.4 and 3.5 to the A *vs.* T and B *vs.* T data also causes uncertainties in the velocity measurements. The uncertainty due to the three calibration curve fits (E^2 *vs.* U, A *vs.* T, and B *vs.* T) should therefore be calculated and the following

equation is used to estimate the associated uncertainty:

$$uncertainty = \sqrt{\frac{1}{N-3}\sum_{i=1}^{N}\left(\frac{U_{fit}(E_i) - U_{i,measured}}{U_{fit}(E_i)}\right)^2 + \left(\frac{1}{U}\frac{\partial U}{\partial A}\sigma_A\right)^2 + \left(\frac{1}{U}\frac{\partial U}{\partial B}\sigma_B\right)^2} \times 100 \tag{B.7}$$

The first term is similar to equation B.10, in which $N-3$ corresponds to the number of data points minus the number of degrees of freedom used to obtain the A, B and n coefficients of the least-squares fit. The second and third terms correspond to the uncertainty due to the A *vs.* T, and B *vs.* T relations, respectively, and are added in quadrature following the propagation of uncertainties theory presented by Taylor (1997). The uncertainties in A and B, respectively σ_A and σ_B are obtained by the following equations (Taylor 1997):

$$\sigma_A = \sqrt{\frac{1}{N-2}\sum_{i=1}^{N}\left(\frac{A_{fit}(T_i) - A_{i,measured}}{A_{fit}(T_i)}\right)^2 + \left(\frac{\partial A}{\partial T}\Delta T\right)^2} \tag{B.8}$$

$$\sigma_B = \sqrt{\frac{1}{N-2}\sum_{i=1}^{N}\left(\frac{B_{fit}(T_i) - B_{i,measured}}{B_{fit}(T_i)}\right)^2 + \left(\frac{\partial B}{\partial T}\Delta T\right)^2} \tag{B.9}$$

in which each first term represents the uncertainty from the corresponding curve fit and each second term represents the uncertainty due to the maximum variation of the jet temperature ($\Delta T = 1°\text{C}$) for one King's Law calibration. Thus, the relative uncertainty calculated from equation B.7 is 2.33% (for the lowest velocity measured during the calibration, $U = 2.0m/s$).

The values of A and B in the King's Law depend on the temperature so the temperature measurements by the cold-wire should be taken into account in the uncertainty in the velocity measurements. The value used for the uncertainty due

to the temperature measurements is 0.51% (half of the total uncertainty calculated in section B.1, because all the uncertainties in the velocity measurements should be first added together in quadrature before multiplying the result by two to measure the total uncertainty in the velocity measurements with confidence level of 95%).

The relative uncertainty in the velocity measurements due to the probe positioning is calculated as follows:

$$uncertainty = \left(\frac{\delta y}{U} \frac{dU}{dy}_{max} \right) \times 100 \tag{B.10}$$

where $\delta y = 7.6 \times 10^{-6} m$ is the accuracy of the traversing mechanism, $(dU/dy)_{max} = 537 s^{-1}$ is the largest mean axial velocity gradient measured in the jet and $U = 11.8 m/s$ is the mean velocity at that point of maximum gradient. The value obtained for this relative uncertainty is 0.03%. Moreover, a small misalignment of the probe does have an effect on the velocity measurements. The errors due to the orientation of the probe were accounted for in the data analysis by correcting the effective angle of each hot-wire for each data set to ensure that the radial velocity is zero at the jet centerline.

Table B–2 summarizes the uncertainties in the velocity measurements in order of decreasing importance.

Table B–2: Uncertainties in the velocity measurements

Source of error	Relative standard uncertainty
Calibration curve fit	2.33%
Hot-wire calibration equipment	1%
Temperature measurements	0.51%
Probe positioning	0.03%
DAQ board	0.0027%
Anemometer	negligible

The total relative uncertainty in the velocity measurements, with a 95% confidence level, is calculated with equation B.5 and the obtained value is 5.2%.

B.3 Uncertainty in the combined velocity-temperature statistics

The total relative uncertainties obtained in sections B.1 and B.2 will be used for both the mean and fluctuating components of the velocities and temperature. The relative uncertainties for the combined velocity-temperature statistics can be directly calculated by the propagation of uncertainties as follows:

$$\frac{\delta\overline{uv}}{\overline{uv}} = \sqrt{(\frac{\delta u}{u})^2 + (\frac{\delta v}{v})^2} = \sqrt{2 \times (5.2\%)^2} = 7.4\% \tag{B.11}$$

$$\frac{\delta\overline{u\theta}}{\overline{u\theta}} = \sqrt{(\frac{\delta u}{u})^2 + (\frac{\delta \theta}{\theta})^2} = \sqrt{(5.2\%)^2 + (1.02\%)^2} = 5.3\% \tag{B.12}$$

$$\frac{\delta\overline{v\theta}}{\overline{v\theta}} = \sqrt{(\frac{\delta v}{v})^2 + (\frac{\delta \theta}{\theta})^2} = \sqrt{(5.2\%)^2 + (1.02\%)^2} = 5.3\% \tag{B.13}$$

B.4 Uncertainty in the velocity and temperature measurements at the jet exit

The velocity and temperature at the jet exit were respectively measured by a mass flow meter and a thermocouple. The uncertainty in their values is therefore different than the measurements done with the X-T probe.

The variations in the measured mass flow rate result in uncertainty in the velocity at the jet exit. The maximum variation in the jet velocity throughout the experiments is estimated to be $\pm 0.5 m/s$, which corresponds to respectively 2.0% and 1.6% of the two jet velocities ($25 m/s$ and $32 m/s$). The maximum relative uncertainty in U_{jet} is therefore 2%.

To avoid disturbing the jet, a fixed thermocouple could not be used to continuously measure the temperature at the jet exit. At the end of each experiment, a rod-mounted thermocouple was therefore manually position at the jet exit and the temperature was recorded for a few seconds. The relative uncertainty in this measurement is estimated to be 3%.

References

[1] A. Afrooz. Turbulent jets in the presence of a turbulent ambient. Master's thesis, McGill University, 2019.

[2] R.A. Antonia and R.W. Bilger. An experimental investigation of an axisymmetric jet in a co-flowing air stream. *Journal of Fluid Mechanics*, 61(4):805–822, 1973.

[3] G.K. Batchelor. The theory of homogeneous turbulence. *Cambridge University Press*, pages 64–65, 1954.

[4] H.A. Becker, H.C. Hottel, and G.C. Williams. The nozzle-fluid concentration field of the round, turbulent, free jet. *Journal of Fluid Mechanics*, 30(2):285–303, 1967.

[5] A.D. Birch, D.R. Brown, M.G. Dodson, and J.R. Thomas. The turbulent concentration field of a methane jet. *Journal of Fluid Mechanics*, 88(3):431–449, 1978.

[6] D. Blais. Wind tunnel flow characterization. Technical report, McGill University, 2019.

[7] L.J.S. Bradbury and J. Riley. The spread of a turbulent plane jet issuing into a parallel moving airstream. *Journal of Fluid Mechanics*, 27(2):381–394, 1967.

[8] L.W.B. Browne, R.A. Antonia, and L.P. Chua. Calibration of x-probes for turbulent flow measurements. *Experiments in Fluids*, 7:201–208, 1988.

[9] H.H. Bruun. *Hot-wire Anemometry, Principles and Signal Analysis*. Oxford University Press, 1995.

[10] Y.A. Cengel and J.M. Cimbala. *Fluid mechanics : fundamentals and applications*. McGraw-Hill Higher Education, 2006.

[11] C.Y. Ching, H.J.S. Fernando, and A. Robles. Breakdown of line plumes in turbulent environments. *Journal of Geophysical Research: Oceans*, 100(C3):4707–4713, 1995.

[12] P.C.K. Chu, J.H. Lee, and V.H. Chu. Spreading of turbulent round jet in coflow. *Journal of Hydraulic Engineering*, 125(2):193–204, 1999.

[13] A. Cohen. Influences of free-stream turbulence and char-layer porosity on the drag on windborne firebrands. Master's thesis, McGill University, 2018.

[14] G. Comte-Bellot and S. Corrsin. The use of a contraction to improve the isotropy of grid-generated turbulence. *Journal of Fluid Mechanics*, 25(4):657–682, 1966.

[15] G. Comte-Bellot and S. Corrsin. Simple eulerian time correlation of full-and narrow-band velocity signals in grid-generated, 'isotropic' turbulence. *Journal of Fluid Mechanics*, 48(2):273–337, 1971.

[16] S. Corrsin. On the spectrum of isotropic temperature fluctuations in an isotropic turbulence. *Journal of Applied Physics*, 22(4):469–473, 1951.

[17] S. Corrsin and A.L. Kistler. Free-stream boundaries of turbulent flows. 1955.

[18] A. Cuthbertson, D. Malcangio, P. Davies, and M. Mossa. The influence of a localised region of turbulence on the structural development of a turbulent, round, buoyant jet. *Fluid Dynamics Research*, 38:683–698, 10 2006.

[19] W.J.A. Dahm and P.E. Dimotakis. Measurements of entrainment and mixing in turbulent jets. *AIAA Journal*, 25(9):1216–1223, 1987.

[20] A. Darisse, J. Lemay, and A. Benaïssa. Budgets of turbulent kinetic energy, reynolds stresses, variance of temperature fluctuations and turbulent heat fluxes in a round jet. *Journal of Fluid Mechanics*, 774:95–142, 2015.

[21] M.J. Davidson and H.J. Wang. Strongly advected jet in a coflow. *Journal of Hydraulic Engineering*, 128:742–752, 2002.

[22] D.R. Dowling and P.E. Dimotakis. Similarity of the concentration field of gas-phase turbulent jets. *Journal of Fluid Mechanics*, 218:109–141, 1990.

[23] M.M. Enayet, M.M. Gibson, A.M.K.P. Taylor, and M. Yianneskis. Laser-doppler measurements of laminar and turbulent flow in a pipe bend, international journal of heat and fluid flow. *Combustion and Flame*, 3:213 – 219, 1982.

[24] E. Ferdman, S. Kim, and M. Otugen. Effect of initial velocity profile on the development of round jets. *Journal of Propulsion and Power*, 16:676–686, 07 2000.

[25] H.B. Fischer, E.J. List, R.C.Y. Koh, J. Imberger, and N.H. Brooks. Turbulent jets and plumes, in mixing in inland and coastal waters. *Ed. Academic Press.*, pages 315–389, 1979.

[26] S.J. Gaskin, M. Mckernan, and F. Xue. The effect of background turbulence on jet entrainment: an experimental study of a plane jet in a shallow coflow. *Journal of Hydraulic Research*, 42(5):533–542, 2004.

[27] W.K. George. The self-preservation of turbulent flows and its relation to initial conditions and coherent structures. *Recent Advances in Turbulence*, pages 39–73, 1989.

[28] Y. Guo, D. Malcangio, P.A. Davies, and H.J.S. Fernando. A laboratory investigation into the influence of a localized region of turbulence on the evolution of a round turbulent jet. *Fluid Dynamics Research*, 36:75–89, 02 2005.

[29] J. C. R. Hunt. *Atmospheric Jets and Plumes*, pages 309–334. Springer Netherlands, 1994.

[30] H.J. Hussein, S.P. Capp, and W.K. George. Velocity measurements in a high-reynolds-number, momentum-conserving, axisymmetric, turbulent jet. *Journal of Fluid Mechanics*, 258:31–75, 1994.

[31] J.C. Isaza, R. Salazar, and Z. Warhaft. On grid-generated turbulence in the near- and far field regions. *Journal of Fluid Mechanics*, 753:402–426, 2014.

[32] F.E. Jørgensen. How to measure turbulence with hot-wire anemometers. Technical report, Dantec Dynamics publication, 2002.

[33] U. Karnik and S. Tavoularis. Measurements of heat diffusion from a continuous line source in a uniformly sheared turbulent flow. *Journal of Fluid Mechanics*, 202:233–261, 1989.

[34] B. Khorsandi. *Effect of Background Turbulence on an Axisymmetric Turbulent Jet*. PhD thesis, McGill University, 2011.

[35] B. Khorsandi, S. Gaskin, and L. Mydlarski. Effect of background turbulence on an axisymmetric turbulent jet. *Journal of Fluid Mechanics*, 736:250–286, DEC 2013.

[36] A. Kolmogorov. Dissipation of Energy in the Locally Isotropic Turbulence. *Akademiia Nauk SSSR Doklady*, 32:16–18, 1941.

[37] A. Kolmogorov. The Local Structure of Turbulence in Incompressible Viscous Fluid for Very Large Reynolds' Numbers. *Akademiia Nauk SSSR Doklady*, 30:301–305, 1941.

[38] A.C.H. Lai, A.W.K. Law, and E.E. Adams. A second-order integral model for buoyant jets with background homogeneous and isotropic turbulence. *Journal of Fluid Mechanics*, 871:271–304, 2019.

[39] A.W.K. Law and H. Wang. Measurement of mixing processes with combined digital particle image velocimetry and planar laser induced fluorescence. *Experimental Thermal and Fluid Science*, 22(3):213 – 229, 2000.

[40] J. Lemay. Constant current anemometer utilization guide. Technical report, Université Laval, 2001.

[41] J. Lemay and A. Benaissa. Improvement of cold-wire response for measurement of temperature dissipation. *Experiments in Fluids*, 31:347–356, 09 2001.

[42] V.J.H. Lienhard and C.W. Van Atta. The decay of turbulence in thermally stratified flow. *Journal of Fluid Mechanics*, 210:57–112, 1988.

[43] G. Lipari and P.K. Stansby. Review of experimental data on incompressible turbulent round jets. *Flow, Turbulence and Combustion*, 87:79–114, 07 2011.

[44] F.C. Lockwood and H.A. Moneib. Fluctuating temperature measurements in a heated round free jet. *Combustion Science and Technology*, 22(1-2):63–81, 1980.

[45] M.B. Long and B.T. Chu. Mixing mechanism and structure of an axisymmetric turbulent mixing layer. *AIAA Journal*, 19(9):1158–1163, 1981.

[46] H. Makita. Realization of a large-scale turbulence field in a small wind tunnel. *Fluid Dynamics Research*, 8:53–64, 1991.

[47] J. Mathew and A.J. Basu. Some characteristics of entrainment at a cylindrical turbulence boundary. *Physics of Fluids*, 14(7):2065–2072, 2002.

[48] J. Mi, D.S. Nobes, and G.J. Nathan. Influence of jet exit conditions on the passive scalar field of an axisymmetric free jet. *Journal of Fluid Mechanics*, 432:91–125, 2001.

[49] M. Moeini, B. Khorsandi, and L. Mydlarski. Effect of coflow turbulence on the dynamics and mixing of a nonbuoyant turbulent jet. *Journal of Hydraulic Engineering*, 47, 10 2020.

[50] B.R. Morton, G.I. Taylor, and J.S. Turner. Turbulent gravitational convection from maintained and instantaneous sources. *Proc. Roy. Soc. of London, Series A*, 234:1–23, 1956.

[51] L. Mydlarski. A turbulent quarter century of active grids: from makita (1991) to the present. *Fluid Dynamics Research*, 49(6), Dec. 2017.

[52] L Mydlarski and Z Warhaft. On the onset of high-reynolds-number grid-generated wind tunnel turbulence. *Journal of Fluid Mechanics*, 320:331–368, Aug. 1996.

[53] T.B. Nickels and A.E. Perry. An experimental and theoretical study of the turbulent coflowing jet. *Journal of Fluid Mechanics*, 309:157–182, 1996.

[54] N.R. Panchapakesan and J.L. Lumley. Turbulence measurements in axisymmetric jets of air and helium. part 1. air jet. *Journal of Fluid Mechanics*, 246:197–223, 1993.

[55] N.R. Panchapakesan and J.L. Lumley. Turbulence measurements in axisymmetric jets of air and helium. part 2. helium jet. *Journal of Fluid Mechanics*, 246:225–247, 1993.

[56] A. Perez-Alvarado. *Effect of background turbulence on the scalar field of a turbulent jet*. PhD thesis, McGill University, 2016.

[57] J. Philip and I. Marusic. Large-scale eddies and their role in entrainment in turbulent jets and wakes. *Physics of Fluids*, 24(5), 2012.

[58] S. Pope. *Turbulent Flows*. Cambridge University Press, 2000.

[59] F.P. Ricou and D.B. Spalding. Measurements of entrainment by axisymmetrical turbulent jets. *Journal of Fluid Mechanics*, 11(1):21–32, 1961.

[60] D.J. Shlien. Observations of dispersion of entrained fluid in the self-preserving region of a turbulent jet. *Journal of Fluid Mechanics*, 183:163–173, 1987.

[61] L.F.G. Simmons and C. Salter. Experimental investigation and analysis of the velocity variations in turbulent flow. *Proc. R. Soc. Lond.*, 1934.

[62] A. Sirivat and Z. Warhaft. The mixing of passive helium and temperature fluctuations in grid turbulence. *Journal of Fluid Mechanics*, 120:475–504, 1982.

[63] D.J. Smith and T. Hughes. Some measurements in a turbulent circular jet in the presence of a co-flowing free stream. *Aeronautical Quarterly*, 28(3):185–196, 1977.

[64] R.W. Stewart and A.A. Townsend. Similarity and self-preservation in isotropic turbulence. *Philosophical Transactions of the Royal Society of London. Series A, Mathematical and Physical Sciences*, 243(867):359–386, 1951.

[65] J.R. Taylor. *An Introduction to Error Analysis: The Study of Uncertainties in Physical Measurements*. University Science Books, 1997.

[66] H. Tennekes and J.L. Lumley. *A First Course in Turbulence*. MIT Press, 1972.

[67] A.A. Townsend. The mechanism of entrainment in free turbulent flows. *Journal of Fluid Mechanics*, 26(4):689–715, 1966.

[68] T. Weisgraber and D. Liepmann. Turbulent structure during transition to self-similarity in a round jet. *Experiments in Fluids*, 24:210–224, 1998.

[69] J. Westerweel, C. Fukushima, J. Pedersen, and J. Hunt. Mechanics of the turbulent-non turbulent interface of a jet. *Physical Review Letters*, 95:174501, 11 2005.

[70] J. Westerweel, C. Fukushima, J.M. Pedersen, and J.C.R. Hunt. Momentum and scalar transport at the turbulent/non-turbulent interface of a jet. *Journal of Fluid Mechanics*, 631:199–230, 2009.

[71] R.A.M. Wilson and P.V. Danckwerts. Studies in turbulent mixing—ii: A hot-air jet. *Chemical Engineering Science*, 19(11):885 – 895, 1964.

[72] S.J. Wright. *The Effect of Ambient Turbulence on Jet Mixing*, pages 13–27. Springer Netherlands, Dordrecht, 1994.

[73] I.J. Wygnanski and H. Fiedler. Some measurements in the self-preserving jet. *Journal of Fluid Mechanics*, 38:577–612, 1969.

[74] G. Xu and R. Antonia. Effect of different initial conditions on a turbulent round free jet. *Experiments in Fluids*, 33:677–683, 2002.

[75] A.J. Yule. Large-scale structure in the mixing layer of a round jet. *Journal of Fluid Mechanics*, 89(3):413–432.